

STATE OF CALIFORNIA DEPARTMENT OF TRANSPORTATION

TECHNICAL REPORT DOCUMENTATION PAGE

TR0003 (REV. 10/98)

1. REPORT NUMBER CA12-2040	2. GOVERNMENT ASSOCIATION NUMBER	3. RECIPIENT'S CATALOG NUMBER
4. TITLE AND SUBTITLE Nonlinear Load-Deflection Behavior of Abutment Backwalls with Varying Height and Soil Density		5. REPORT DATE December, 2011
		6. PERFORMING ORGANIZATION CODE
7. AUTHOR(S) Stewart, JP, E Taciroglu, JW Wallace, A Lemnitzer, CH Hilson, A Nojoumi, S Keowan, RL Nigbor, and A Salamanca		8. PERFORMING ORGANIZATION REPORT NO. SGEL 2011-01
9. PERFORMING ORGANIZATION NAME AND ADDRESS University of California, Los Angeles Civil & Environmental Engineering Department 5731 Boelter Hall Los Angeles, CA 90095		10. WORK UNIT NUMBER
		11. CONTRACT OR GRANT NUMBER 59A0655
12. SPONSORING AGENCY AND ADDRESS California Department of Transportation Division of Research and Innovation, MS-83 1227 O Street Sacramento CA 95814		13. TYPE OF REPORT AND PERIOD COVERED Final Report
		14. SPONSORING AGENCY CODE
15. SUPPLEMENTAL NOTES		

16. ABSTRACT

We address the scaling of abutment wall lateral response with wall height and compaction condition through testing and analytical work. The analytical work was undertaken to develop hyperbolic curves representing the load-deflection response of backwalls for two backfill material types (clay and sand) as a function of wall height. The scaling of backwall resistance with height is expressed by an exponent n applied to a normalized wall height; we find that the height scaling exponent can be taken as 1.05 and 1.56 for the considered clay and sand backfill materials.

We tested two wall-soil specimens with identical characteristics except for the level of compaction of the sandy backfill. One specimen (denoted T8.0-1) has as-compacted relative densities ranging from approximately $D_r = 0.4\text{-}0.6$ (which was lower than specified) and the other (T8.0-2) had a high level of compaction of $D_r = 0.9\text{-}1.0$. Other than the degree of compaction, the two specimens are essentially identical in terms of dimensions, material gradation, and boundary conditions imposed during testing. The wall height in these tests is 8.0 ft (2.4 m), which represents an approximate upper-bound backwall height; in previous work we tested a similar specimen with a height of 5.5 ft (1.67 m). The backfill material is a well graded silty sand known in the construction industry as SE-30. The boundary condition imposed on the test is horizontal displacement towards the backfill without rotation (torsion or rocking) or uplift.

The modest- D_r specimen (T8.0-1) exhibits nearly elastic-plastic response with negligible strain softening. The peak resistance was approximately 700 kips (3114 kN), which corresponds to a passive earth pressure coefficient of $K_p=10$, and occurred with a wall-soil interface friction that is approximately half of the soil friction angle. The high- D_r specimen (T8.0-2) exhibits a strongly strain softening response with a peak resistance of approximately 1650 kips (7340 kN) and large-strain (approaching residual) capacity of approximately 1100 kips (4900 kN). These capacities correspond to K_p values of 24 and 17 for peak and large-strain conditions, respectively.

Using shear strength parameter derived from triaxial drained strength testing, log-spiral hyperbolic (LSH) simulations of the backfill response are performed that modestly under predict the peak specimen responses. However, the degree of underprediction is modest relative to the substantial differences in capacity between specimens T8.0-1 and T8.0-2. Those large variations in capacity are well captured by the analysis, suggesting that the LSH method can account for the effects of compaction condition on the wall capacity. The LSH simulations are also able to capture variations in specimen response for different wall height.

We recommend that the height scaling effects in future versions of the SDC be modified to more realistically capture the different trends for cohesive and granular backfills. For granular backfill, stiffness and capacity should scale by an exponent $n = 1.5\text{-}2.0$. We also recommend that compaction condition be considered in the specification of stiffness and capacity.

17. KEY WORDS Abutment Backwall	18. DISTRIBUTION STATEMENT No restrictions. This document is available to the public through the National Technical Information Service, Springfield, VA 22161	
19. SECURITY CLASSIFICATION (of this report) Unclassified	20. NUMBER OF PAGES 123	21. PRICE

Nonlinear Load-Deflection Behavior of Abutment Backwalls with Varying Height and Soil Density

PRINCIPAL INVESTIGATOR

Jonathan P. Stewart
University of California, Los Angeles

CO-PRINCIPAL INVESTIGATORS

Ertugrul Taciroglu and John W. Wallace
University of California, Los Angeles

COLLABORATING RESEARCHER

Anne Lemnitzer
University of California, Irvine

GRADUATE STUDENTS

Chris H. Hilson and Ali Nojoumi
University of California, Los Angeles

STAFF OF NEES@UCLA

Steve Keowen, Robert L. Nigbor and Alberto Salamanca
University of California, Los Angeles

A report on research conducted under Grant No. 59A0655
from the California Department of Transportation

Department of Civil and Environmental Engineering
University of California, Los Angeles
December 2011

DISCLAIMER STATEMENT

This document is disseminated in the interest of information exchange. The contents of this report reflect the views of the authors who are responsible for the facts and accuracy of the data presented herein. The contents do not necessarily reflect the official views or policies of the State of California or the Federal Highway Administration. This publication does not constitute a standard, specification or regulation. This report does not constitute an endorsement by the Department of any product described herein.

For individuals with sensory disabilities, this document is available in Braille, large print, audiocassette, or compact disk. To obtain a copy of this document in one of these alternate formats, please contact: the Division of Research and Innovation, MS-83, California Department of Transportation, P.O. Box 942873, Sacramento, CA 94273-0001.

Table of Contents

TABLE OF CONTENTS.....	III
LIST OF FIGURES.....	V
LIST OF TABLES	IX
ACKNOWLEDGMENTS.....	X
TECHNICAL REPORT DOCUMENTATION PAGE.....	XI
DISCLAIMER STATEMENT.....	XII
EXECUTIVE SUMMARY.....	XIII
1. INTRODUCTION	1
2. LITERATURE REVIEW.....	4
2.1 LARGE-SCALE TESTS OF ABUTMENT SYSTEMS	4
2.2 CALTRANS SEISMIC DESIGN CRITERIA	8
2.3 SIMULATION MODELS OF LATERAL RESPONSE OF BRIDGE ABUTMENTS	10
2.3.1 <i>Log-Spiral Hyperbolic (LSH) Methods</i>	10
2.3.2 <i>Models Based on Hyperbolic Stress-Strain Relationship for Soil</i>	11
3. EXPERIMENTAL SETUP	13
3.1 LOADING SYSTEM & SPECIMEN CONFIGURATION	13
3.2 SENSOR LAYOUT	15
3.3 CONTROL SYSTEM	18
3.4 BACKWALL AND REACTION BLOCK STRUCTURAL REPAIRS	19
4. TEST SPECIMEN	25
4.1. CONCRETE PROPERTIES.....	25
4.2. BACKFILL SOIL	27
4.2.1 <i>Gradation Tests</i>	28
4.2.2 <i>Compaction and Relative Density</i>	29
4.2.3 <i>Strength Tests</i>	37
5. TEST RESULTS.....	41
5.1. LOAD-DISPLACEMENT DATA	41
5.1.1 <i>Baseline Friction Tests</i>	41
5.1.2 <i>Data from T8.0-1</i>	45
5.1.3 <i>Data from T8.0-2a</i>	48
5.1.4 <i>Data from T8.0-2b & T8.0-2c</i>	49
5.2. METRICS OF SPECIMEN PERFORMANCE.....	51
5.2.1 <i>Assembling Data into One Representative Plot</i>	52
5.2.2 <i>Passive Capacity of Backfill Specimen and Force-Displacement Shape</i>	54
5.2.3 <i>Initial Loading and Unload/Reload Moduli</i>	58
5.2.4 <i>Mobilized Interface Friction Angle</i>	63
5.2.5. <i>Earth Pressure Distribution</i>	65
5.3. MAPPED CRACK PATTERNS.....	68

5.3.1 <i>Surface of Backfill</i>	68
5.3.2 <i>Post-Test Trenching of Slip Surfaces</i>	72
6. ANALYTICAL AND NUMERICAL MODELING.....	75
6.1. DEVELOPMENT OF A HFD MODEL INCORPORATING ABUTMENT HEIGHT EFFECTS.....	75
6.1.1 <i>HFD Representation of Test Results for 1.68 m (5.5 ft) Tests</i>	75
6.1.2 <i>HFD Model Extension for Backwall Height Effects</i>	76
6.1.3 <i>Evaluation of Height Exponential Factor n</i>	78
6.1.4 <i>Re-Calibration of EHFD Coefficients</i>	79
6.2. MODEL PREDICTIONS VERSUS OBSERVED RESPONSE.....	82
6.2.1 <i>Selection of Strength Parameters for Use in Analysis</i>	82
6.2.2 <i>LSH Model Comparisons</i>	84
6.2.3 <i>Attempted Inference of Height Effect</i>	88
6.2.4. <i>Comparison of experimental data with analytical and classical solutions</i>	89
7. PRELIMINARY ANALYTICAL STUDIES ON SKEW ABUTMENTS	93
7.1. THREE-DIMENSIONAL FINITE ELEMENT SIMULATIONS OF NON-ROTATING SKEW WALLS	94
8. SUMMARY AND RECOMMENDATIONS	103
8.1 SCOPE OF RESEARCH	103
8.2 PRINCIPAL FINDINGS AND RECOMMENDATIONS	104
8.3 RECOMMENDATIONS FOR FUTURE RESEARCH	105
9. REFERENCES.....	107

List of Figures

Figure 1.1 Typical abutment configuration	2
Figure 1.2 Possible wall movements due to lateral loading	2
Figure 2.1 Curves showing development of normalized passive resistance as function of normalized wall displacement based on tests by various investigators (Rollins and Sparks, 2002).....	5
Figure 2.2 Lateral force-displacement backbone curves from UCD abutment test along with LSH prediction.	7
Figure 2.3 Lateral force-displacement backbone curves from Lemnitzer et al. (2009) (test T5.5) along with LSH model simulations with upper-bound and lower-bound strength parameters (Shamsabadi et al. 2010).....	8
Figure 2.4 Effective Abutment Stiffness and Capacity (Caltrans SDC 2010)	9
Figure 2.5 Hyperbolic Force Displacement Plot (modified from Shamabadi et al. 2010)	12
Figure 3.1 Actuator Configurations for Tests T8.0-1 & T8.0-2	14
Figure 3.2 Excavation and backfill geometry.....	14
Figure 3.3 Schematic Plan View of Specimen and Actuator Configuration.....	16
Figure 3.4a&b Reference Frame and Horizontal LVDT	16
Figure 3.5 Pressure Sensors on Fill-Side of Backwall.....	17
Figure 3.6 Photograph of actuator configuration (Elevation view from North).....	19
Figure 3.7 Abutment Wall Cracks Between Actuators 2 and 3L	20
Figure 3.8 Reaction Block Blowout at Actuator 4.....	20
Figure 3.9 W14X120 Sections to Strengthen Damaged Backwall	21
Figure 3.10 Diagonal Actuator Attached to W14X120 Steel Sections	21
Figure 3.11 Steel Plate and Angle Assembly to Strengthen Reaction Block	22
Figure 3.12 Repaired Edge of Concrete Reaction Block	23
Figure 4.1 Concrete Compressive Strengths of 5 Test Cylinders	25
Figure 4.2 Abutment Wall Reinforcement Cage	26
Figure 4.3 Formwork and Concrete Curing	26
Figure 4.4a Vibratory Drum Roller Compacting a Lift for T8.0-1.....	27
Figure 4.4b Hydraulic Vibrator and Manual “Whacker” Compacting a Lift (T8.0-2).....	28
Figure 4.5 Grain size distribution of bucket samples from T8.0-1 and T8.0-2	29
Figure 4.6 Compaction Curves for Various Samples from T8.0-1 and T8.0-2.....	29
Figure 4.7 Observed Correlation between Maximum Dry Unit Weight and Gradation Parameter D ₅₀	30
Figure 4.8 Sand Cone Testing between Lifts	30
Figure 4.9 Sand Cone Test Locations during Compaction for T8.0-1.....	31
Figure 4.10 Sand Cone Test Locations during Compaction for T8.0-2.....	32
Figure 4.11 Sand Cone R.C. Histograms for T8.0-1 (left) and T8.0-2 (right)	33
Figure 4.12 CPT Locations In Backfill for T8.0-1 (left) and T8.0-2 (right)	35
Figure 4.13 CPT data for T8.0-1 and T8.0-2	36
Figure 5. 1 Horizontal load - displacement relationship of baseline friction tests T5.5 & T8.0-1	42
Figure 5. 2 Vertical load-displacement relationship of baseline friction tests T5.5 & T8.0-1.....	42

Figure 5. 3 Horizontal and vertical load-displacement relationships for baseline friction test T8.0-2.....	43
Figure 5. 4 Observed sliding during baseline friction test	44
Figure 5. 5 Horizontal, vertical and total load displacement relationship of T8.0-1a	45
Figure 5. 6 Individual, measured actuator forces during test T8.01a.....	46
Figure 5. 7 Horizontal, vertical and total load displacement relationship T8.0-1b	47
Figure 5. 8 Individual actuator forces test T8.01b	47
Figure 5. 9 Horizontal, vertical and total load displacement relationship T8.0-2a.....	48
Figure 5. 10 Individual actuator forces T8.02a.....	49
Figure 5. 11 Visible striations on the steel base plate during T8.0-2b and T8.0-2c indicating movement along the wall-grout-plate interface.....	50
Figure 5. 12 Tests T8.02b and T8.0-2c horizontal, vertical and total load displacement relationships.....	51
Figure 5. 13 Combined horizontal and vertical load displacement relationships of test T8.01a&b.....	52
Figure 5. 14 Combined horizontal load displacement relationship for T8.0-1 a,b & c	54
Figure 5. 15 a & b: Idealized friction corrections for horizontal and vertical force components	55
Figure 5. 16 Passive load displacement relationships for T8.0-1	55
Figure 5. 17 Idealized friction correction for the ‘no backfill’ data recorded for test T8.0-2 for the horizontal force component	56
Figure 5. 18 Horizontal passive resistance P_x for T8.0-2	57
Figure 5. 19 Combined passive resistance P_x , P_z and P_p for T8.0-2	58
Figure 5. 20 Linear fit to initial and reloading stiffness using the passive force –displacement relationship	59
Figure 5. 21 Initial and reloading stiffness versus horizontal displacement	60
Figure 5. 22 Force-deflection relationship for T8.0-2a showing initial hardening behavior and evaluation of initial and unload/reload moduli	61
Figure 5. 23 Composite load-deflection relationship for T8.0-2 showing initial and unload-reload stiffness	62
Figure 5. 24 Initial and unload-reload stiffness vs. wall displacement. Note that the “initial” stiffness	62
Figure 5. 25 Wall soil interface friction angle for T8.0-1	64
Figure 5. 26 Wall soil interface friction angle for T8.02	64
Figure 5. 27 Pressure sensor recordings vs. time for T8.0-1a	66
Figure 5. 28 Pressure versus lateral wall displacement for T8.0-1b	66
Figure 5. 29 Earth pressure distribution for lateral displacement levels of 1.0, 3.5 and 5.0 inch	67
Figure 5. 30 Surface cracks on the backfill of T8.0-1 marked in green color	68
Figure 5. 31 Backfill upheave and major cracking at the location where the principal failure plane intersects with the surface	69
Figure 5. 32 Photograph of backfill upheave along the wingwalls of the specimen	69
Figure 5. 33 Plan view of surface cracks with highlighted regions for test T8.0-2	70
Figure 5. 34 Surface Cracks after test T8.0-2a. Left: Cracking near Grid A-1, Right: Cracking near Grid B-3	71
Figure 5. 35 Local Cracking after T8.0-2c	71
Figure 5. 36 Main Failure Surface Crack after T8.02c	72
Figure 5. 37 Elevation View of Backfill with Gypsum Column Locations for T8.0-2	72

Figure 5. 38 Combined images of backfill excavation and gypsum column ruptures for T8.0-2	73
Figure 5. 39 Trace off failure surface observed for T8.0-1	74
Figure 5. 40 Photograph showing the initiation of the major failure surface at the bottom of the wall for T8.0-1	74
Figure 6. 1 Variation of the backwall capacity per unit width versus normalized backwall height (reproduced from Shamsabadi <i>et al.</i> 2010).	78
Figure 6. 2 Variation of the normalized HFD coefficients versus normalized backwall height (reproduced from Shamsabadi <i>et al.</i> 2010).....	80
Figure 6. 3 Comparison of backbone curves computed using the proposed EHFD equations along with LSH curves and data from the T5.5 and UCD tests (reproduced from Shamsabadi <i>et al.</i> 2010).....	82
Figure 6. 4 Test results for T8.0-1 and LSH predictions of capacity using strength parameters from Section 6.2.1	85
Figure 6. 5 Test results for T8.0-2 and LSH predictions of capacity using strength parameters from Section 6.2.1	86
Figure 6. 6 Test results for T5.5 and LSH predictions of capacity using strength parameters from Section 6.2.1	87
Figure 6. 7 Test results for T5.5 and T8.0-2 to show apparent height effect	89
Figure 7. 1 Schematic for the generic configuration of straight/skew abutment finite element meshes	94
Figure 7. 2 Abutment backfill capacity versus backwall length.....	95
Figure 7. 3 Normalized abutment backfill capacity versus deck width	96
Figure 7. 4 Deformed finite element mesh at capacity for a backwall with skew angle 75° and the computed backbone curve.....	97
Figure 7. 5 Backbone curves for different backwalls lengths and skew angles.	98
Figure 7. 6 Sketch of the model configuration used in side-boundary influence studies.	99
Figure 7. 7 Backbone curves a 4.5 m wall with 45° skew for various side-boundary inclination angles.	100
Figure 7. 8 Backfill capacity versus the wingwall inclination angle.	101

List of Tables

Table 1.1 Overview of UCLA Full-Scale Tests	3
Table 3.1 List of sensor functionality for all test segments.....	17
Table 4. 1 Sand Cone Test Results for T8.0-1.....	32
Table 4. 2 Sand Cone Test Results for T8.0-2.....	33
Table 4. 3 Laboratory Results for Min. and Max. Dry Densities for Backfill Specimen	34
Table 4. 4 Triaxial strength test results for SE30 sand	37
Table 5. 1 Comparison between measured capacities from hydraulic equipment and earth pressure sensors.	67
Table 6. 1: Abutment Backfills Parameters for UCLA and UCD Abutment Tests.....	76
Table 6. 2: EHFD coefficients back-calculated using LSH simulation data.....	79
Table 6. 3: Input Parameters for Comparison Study.....	89
Table 6. 4: Comparison of K _p and P _p from experiment and analyses.....	90

Acknowledgments

Support for this research was provided by the California Department of Transportation under Research Contract No. 59A0655 (and amendments thereto), which is gratefully acknowledged. We would like to acknowledge the valuable assistance and technical support of Caltrans staff in this project, particularly Anoosh Shamsabadi and Li-Hong Sheng. George Cooke of GB Cooke Inc is recognized for his assistance in specimen construction and contract administration. Several undergraduate and graduate students assisted in this project at various stages including Abdou Diop, Hilarion Marapao, Jay Merani, and Edward Reinert.

The authors gratefully acknowledge that this research was conducted with equipment purchased and integrated into the NEES@UCLA Equipment Site with support from NSF Cooperative Agreement CMS-0086596.

Disclaimer Statement

This document is disseminated in the interest of information exchange. The contents of this report reflect the views of the authors who are responsible for the facts and accuracy of the data presented herein. The contents do not necessarily reflect the official views or policies of the State of California or the Federal Highway Administration. This publication does not constitute a standard, specification or regulation. This report does not constitute an endorsement by the Department of any product described herein.

For individuals with sensory disabilities, this document is available in Braille, large print, audiocassette, or compact disk. To obtain a copy of this document in one of these alternate formats, please contact: the Division of Research and Innovation, MS-83, California Department of Transportation, P.O. Box 942873, Sacramento, CA 94273-0001.

Executive Summary

This research involved analysis and field testing of abutment backwalls, which are an important component of foundation support for highway bridges. Caltrans Seismic Design Criteria (SDC, 2010) describe the load-deflection relationship for abutment wall-backfill interaction with a bilinear relationship defined by a stiffness and capacity. Stiffnesses are specified separately for clay and sand backfills as 25 and 50 kips/in per foot of wall width (145 and 290 kN/cm/m), respectively, for walls 5.5 ft (1.67 m) in height. For this same wall height, capacity is defined from a uniform pressure of 5.0 ksf (240 kPa) acting normal to the wall. Both stiffness and capacity are assumed to scale linearly with wall height. Compaction conditions of the backfill materials are not directly considered in assigning stiffness or strength parameters.

In this research we address the scaling of abutment wall lateral response with wall height and compaction condition through testing and analytical work. The analytical work was undertaken to develop hyperbolic curves representing the load-deflection response of backwalls for two backfill material types as a function of wall height. The scaling of backwall resistance with height is expressed by an exponent n applied to a normalized wall height; we find that the height scaling exponent can be taken as 1.05 and 1.56 for the same clay and sand backfill materials considered in SDC (2010), respectively.

We tested two wall-soil specimens 8 ft (2.4 m) in height with identical characteristics except for the level of compaction of the sandy backfill. One specimen (denoted T8.0-1) has as-compacted relative densities ranging from approximately $D_r = 0.4\text{-}0.6$ (which was lower than specified) and the other (T8.0-2) had an unusually high level of compaction of $D_r = 0.9\text{-}1.0$. Other than the degree of compaction, the two specimens are essentially identical in terms of dimensions, material gradation, and boundary conditions imposed during testing. The wall height in these tests is 8.0 ft (2.4 m), which represents an approximate upper-bound backwall height; in previous work we tested a similar specimen with a height of 5.5 ft (1.67 m). The backfill material is a well graded silty sand known in the construction industry as SE-30. The boundary condition imposed on the test is horizontal displacement towards the backfill without rotation (torsion or rocking) or uplift.

The modest- D_r specimen (T8.0-1) exhibits nearly elastic-plastic response with negligible strain softening. The peak resistance was approximately 700 kips (3114 kN), which corresponds

to a passive earth pressure coefficient of $K_p=10$, and occurred with a wall-soil interface friction that is approximately half of the soil friction angle. The high- D_r specimen (T8.0-2) exhibits a strongly strain softening response with a peak resistance of approximately 1650 kips (7340 kN) and large-strain (approaching residual) capacity of approximately 1100 kips (4900 kN). These capacities correspond to K_p values of 24 and 17 for peak and large-strain conditions, respectively. As before, the wall-soil interface friction angle was approximately half of the soil friction angle. Measured earth pressure distributions against the wall were found to be reverse triangular, confirming classical theories of passive pressure distribution.

We characterize the soil strength parameters using drained triaxial testing over a range of normal stresses that represent in situ conditions. We evaluate peak strength parameters for the dense backfill configuration and apply corrections for plane strain effects and for the looser backfill configuration. We also estimate critical state parameters using the test results and literature. Due to scatter in the test data, there is some uncertainty in the strength parameters which we quantify and consider in the analysis. When these strength parameters are used in log-spiral hyperbolic (LSH) simulations of the backfill response, we find modest under prediction of the peak response for the upper bound of the considered range of strengths; central values of strength parameters produce more substantial under prediction. Nonetheless, the degree of underprediction is modest relative to the substantial differences in capacity between specimens T8.0-1 and T8.0-2. Those large variations in capacity between specimens are well captured by the analysis, suggesting that the LSH method can account for the effects of compaction condition on the wall capacity. The LSH simulations are also able to capture variations in specimen response for different wall height.

We recommend that the height scaling effects in future versions of the SDC be modified to more realistically capture the different trends for cohesive and granular backfills. For granular backfill, capacity should scale by an exponent $n = 1.5\text{--}2.0$. We also recommend that compaction condition be considered in the specification of stiffness and capacity. This research has demonstrated the substantial, first-order impact of compaction level which can vary substantially in the field from site-to-site due to variations in construction quality.

1. Introduction

Bridge structures are typically constructed with earth abutments at their ends. As shown in Figure 1.1, typical components of bridge abutments in current California design practice include a backwall, two wingwalls, a support foundation (spread footings or piles) and the retained soil. The behavior of the backwall when struck by a bridge deck displacing longitudinally during earthquake shaking is a significant, yet poorly understood, aspect of bridge design. Lam and Martin (1986) describe abutment performance as the “largest unknown in the area of bridge foundations.” This statement arguably remains true today, despite significant progress in recent years in the testing and simulation of abutment performance. This report examines the results of research that has investigated abutment wall behavior. The principal objective of this report is to describe a series of full scale field experiments of abutment performance for specimens with a prescribed set of boundary conditions pertinent to Caltrans seismic design practice. It also reviews the current state of knowledge from both analytical and experimental perspectives. In addition to the experiments and literature synopses, this report presents the results of pre- and post-test analyses as well as analytical results for skewed abutments, which were not physically tested in this endeavor.

Abutment backwalls in current practice are designed to break away from their foundations when struck by the bridge superstructure and subsequently displaced in the bridge longitudinal direction. This wall displacement occurs between two sidewalls that are perpendicular to the backwall, as illustrated in Figure 1.1. Figure 1.2 highlights several possible rigid-body motions the backwall could undergo as it is forced into the supporting backfill; our experimental setup reproduces simple horizontal translation without rotation as illustrated in the leftmost schematic, which is understood to be the most realistic response based on discussions with Caltrans engineers.

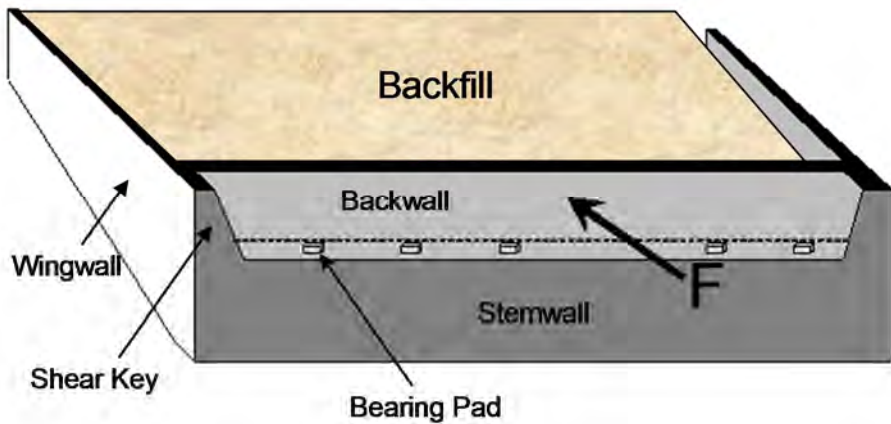


Figure 1.1 Typical abutment configuration

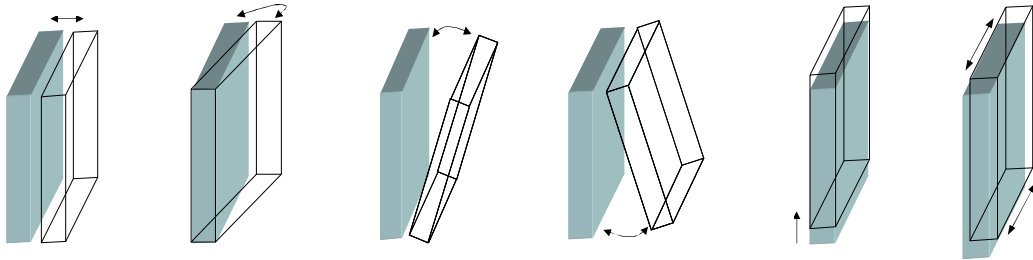


Figure 1.2 Possible wall movements due to lateral loading

Following this introduction, Chapter 2 reviews previous research on abutment walls, with an emphasis on (1) previous full-scale field experiments and (2) analysis tools used for evaluating abutment load-deflection behavior. Chapter 3 describes the test set-up, sensor layout, and control system used in the testing. The control system enforces the leftmost boundary condition depicted in Figure 1.2. In Chapter 3, we also describe structural repairs undertaken over the course of the research. Material properties of the full-scale specimen, for both the backwall and backfill soil, are described in Chapter 4. Test protocol, results, and compliance with intended boundary conditions are discussed in Chapter 5. Also included in Chapter 5 is documentation of the passive wedge soil failure surface observed during the experiment, which was obtained from both ground surface crack observations and post-test excavation. Chapter 6 describes analytical studies investigating the effect of abutment wall height on the load-deflection behavior and compares the results of those studies to the experimental results from this research. Chapter 7 describes additional analytical work used to design experimental

configurations for skew-type abutments, which was not carried out in this research. Finally, Chapter 8 provides a summary of major findings and future research needs.

The experimental work chronicled in this report was performed at the UCLA-Caltrans test site in Hawthorne, CA, and involved two 8.0 ft (2.4 m) backfills referred to as T8.0-1 and T8.0-2. Table 1.1 summarizes the various backwall tests undertaken at this test site. Test T5.5 was completed in previous research and involved a 5.5 ft (1.68 m) tall backfill (Lemnitzer et al. 2009). The first 8.0 ft (2.4 m) specimen (T8.0-1) had two distinct testing phases referred to as T8.0-1a and T8.0-1b. The second 8.0 ft (2.4 m) specimen (T8.0-2) had three test phases referred to as T8.0-2a, T8.0-2b, and T8.0-2c. Dates for each test sequence, along with method of compaction information and other notes, are given in the table.

Table 1.1 Overview of UCLA Full-Scale Tests

Test ID	Backfill Height [ft (m)]	Test Date	Compaction Method	Notes
T5.5	5.5 (1.68)	July 2006	Vibratory Plate and Small Handwacker	Testing completed in one attempt
T8.0-1a	8.0 (2.44)	July 2009	Large Vibratory Roller	Actuator capacity exceeded
T8.0-1b	8.0 (2.44)	August 2009		Test cont'd with additional actuator; pushed to failure
T8.0-2a	8.0 (2.44)	July 2010	Vibratory Plate and Small Handwacker	Steel baseplate added; testing halted by structural damage to wall and reaction block
T8.0-2b	8.0 (2.44)	December 2010		Gap closing generated softer initial stiffness; pump overheated and limited maximum deliverable force
T8.0-2c	8.0 (2.44)	December 2010		Initial stiffness similar to 8.0-2a; force level exceeded 8.0-2b; softening at end of test

2. Literature Review

When a backwall is pushed into its backfill, the principal resistance to lateral displacement is provided by shear resistance developed in the soil. The ultimate capacity is reached when the lateral resistance achieves a state of passive earth pressure, which is typically calculated using log-spiral methods (Terzaghi, 1943). Recent research has focused on load-deflection behavior of abutment walls up to the point of passive failure through experimental testing and analytical simulations. Testing efforts have largely focused on walls of a height of 5.5 ft (1.68 meters), a typical level for Caltrans abutments. Section 2.1 focuses on two of these testing programs for this wall height, which together form the basis of the current California Seismic Design Criteria (SDC, 2010). Section 2.2 describes the SDC criteria pertaining to the design of abutment walls, which are based on elastic-perfectly plastic representations of backfill behavior. Section 2.3 describes more advanced nonlinear procedures for the simulation of abutment wall-backfill response. For each of these topics, the discussion is focused on those aspects of the literature with direct influence on this project. References are made to additional manuscripts with more exhaustive literature summaries for the respective subjects.

2.1 Large-scale tests of abutment systems

A number of tests have been performed in laboratories at reduced scales to investigate passive earth pressures against retaining structures (Tschebotarioff and Johnson, 1953; Schofield, 1961; Rowe and Peaker, 1965; Mackey and Kirk, 1968; Narain et al., 1969; James and Bransby, 1970; Roscoe, 1970; Carder et al., 1977; Fang et al., 1994; Gadre and Dobry, 1998). Many of these tests have been used to develop empirical relationships between passive pressure formation and normalized wall displacement ($K/(K_p)$ vs. Δ/H); where K is the lateral earth pressure corresponding to wall displacement Δ , K_p is the passive earth pressure coefficient, and H is the

wall height. Results from selected laboratory-scale experiments, and some field-scale experiments, are summarized in Figure 2.1 Curves showing development of normalized passive resistance as function of normalized wall displacement based on tests by various investigators (Rollins and Sparks, 2002). This section, however, focuses on full-scale testing. While laboratory tests certainly hold merit, full scale tests with proper boundary conditions are generally preferred for the development of practical design recommendations. Not only do the stresses acting within the full-scale experimental specimens replicate those in real backfills, but they also represent realistic soil types and means of construction. In particular, we will investigate two of the experiments currently serving as the basis of the Caltrans Seismic Design Criteria (2010), although it should be noted a more complete review of several large-scale experiments is available in Stewart et al. (2007).

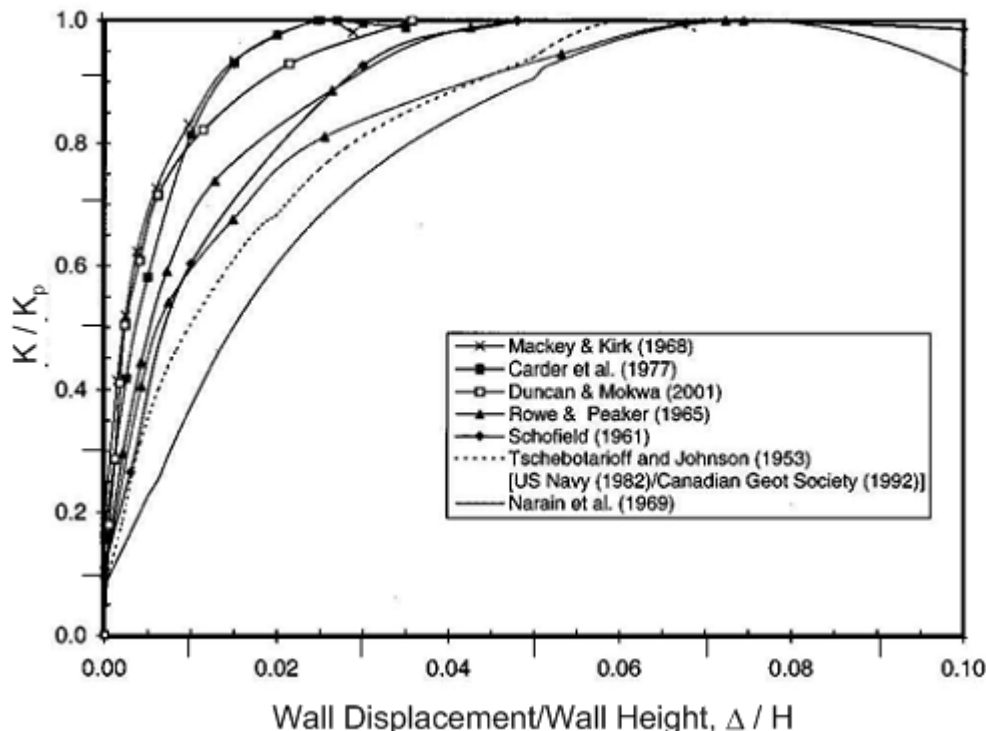


Figure 2.1 Curves showing development of normalized passive resistance as function of normalized wall displacement based on tests by various investigators (Rollins and Sparks, 2002)

One of the first large-scale tests of passive earth pressures was the cyclic tests of an abutment by Romstad et al. (1995). The test involved a 10.0 ft (3.05 m) wide by 5.5 ft (1.68 m) tall wall specimen that was displaced both into the backfill (simulating longitudinal deck excitation) and along the backfill (simulating transverse excitation). The backfill was comprised

of three zones. The first zone, immediately behind the backwall, consisted of clean pea gravel with no reported strength or compaction properties. The second zone was a granular soil wedge located adjacent to the pea gravel zone and compacted to an average of 98% relative compaction based on the modified Proctor standard. Consolidated-drained triaxial compression tests of this material indicated a friction angle of 41° over the minor principal stress range of 1 – 4 ksf (50–110 kPa). The third zone consisted of the weakest (and therefore most critical) material, referred to as Yolo loam. The Yolo loam was a compacted, low-plasticity clayey silt material with liquid limit (LL) and plasticity index (PI) equal to 34% and 10.5%, respectively. The soil was compacted to a minimum of 90% relative compaction, but no information on water content control during compaction was reported. Unconfined compression tests yielded average deviatoric stresses at failure ranging from approximately 1.7 – 4 ksf to 15 – 19 ksf (80-200 kPa to 700-900 kPa). Since the compacted soil was not fully saturated, one would expect stress-dependent shear strength (i.e. ϕ not equal to 0); however based on the recommendations of Romstad et al. (1995), high water contents were assumed along with a representative undrained strength of $S_u = 2.0$ ksf (100 kPa).

Lateral load-deflection data from this test is shown by the discrete symbols in Figure 2.2 (the modeling is described subsequently). The failure surface was observed to plunge down into the backfill from the base of the wall before rising towards the surface at increasing distance from the wall. The induced failure could be described as generally two-dimensional in geometry because of the influence of a rigid connection of concrete wingwalls to the backwall. The ultimate passive pressure of the abutment wall was measured to be approximately 5.5ksf (265 kPa), which was reached at a lateral displacement of 5.4 inch (16.8 cm, 10% of the abutment height). The secant stiffness at 50% of load capacity per unit width of the backwall was calculated to be approximately 25 kips/in/ft (145 kN/cm/m) (Shamsabadi et al. 2007). This test is hereafter referred to as the UCD abutment wall test. The performance of this specimen forms the experimental basis for current Caltrans Seismic Design Criteria (SDC) for cohesive backfill materials.

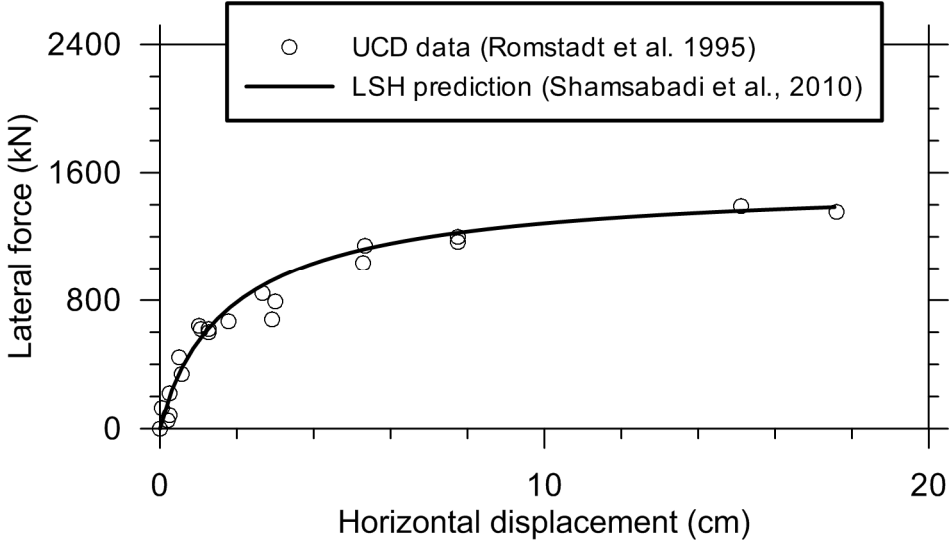


Figure 2.2 Lateral force-displacement backbone curves from UCD abutment test along with LSH prediction.

Lemnitzer et al. (2009) tested a full scale bridge abutment wall at the Caltrans-UCLA field test site in Hawthorne, CA (test T5.5 in Table 1.1). The wall, measuring 8.5 ft (2.6 m) tall by 15.0 ft (4.57 m) wide by 3.0 ft (0.91 m) thick, was displaced horizontally into a granular (SE-30) backfill that extended 2.0 ft (0.61 m) below base of wall and was 5.5 ft (1.68 m) tall relative to the base of the abutment wall. Plywood wingwalls were constructed to laterally confine the backfill specimen. The backfill was compacted to over 95% of modified Proctor relative compaction. The SE-30 backfill is a silty sand material with low fines content (5-10%). As described by Lemnitzer et al. (2009), strength testing performed on this material followed a protocol specified by Earth Mechanics (2005) in which triaxial drained shear of a virgin specimen was performed at a low confining pressure, after which confining stress was increased to two higher levels, and re-shearing occurred at each level. The peak shear strengths from these tests are bracketed by total stress Mohr-Coulomb strength parameters of $c = 300$ psf (14 kPa) and $\phi = 40$ deg (lower bound) and $c = 500$ psf (24 kPa) and $\phi = 39$ deg (upper bound). It should be recognized that the Earth Mechanics test protocol properly represents the “undisturbed” response of the compacted soil at the lowest confining pressure only. At higher confining stresses, the material is already at or near critical state, so dilatancy effects would be expected to be suppressed.

Testing was performed without allowing wall rotation or vertical displacement. Cyclic loading was applied, but gapping was not allowed to occur at the wall-backfill interface during unload cycles. Lateral load-deflection data from this test are shown in Figure 2.3. The ultimate

(and the deepest) failure surface extended down from the bottom of the abutment backwall in a nearly log-spiral shape, ultimately reaching the backfill ground surface at a horizontal distance behind the wall of approximately three times the height of the backwall. The lateral capacity of the abutment backfill per unit wall width was measured to be approximately 16000 kip/ft (480 kN/m) at a lateral displacement of 2.0 inch (5 cm; 3% of abutment height). The ultimate residual capacity was approximately 14500 kip/ft (440 kN/m), which was reached at a lateral displacement of 3.3 inch (8.5 cm). This corresponded to an ultimate residual capacity normalized by wall area of 5.2 ksf (270 kPa). The secant stiffness at 50% of load capacity per unit width of the backwall was calculated to be approximately 50 kips/in./ft (290 kN/cm/m). The performance of this specimen forms the experimental basis for the Caltrans SDC provisions for granular backfill materials.

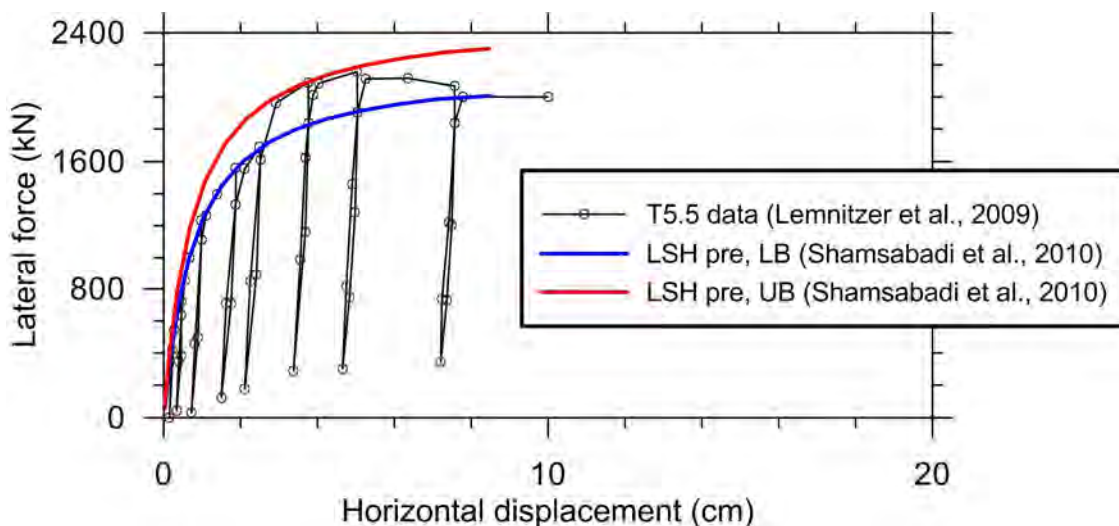


Figure 2.3 Lateral force-displacement backbone curves from Lemnitzer et al. (2009) (test T5.5) along with LSH model simulations with upper-bound and lower-bound strength parameters (Shamsabadi et al. 2010)

2.2 Caltrans Seismic Design Criteria

Section 7.8 of the 2010 Caltrans Seismic Design criteria outlines the design standard for longitudinal abutment response. The representation of wall-backfill behavior in the design standard consists of an elastic-perfectly-plastic spring suitable for static or pushover-type analyses. The properties of the spring are given in Figure 2.4, where K_{eff} represents the effective abutment stiffness term, and P_x represents the maximum spring capacity for abutment type x

(x =‘bw’ for backwalls and ‘dia’ for diaphragm walls). Both stiffness model parameters are derived from the experimental results of Romstad et al. (1995) and Lemnitzer et al. (2009) for cohesive and granular backfill materials, respectively. As described in Section 2.1, both abutment tests were performed using 5.5 ft (1.68 m) tall walls.

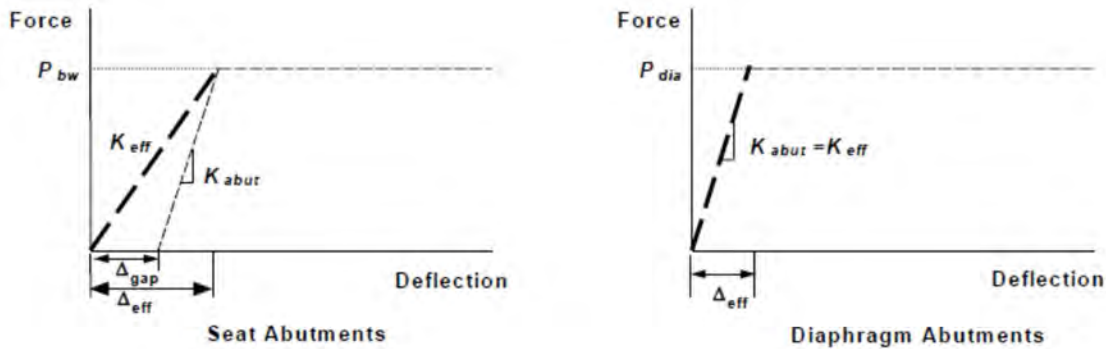


Figure 2.4 Effective Abutment Stiffness and Capacity (Caltrans SDC 2010)

The effective stiffness is given as 50 kip/in per foot of wall width (or 290 kN/cm per meter of wall width) — for fill material conforming to the requirements of Caltrans Standard Specifications; for material not in conformance with the Standard Specification, the stiffness value is halved (applied for clayey materials). For wall heights different from 1.68 m, the stiffness is proportioned to the actual backwall height as follows:

$$K_{eff} = \begin{cases} K_{eff,1.68} \times w \times \left(\frac{h}{1.7} \right) & (\text{m, kN}) \\ K_{eff,5.5} \times w \times \left(\frac{h}{5.5} \right) & (\text{ft, kip}) \end{cases} \quad (2.1)$$

where K_{eff} is the initial stiffness, $K_{eff,1.68}$ is the stiffness for a 1.68 m wall height per unit width as given above, w is the wall width, and h is the backwall height. Note that the height adjustment factor imposes a depth-invariant assumption of lateral stress distribution.

The capacity of the backwall spring is represented in stress units as 5.0 ksf (239 kPa) for the standard 5.5 ft (1.68m) backfill height. These values are loosely based on residual capacities (but not the actual stress distributions) obtained from the field tests described in Section 2.1. The capacity adjustment for different wall heights assumes linear scaling with wall height, similar to the stiffness derivations, as follows:

$$P_{bw} \text{ or } P_{dia} = \begin{cases} A_e \times 239 \text{ kPa} \times \left(\frac{h_{bw} \text{ or } h_{dia}}{1.7} \right) & (\text{m, kN}) \\ A_e \times 5.0 \text{ ksf} \times \left(\frac{h_{bw} \text{ or } h_{dia}}{5.5} \right) & (\text{ft, kip}) \end{cases} \quad (2.2)$$

The stiffness and capacity height factor were investigated in the present research through means of numerical analysis and full scale testing, both of which indicate that pressure scales with height at greater rates than the linear relationships presented above. This phenomenon is described further in Chapter 6, where we propose calibrated models for the backfill depth effect that depend on soil type.

2.3 Simulation Models of Lateral Response of Bridge Abutments

Methods available for analyzing the behavior of laterally loaded abutment backfill include closed-form equations for the backbone curve, limit equilibrium methods utilizing methods of slices, and continuum modeling (finite element or finite difference analysis). For the present discussion we describe two widely implemented methods in Caltrans practice: log-spiral hyperbolic (LSH) which is a limit equilibrium approach coupled with assumed hyperbolic stress-strain behavior in soil, and closed hyperbolic force-displacement (HFD) relationships for the backbone curve.

2.3.1 Log-Spiral Hyperbolic (LSH) Methods

The LSH model is a plane-strain model that was developed to estimate nonlinear force-displacement relationships for abutment walls based on the wall dimensions and backfill soil properties (Shamsabadi et al. 2007). This model is based on a limit equilibrium method for ultimate capacity that employs logarithmic spiral failure surfaces, coupled with a modified hyperbolic soil stress-strain relationship to evaluate load-deflection behavior. Unlike classical limit-equilibrium methods, shear resistance of the soil is not assumed to be simultaneously mobilized across the full failure surface in this approach, but instead varies as a function of progressive failure and strain localization in the backfill. Each progressive failure surface is associated with the mobilized shear resistance and strain of the backfill. Dubrova (1963) referred to such mobilized failure surfaces as “quasi-rupture lines.” The model neglects the effects of inertia in the soil backfill.

Input parameters for LSH models include strength parameters (e.g. c and ϕ), Poisson's ratio (v), strain at 50% of ultimate capacity from triaxial compression tests on soil specimens, and failure ratio (R_f). Strength parameters are ideally obtained from test samples representative of the full-scale specimen. For the remaining model parameters, magnitudes can be established according to literature recommendations (see Shamsabadi et al. 2007, 2010 for further details). Figure 2.2 and Figure 2.3 show LSH model predictions by Shamsabadi et al. (2010) relative to test data for the UCD and T5.5 tests. In the case of the UCD test, the fit is reasonably good. For T5.5, the upper bound strengths better estimate the peak lateral load capacity, whereas lower bound strengths match residual capacity.

2.3.2 Models Based on Hyperbolic Stress-Strain Relationship for Soil

Hyperbolic models have long been used to approximate load-deflection and stress-strain relationships for problems in soil mechanics (Duncan and Chang, 1970). A number of investigators have adapted various forms of hyperbolic models to simulate the load-deflection behavior of retaining walls pushed into backfill, and an extensive review of these models can be found in Stewart et al. (2007). Typically, these simulations build upon the basic form of the hyperbolic model, which can be written as

$$P(y) = \frac{ay}{1+by} \quad (2.3)$$

where P = lateral force on retaining wall corresponding to lateral deflection y , and a and b are constants that are determined differently in various forms of the hyperbolic model. Shamsabadi et al. (2007) derive parameters a and b as follows:

$$a = \left(2K_{50} - \frac{P_{\max}}{y_{\max}} \right), \quad b = 2 \left(\frac{K_{50}}{P_{\max}} - \frac{1}{y_{\max}} \right) \quad (2.4)$$

where P_{\max} is the maximum abutment force (per unit width of wall) developed at maximum displacement y_{\max} . K_{50} is the average abutment stiffness evaluated as $P_{\max}/(2y_{50})$, where y_{50} is the displacement corresponding to half the maximum abutment force. Figure 2.5 illustrates these parameters on a HFD plot.

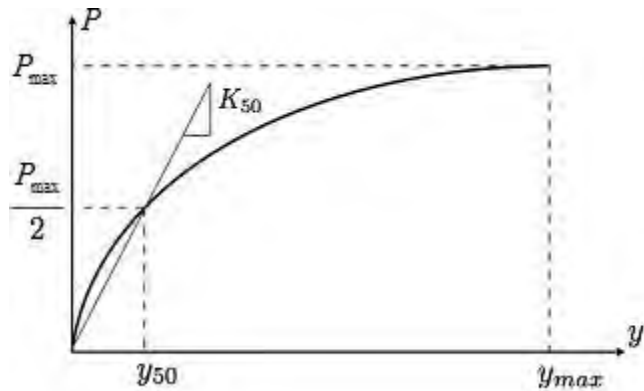


Figure 2.5 Hyperbolic Force Displacement Plot (modified from Shamabadi et al. 2010)

Shamsabadi et al. (2007) investigates how these three parameters (P_{max} , y_{max} , and K_{50}) affect the HFD model and makes recommendations for either cohesive or granular type backfill materials. In their report, presumptive values for all three parameters based on eight set of experimental data were used to fit HFD relationships for materials that are either clay or sand. The parameters recommended for cohesive backfill were $P_{max} = 30.4$ kip/ft (444 kN/m), $y_{max} = 6.6$ in (16.8 cm), and $K_{50} = 25$ kip/in.ft (145 kN/cm/m); the resulting force-displacement relationship was

$$P(y_i) = \begin{cases} \frac{y_i}{0.00383 + 0.00204y_i} & (y_i \text{ in cm, } P_{max} \text{ in kN per m of wall}) \\ \frac{y_i}{0.0220 + 0.0297y_i} & (y_i \text{ in inches, } P_{max} \text{ in kip per ft of wall}) \end{cases} \quad (2.5)$$

The same process was applied for granular backfill, with recommended parameters $P_{max} = 30.4$ kip/ft (444 kN/m), $y_{max} = 3.3$ inch (8.4 cm), and $K_{50} = 50$ kips/in/ft (290 kN/cm/m); the resulting force-displacement relationship for sandy backfill was

$$P(y_i) = \begin{cases} \frac{y_i}{0.00191 + 0.00204y_i} & (y_i \text{ in cm, } P_{max} \text{ in kN per m of wall}) \\ \frac{y_i}{0.0110 + 0.0297y_i} & (y_i \text{ in inches, } P_{max} \text{ in kip per ft of wall}) \end{cases} \quad (2.6)$$

3. Experimental Setup

3.1 Loading System & Specimen Configuration

Each of the backwall specimens were tested at the UCLA-Caltrans test site in Hawthorne, CA. The wall specimen consists of a full scale (in height) backwall with dimensions of 8.5 ft (2.6 m) in height, 15.0 ft (4.57 m) in width, and 3.0 ft (0.91 m) in thickness. The wall is located at a clear distance of 9.5 ft (2.90 m) from a reaction block dimensioned 6.0 ft (1.83 m) tall, 24.0 ft (7.32 m) long, and 12.0 ft (3.66 m) wide. The reaction block provides a load capacity of 3000 kips (13300 kN) in the linear range, which well exceeds the forces applied to the test specimen. Six hydraulic actuators were installed in horizontal and diagonal orientations between the reaction block and the test specimen to control the horizontal, vertical, and rotational displacements of the backwall. This setup was similar to the T5.5 backwall experiment with one difference: one additional center actuator was placed next to the center Actuator 3 during the 8.0-1 tests to address the greater lateral capacity associated with the increased backfill height. The diagonal actuators were used to prevent an uplift movement of the wall when pushed laterally into the backfill material to enable the zero-uplift boundary condition as shown in Figure 1.2a. A photograph of the installed actuators on site is shown in Figure 3.1.

Testing was performed under displacement control, in which horizontal displacements (normal to the wall) were prescribed while all other displacements and all rotations were held to zero. Forces and displacements of all actuators were recorded using an MTS control system and the corresponding Flextest GT Software. Further details on the control system are provided in Section 3.3.

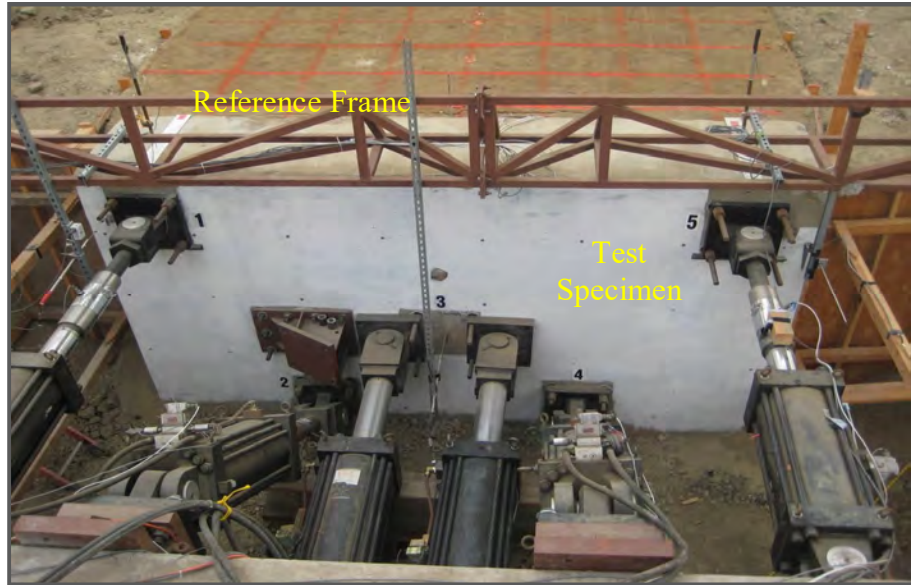


Figure 3.1 Actuator Configurations for Tests T8.0-1 & T8.0-2

The natural clayey soils at the site were excavated as shown schematically in Figure 3.2 so that the failure plane would develop within the backfill material. Wingwalls were simulated using 1.0 inch (2.5 cm) plywood sheathing erected on either side of the backwall. These assemblies were located approximately 1.0 ft (0.3 m) from both sides of the backwall, and were braced with stakes anchored into the native slopes. To minimize friction between the sidewalls and the backfill material, the plywood was furnished with several layers of PVC foil. During compaction of the backfill lifts, material was also placed and compacted behind the wingwalls to minimize bulging or displacement of the plywood during setup and testing.

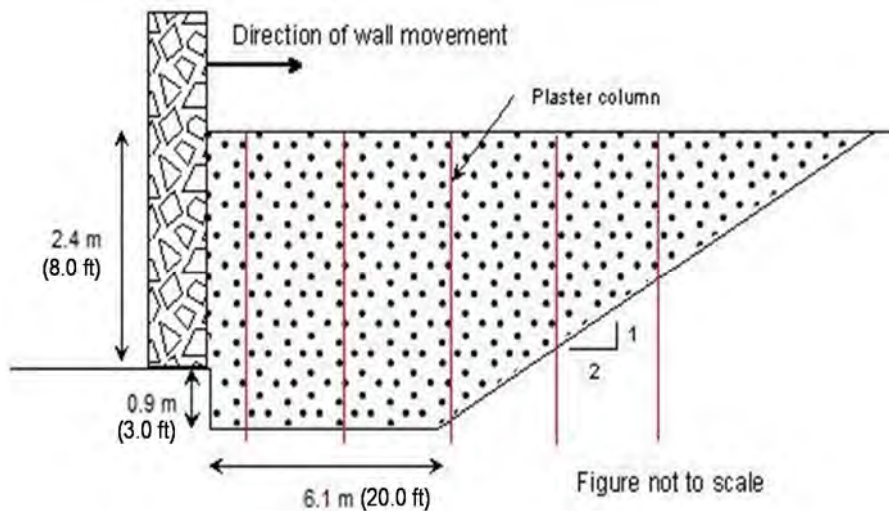


Figure 3.2 Excavation and backfill geometry

Tests T5.5 and T8.0-1 were conducted with the concrete abutment backwall resting on the natural underlying soil. After many push-pull cycles from these previous experiments (T5.5 & T8.0-1) as well as due to flooding of the construction site during the winter season 2009/2010, it was observed that the abutment wall had begun to settle into the underlying native soil. Since the base of the wall was cast directly on the soil below, it created a rough surface that would “dig in” as significant displacement demands moved the wall back and forth. This settlement was creating difficulties in attaching the actuator equipment to the wall as the connection points in the wall were no longer at the proper elevation. To prevent further settlement and possible damage, we added a thick steel plate below the concrete wall before conducting test T8.0-2. The intent of the new plate was to relocate the sliding mechanism below the wall to the concrete-steel interface instead of the soil contact, thus keeping the underlying soil intact and hinder further settlement. A weak grout was applied between the wall and the plate to stabilize the wall during the construction phase. Once the wall assembly was repositioned, a combination of sledgehammering the baseplate and tilting the wall with the actuators broke the seal at the wall-plate interface.

3.2 Sensor Layout

Five Transtek Linear Variable Differential Transducers (LVDTs) were installed to control the wall movement for both 8.0 tests. Three horizontally aligned LVDTs were used to measure and control the individual and average horizontal displacement of the wall. These LVDTs were located next to Actuators 1, 3, and 5. A free-standing hollow tube-section steel space truss provided a global reference frame positioned 2.0 ft (0.6 m) from top of backwall as shown in Figure 3.1. Two vertically oriented LVDTs mounted directly to the frame and the extensible ends contacted a clean, smooth steel plate to detect and control the zero-uplift boundary condition. The diagonal actuators adjusted their force levels to enforce zero vertical wall movement. Figure 3.2 is a schematic showing the instrumentation and actuator installation. Figure 3.4 a&b are photographs of the instrumentation setup.

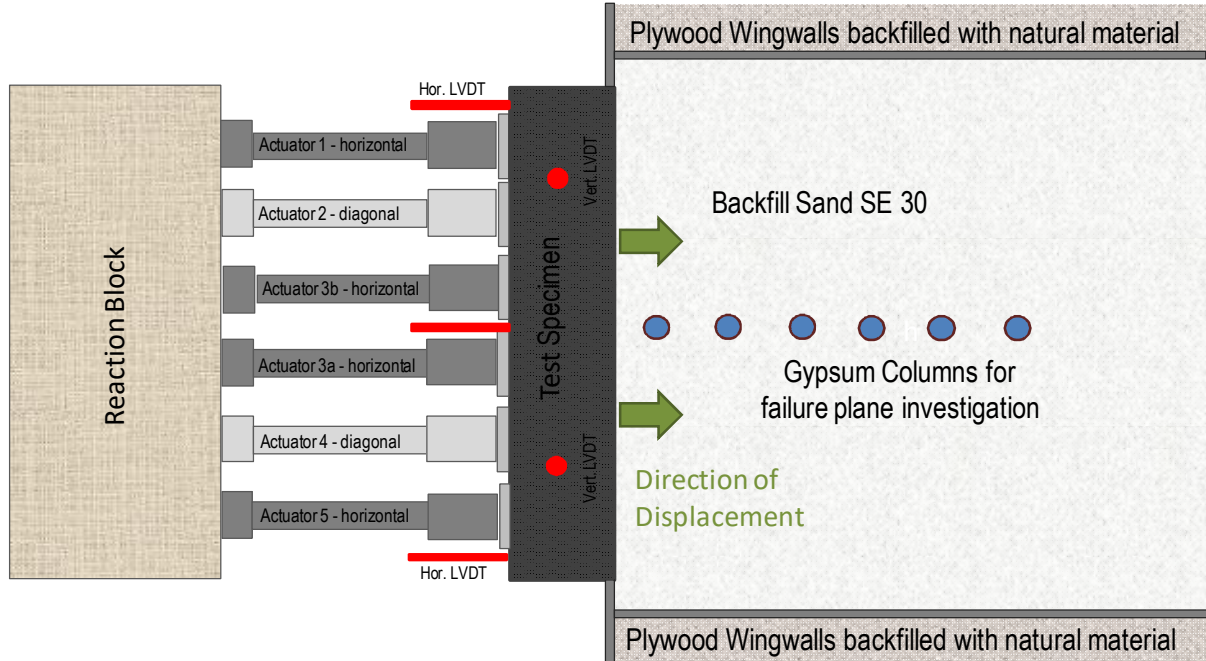


Figure 3.3 Schematic Plan View of Specimen and Actuator Configuration

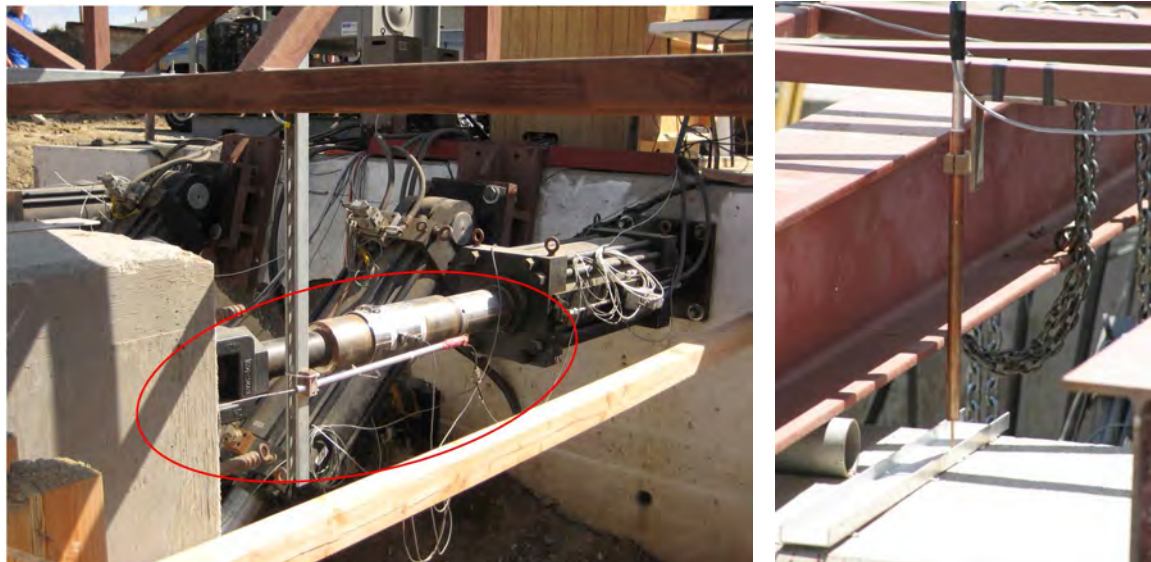


Figure 3.4a&b Reference Frame and Horizontal LVDT

Sixteen pressure sensors were installed into the backwall at the interface with the backfill. Eight sensors were aligned vertically near the center of the wall before test T8.0-1 and provided reliable pressure measurements for all lateral displacement levels. Eight additional sensors were

installed horizontally across two rows as shown in Figure 3.5 before the 8.0-2 test. All pressure sensors are 4.0 inch (10 cm) in diameter (sensing area is 3.75 inch (9.5 cm) in diameter) and are approximately 1 inch (2.5 cm) thick. Each sensor contains a hermetically sealed full-bridge load cell capable of reliably registering up to 13,500 psf (675 kPa). Most sensors provided meaningful pressure readings for the tests conducted (T8.0-1a&b). Several sensors experienced damage due to exposure to weather and corrosion, and possibly damage during the backfill placement and compaction. This affected only test T8.0-2 a-c. A summary documenting the functionality of each sensor during the various test segments is shown in Table 3.1

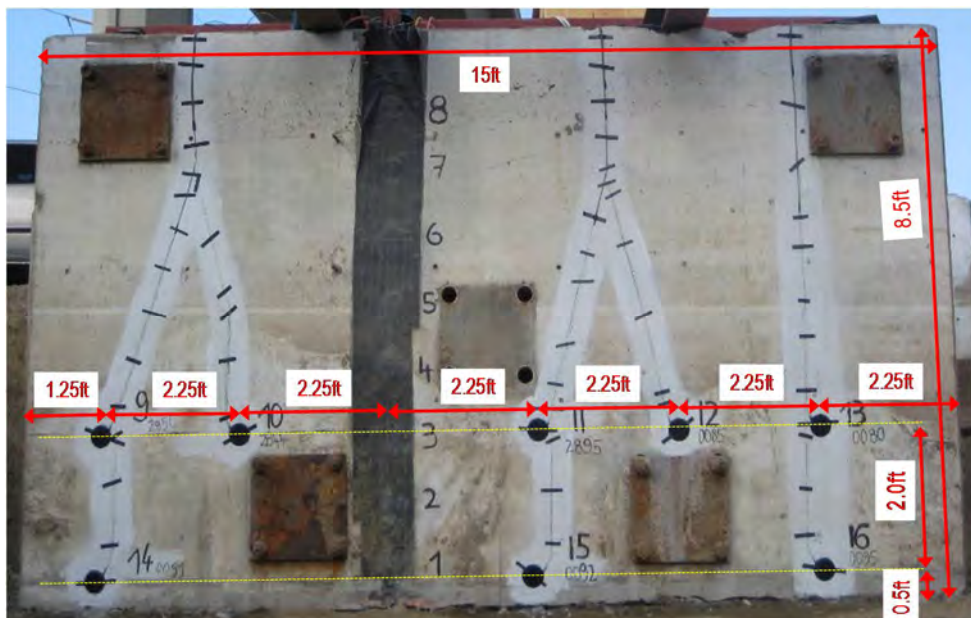


Figure 3.5 Pressure Sensors on Fill-Side of Backwall

Table 3.1 List of sensor functionality for all test segments

Test/Sensor	1	2	3	4	5	6	7	8	9	10	11	12	13	14	15	16
8.0-1 a									NA	NA	NA	NA	NA	NA	NA	NA
8.0-1 b									NA	NA	NA	NA	NA	NA	NA	NA
8.0-2 a		red				red			green					red		red
8.0-2 b		red	red	yellow			red		red			yellow	red	yellow		red
8.0-2 c	green				green			red		green		red	green	red	green	red

	reliable data
	data, but possibly unreliable
	no data, sensor/cable failure

3.3 Control System

A five-channel MTS Flextest GT Control System was used to record and control the forces and displacements of the hydraulic actuators. All actuator forces were measured individually. The sixth actuator (center actuator 3b) was slaved to follow its neighboring center actuator 3a in force and displacement and was controlled by an internal pressure sensor. All other actuators used internal load cells. The diagonal actuators were controlled using the vertical LVDTs as mentioned above. The diagonal actuators adjusted their forces in compression and tension according to the displacement feedback obtained from the associated vertical LDVTs. Vertical displacements were controlled to be zero as shown in Chapter 5. The average horizontal displacement used in all load displacement relationships was obtained by calculating the average of actuator 1, 3 and 5. The individual actuator forces can be resolved into cumulative horizontal and vertical forces on the wall as well as applied moments about the wall centroid.

The movement of the abutment wall was performed in two stages for both tests. Stage one signifies a pretesting without soil backfill up to a displacement level of 10 inches (25 cm) in the T8.0-1 test and 2.4 inches (6 cm) in the T8.0-2 test. The purpose of this test was to measure the frictional resistance at the base of the wall from the natural underlying soil (T8.0-1) or from interaction between the wall concrete and underlying steel plate as in test T8.0-2. During the “no-backfill” test for T8.0-2, the load was cycled with displacements in the backfill direction only (no displacements back towards the reaction wall). During this phase the vertical uplift of the backwall was not restrained but was anticipated to be minimal given that the wall was not pushing into any backfill material.

After backfilling and compacting, the wall was pushed against the backfill soil up to 10 inches (25 cm). Forces were applied cyclically, but positive reactions were maintained against the wall so as to always maintain positive contact stresses between backfill and wall (i.e., no gapping).

All data have been recorded with a National Instrument data acquisition system.



Figure 3.6 Photograph of actuator configuration (Elevation view from North)

3.4 Backwall and Reaction Block Structural Repairs

During the T8.0-2a experiment, not all actuators behaved as expected. The intent of the six-actuator configuration was to use the center pistons 3L and 3R to provide the bulk of the lateral force to drive the wall into the backfill. Unfortunately, this was not the case. While the actuators were in contact with the wall throughout the experiment, they did not have a significant contribution until the wall had displaced approximately 0.75 inch (1.9 cm) into the backfill. Instead, the horizontal pistons at the top of the wall and the diagonal pistons bore the majority of the loading in the early stages of the experiment.

As this was not the anticipated loading behavior and the abutment wall was not designed to accommodate the associated moments, significant cracking occurred across the wall approximately 3 ft (1.0 m) from the base. Furthermore, the diagonal actuators were generating much larger forces than expected, eventually leading to failure in the reaction block at the diagonal actuator connections. Damage to the abutment wall and the reaction block is presented in Figure 3.7 and Figure 3.8, respectively.



Figure 3.7 Abutment Wall Cracks Between Actuators 2 and 3L



Figure 3.8 Reaction Block Blowout at Actuator 4

Both the wall and reaction block were repaired for subsequent tests T8.0-2b and T8.0-2c. The repairs were designed for the maximum load the diagonal actuators could produce. That way, even if the performance of the actuator group was not as expected, our connections and members would be able to withstand the actuator demands.

We assumed that the reinforcement steel passing through the cracked portion of the wall had ruptured and would be unable to transfer moments. Accordingly, we added W14X120 steel beams to the cracked face of the wall, effectively acting as cantilevers beyond the crack in the wall. The beams transfer the vertical component of the wall to rows of post-installed Hilti

anchors above the crack. Post-installed anchor calculations generally followed ACI 318-08 Appendix D and Hilti PROFIS Anchor Design software. Figure 3.9 shows the wide flange beams prior to actuator installation, and Figure 3.10 highlights the diagonal actuator-steel beam connection.



Figure 3.9 W14X120 Sections to Strengthen Damaged Backwall



Figure 3.10 Diagonal Actuator Attached to W14X120 Steel Sections

The reaction block damage was associated with unexpectedly large forces in the diagonally oriented actuators. The resulting moments generated by the eccentricity of the actuator connectors to the reaction block caused pullout failure of the connection anchors. The reaction block repair design sought to relocate the reaction load path to avoid a similar failure mechanism from occurring in future tests; connections and members were also designed to withstand maximum actuator loads. To resist the vertical component of the diagonal force generated by the diagonal actuators, a steel plate assembly as tall as the reaction block was designed as shown in Figure 3.11 to transfer shear away from the top edge and into Hilti post-installed anchors distributed across the reaction block face. The actuator-plate connection was designed to resist moments caused by the actuator pin eccentricity relative to the plane of the wall by reinforcing the plate with steel angle assemblies adjacent to the actuator connection. The damaged concrete edge was removed, the remaining corner was sandblasted, and fresh concrete was placed to repair the block (Figure 3.12).



Figure 3.11 Steel Plate and Angle Assembly to Strengthen Reaction Block



Figure 3.12 Repaired Edge of Concrete Reaction Block

4. Test Specimen

4.1. Concrete Properties

The dimensions and geometry of the test specimen were described in Section 3.1. The wall was constructed from reinforced concrete. The concrete was normal weight concrete with a specified unit weight of 145 pcf (22.8 kN/m^3). The weight of the wall specimen is 55,450 lbs (246.7 kN). Concrete cylinders taken during pouring were tested following the field testing. The stress-strain results are shown in Figure 4.1, and revealed an average strength of 5.76 ksi (39.7 MPa). Reinforcement steel with nominal yield capacity of $f_y = 60 \text{ ksi}$ (413 MPa) was used. Figure 4.2 and Figure 4.3 are photographs of the wall specimen showing the steel reinforcement layout and the curing concrete after pouring with forms in place.

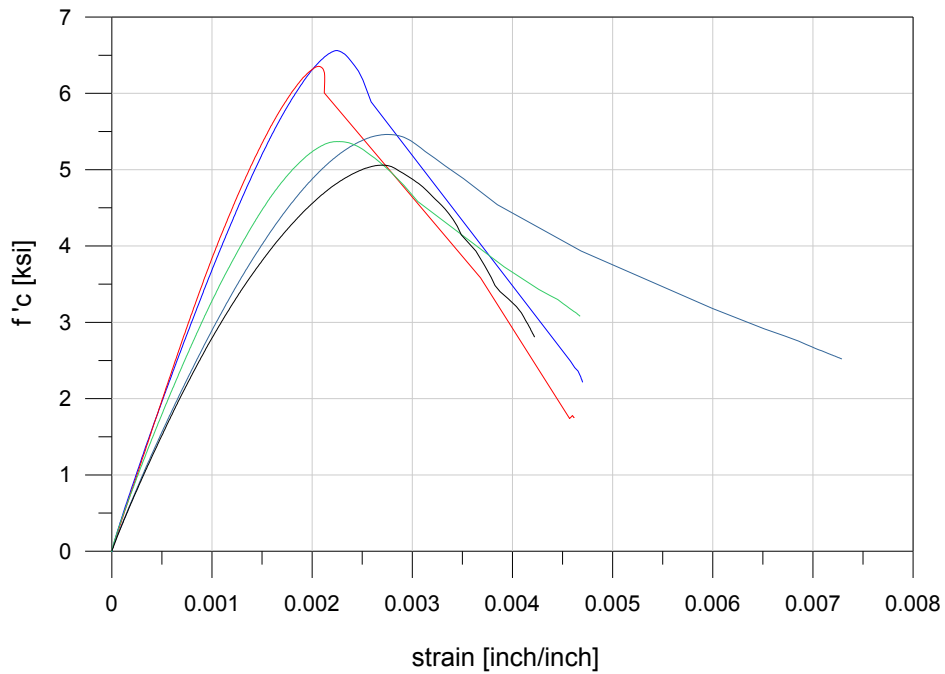


Figure 4.1 Concrete Compressive Strengths of 5 Test Cylinders



Figure 4.2 Abutment Wall Reinforcement Cage



Figure 4.3 Formwork and Concrete Curing

4.2. Backfill Soil

The abutment wall backfill for tests T8.0-1 and T8.0-2 was composed of a sandy material referred to in the construction industry as sand-equivalent 30 (SE-30). The height of the fill relative to the wall base varied slightly, but as shown in Figure 3.2 was nominally 8.0 ft (2.4 m) tall relative to the base of wall throughout the extent of the backfill. Backfill material was placed in 12 inch (30.5 cm) lifts in T8.0-1 and 8 inch (20 cm) lifts in T8.0-2. The SE-30 material was delivered in stages. The lower lifts of T8.0-1 consisted of material previously used in the T5.5 experiment, and the upper lifts consisted of newly delivered material. Similarly, lower lifts for the T8.0-2 specimen were composed of reused material from the T8.0-1 test. Soil bulk samples were taken at different stages of fill placement for both specimens. One bulk sample was taken from backfilling of T8.0-1 consisting of imported material (Sample T8.0-1 S1). Samples T8.0-2 S1, S2, and S3 represent the reused material from the T8.0-2 experiment; S4 through S6 represent the soil used in later lifts.

The lifts were compacted using a vibratory drum roller for T8.0-1 (Figure 4.4a) and vibratory plate for T8.0-2. The vibratory plate is a rectangular hydraulic vibrator attached to a backhoe, as shown in Figure 4.5b. The vibrator would move to a position in the field, bear down on the soil and pulsate, lift up after a certain level of settlement had been achieved, and then move on to the next position (usually overlapping) to repeat the same process. In more sensitive areas too risky to place the vibrator, such as near wingwalls and the abutment wall, a manual “whacker” was used for compaction.



Figure 4.4a Vibratory Drum Roller Compacting a Lift for T8.0-1



Figure 4.5b Hydraulic Vibrator and Manual “Whacker” Compacting a Lift (T8.0-2)

4.2.1 Gradation Tests

Gradation tests were performed on each bucket sample according to ASTM D422. Figure 4.6 shows the gradation curves for T8.0-1 and T8.0-2. Figure 4.6 illustrates that all the samples from both specimens were well-graded sands. T8.0-1 had a fines content ranging between 4.5% and 6%, whereas samples from T8.0-2 were slightly finer, between 5% and 7%. However, it also reveals slightly different particle size distribution in T8.0-2 S4 and T8.0-2 S5 when compared to the other T8.0-2 samples. Samples T8.0-2 S1 through S3 and S6 are very similar, being characterized by an effective grain size (D_{10}) of about 0.006 inch (0.15 mm) and a coefficient of uniformity (C_U) of 4.67. Samples T8.0-2 S4 and S5 are slightly finer and have an effective grain size of about 0.004 inch (0.11 mm) and a coefficient of uniformity of 4.54. Overall the sand materials have quite similar gradation characteristics. All specimens are classified in the Unified Soil Classification system as SP (glean, gravelly sand) and Group A-3 (fine sand) in the AASHTO soil classification system.

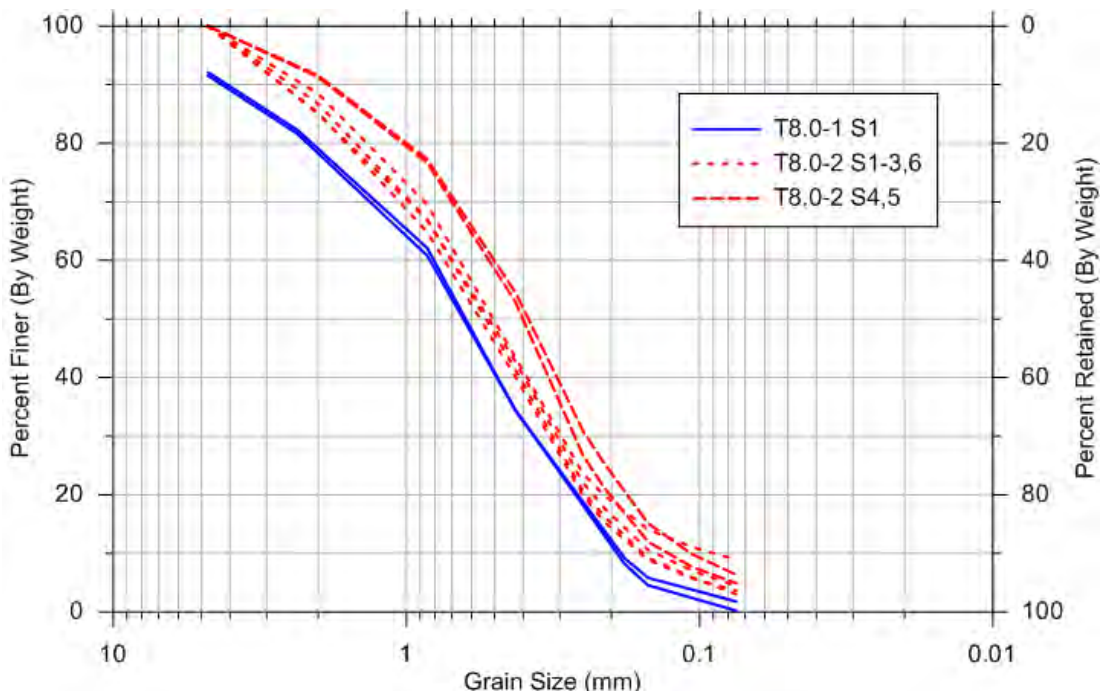


Figure 4.6 Grain size distribution of bucket samples from T8.0-1 and T8.0-2

4.2.2 Compaction and Relative Density

Modified Proctor tests (ASTM D1557) were performed in the laboratory to develop compaction curves for a sample from T8.0-1 and four samples from T8.0-2, with the results shown in Figure 4.7. We investigated how grain size might impact Modified Proctor results. Maximum dry densities increase slightly with mean grain size, D_{50} , as illustrated in Figure 4.8, but there are no significant differences between the compaction curves for the soils used in T8.0-1 and T8.0-2.

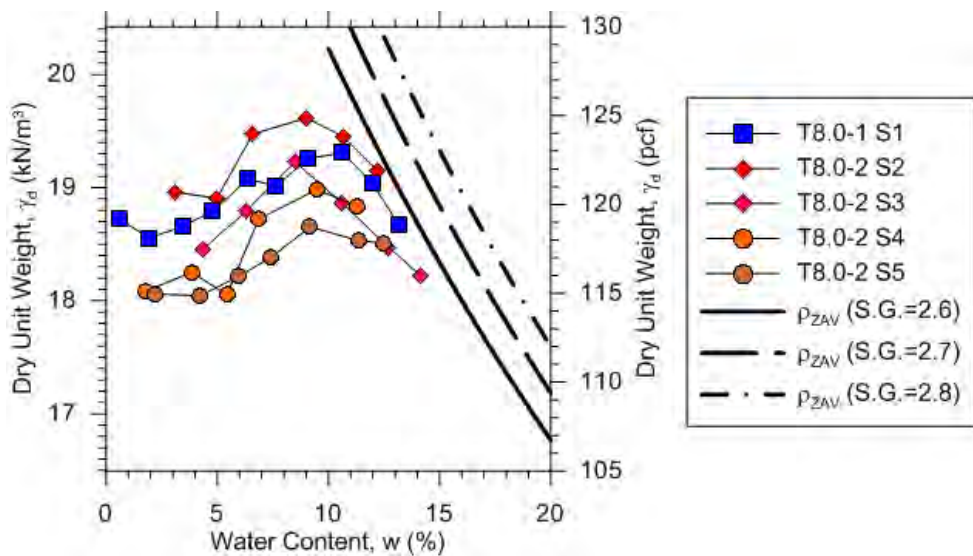


Figure 4.7 Compaction Curves for Various Samples from T8.0-1 and T8.0-2

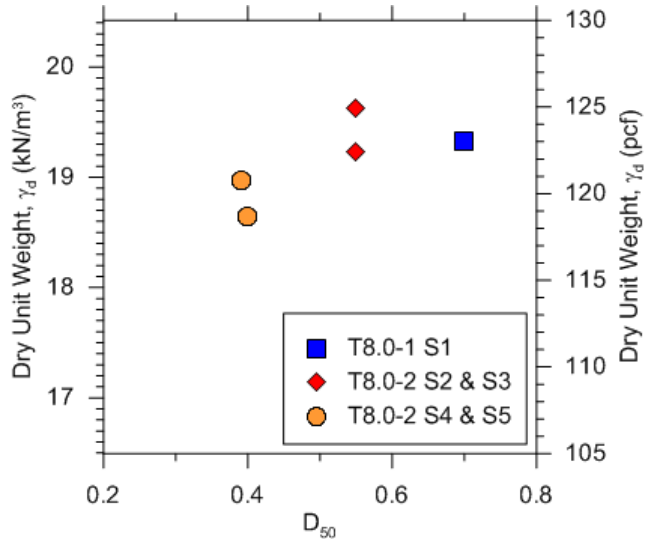


Figure 4.8 Observed Correlation between Maximum Dry Unit Weight and Gradation Parameter D_{50}

In between lifts, sand cone tests were performed to measure density and water content per ASTM 1556. The upper 2 inch (5 cm) of the lift was scraped off to remove loose material and ensure a more accurate representation of the level of compaction. Figure 4.9 illustrates a test in progress, and Figure 4.10 and Figure 4.11 show test locations for T8.0-1 and T8.0-2, respectively. As shown in **Error! Reference source not found.** and **Error! Reference source not found.** and Figure 4.12, the results indicate relative compaction levels per the modified Proctor standard between 93% and 106.8% with a mean of 98%, with a standard deviation of 5.8% for T8.0-1. For T8.0-2, compaction levels ranged between 93% and 114.8%, with a mean of 98.6% and a standard deviation of 6.0%. As-compacted water contents are generally at or near optimum. Relative compactations were computed using a maximum dry density of 120.5 pcf (18.85 kN/m^3).



Figure 4.9 Sand Cone Testing between Lifts

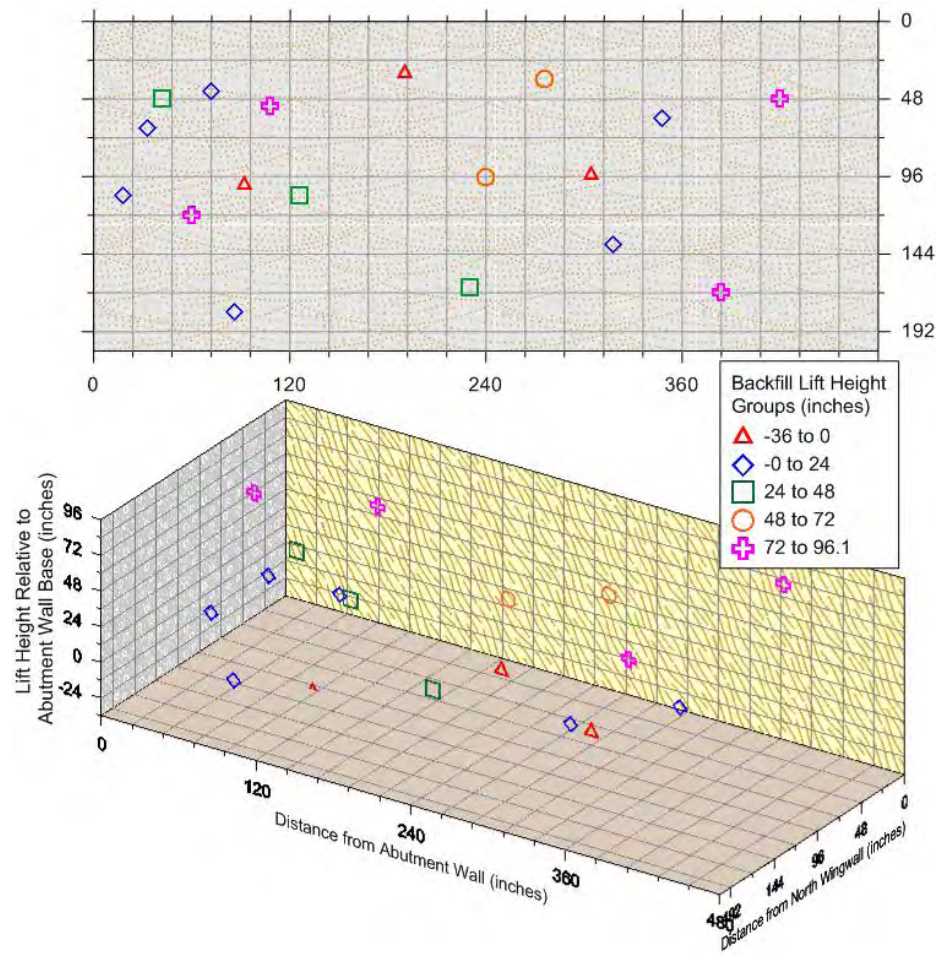


Figure 4.10 Sand Cone Test Locations during Compaction for T8.0-1

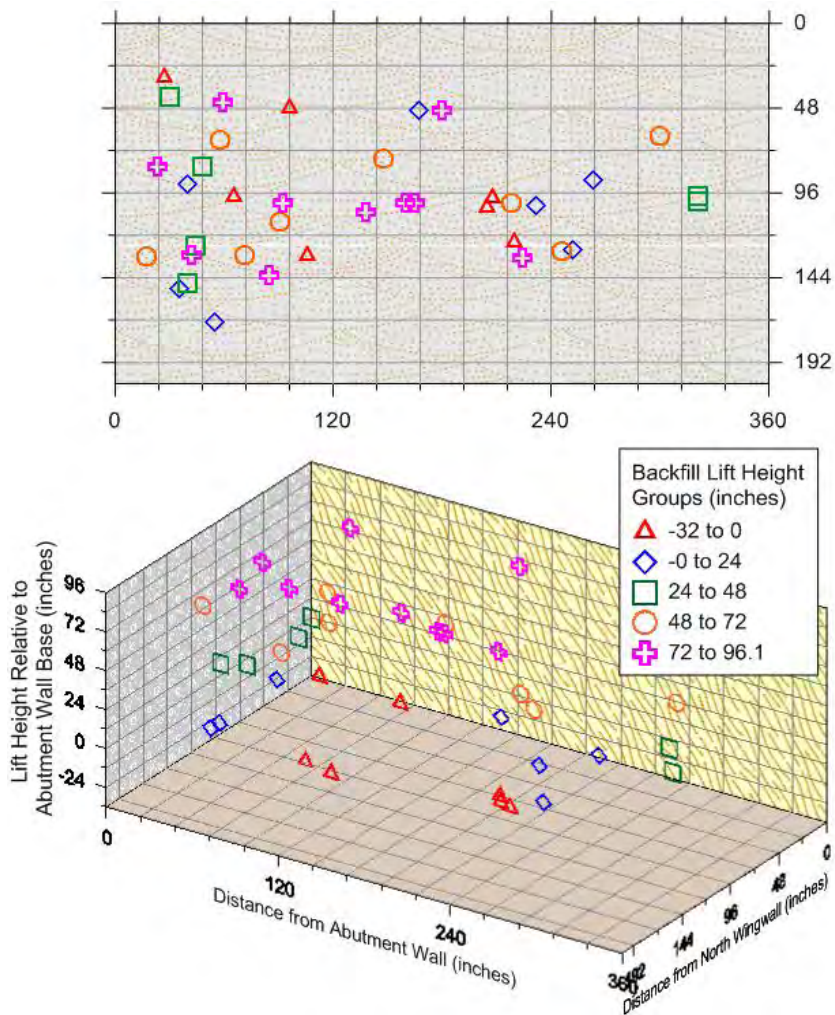


Figure 4.11 Sand Cone Test Locations during Compaction for T8.0-2

Table 4. 1 Sand Cone Test Results for T8.0-1

Sand Cone Test #	Wet Density (kN/m ³)	Moisture Content w (%)	Dry Density (kN/m ³)	R. C. (%)	Sand Cone Test #	Wet Density (kN/m ³)	Moisture Content w (%)	Dry Density (kN/m ³)	R. C. (%)
1	20.3	6.41	19.0	100.6	10	20.0	5.88	18.9	99.6
2	20.9	6.06	19.7	104.1	11	19.7	9.28	18.0	95.1
3	20.9	7.76	19.4	102.2	12	19.8	7.41	18.4	97.2
4	20.8	10.53	18.8	99.2	13	20.4	13.10	18.1	95.5
5	19.8	8.74	18.2	96.3	14	19.9	6.52	18.6	98.5
6	19.5	10.87	17.6	93.1	15	18.7	3.16	18.1	95.6
7	20.2	9.86	18.4	97.1	16	20.2	8.42	18.6	98.4
8	21.0	6.25	19.8	104.6	17	19.0	6.90	17.8	93.9
9	19.6	6.15	18.5	97.6	18	21.8	8.05	20.2	106.8

Table 4. 2 Sand Cone Test Results for T8.0-2

Sand Cone Test #	Wet Density (kN/m3)	Moisture Content w (%)	Dry Density (kN/m3)	R. C. (%)	Sand Cone Test #	Wet Density (kN/m3)	Moisture Content w (%)	Dry Density (kN/m3)	R. C. (%)
1	19.3	4.72	18.5	97.5	20	19.3	10.00	17.5	92.6
2	19.3	6.00	18.2	96.2	21	20.2	6.54	19.0	100.4
3	17.8	3.27	17.2	90.8	22	20.5	8.55	18.9	99.7
4	19.4	4.32	18.6	98.2	23	17.7	9.43	16.2	85.5
5	19.8	5.49	18.8	99.4	24	22.3	8.89	20.5	108.1
6	19.9	10.00	18.1	95.5	25	19.7	8.55	18.2	96.0
7	20.6	8.00	19.1	100.8	26	19.3	9.65	17.6	92.9
8	20.1	9.15	18.4	97.4	27	23.4	7.69	21.7	114.8
9	21.0	7.30	19.6	103.6	28	19.7	10.16	17.9	94.5
10	20.0	8.28	18.5	97.7	29	22.6	8.33	20.9	110.3
11	19.5	9.66	17.8	94.0	30	22.1	9.17	20.2	106.8
12	21.7	10.15	19.7	104.2	31	20.8	9.26	19.1	100.7
13	19.5	7.60	18.2	95.9	32	17.7	9.09	16.2	85.5
14	21.1	11.32	18.9	100.1	33	20.9	11.63	18.7	99.0
15	18.5	10.05	16.8	88.9	34	19.5	10.00	17.8	93.8
16	20.6	10.68	18.6	98.4	35	19.7	7.96	18.2	96.4
17	19.7	9.65	17.9	94.8	36	20.8	5.83	19.7	104.0
18	21.2	12.00	19.0	100.2	37	20.5	12.84	18.1	95.9
19	19.3	8.52	17.8	94.2	38	19.7	5.79	18.6	98.4

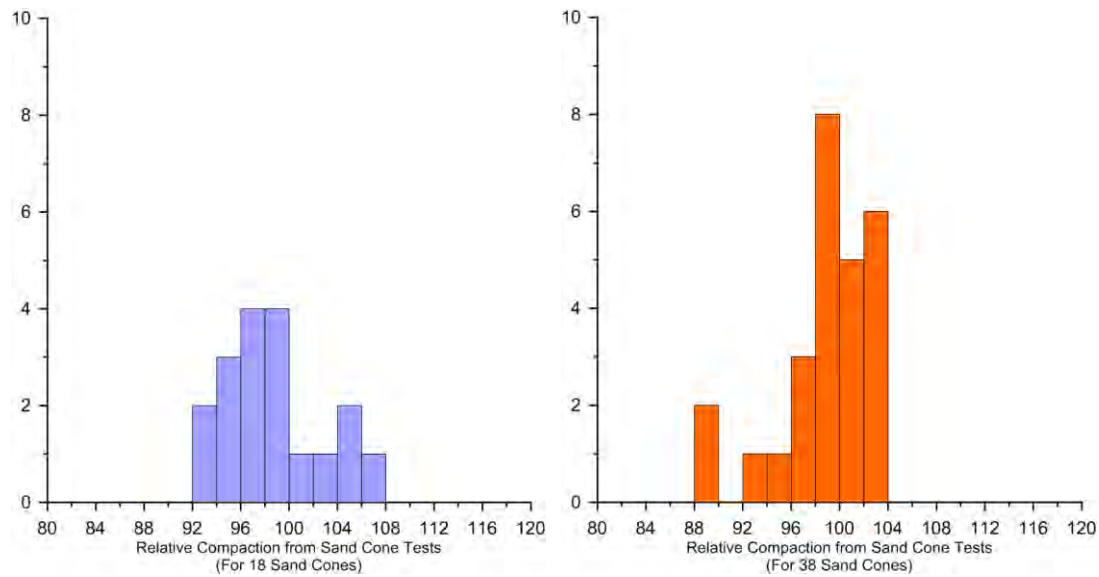


Figure 4.12 Sand Cone R.C. Histograms for T8.0-1 (left) and T8.0-2 (right)

Maximum and minimum dry density experiments (ASTM D4253 and ASTM D4254, respectively) were performed on the bulk samples, with the results shown in **Error! Reference source not found.** Maximum densities were obtained by filling a cylindrical mold with lifts of soil and vibrating the base of the mold for a set duration to densify the specimen. Minimum densities were obtained by placing soil samples into a graduated cylinder that was slowly inverted several times to achieve a loose condition.

Table 4. 3 Laboratory Results for Min. and Max. Dry Densities for Backfill Specimen

	T8.0-2 S1	T8.0-2 S2	T8.0-2 S3	T8.0-2 S4	T8.0-2 S5	T8.0-2 S6	Average
Minimum γ_d (kN/m ³) (pcf)	14.2 90.4	14.5 92.4	14.0 89.2	12.6 80.3	14.0 89.2	13.5 86.0	13.8 87.9
Maximum γ_d (kN/m ³) (pcf)	17.9 114.0	18.4 117.2	18.4 117.2	18.3 116.6	17.2 109.6	18.7 119.1	18.1 115.3

The average maximum dry density in **Error! Reference source not found.** of 115.3 pcf (18.1 kN/m³)(from ASTM D4253) is lower than the modified Proctor maximum density of 120.4 pcf(18.9 kN/m³) and the mean from the sand cone tests of 118.5 pcf (18.6 kN/m³). This occurs because the relative density standards for maximum density do not allow grain breakage during testing, whereas grain breakage is likely in the modified Proctor test and during field compaction. Therefore, in situ relative densities are difficult to evaluate in this case, but clearly they are high (near 1.0).

After the completion of tests T8.0-1 and T8.0-2, cone penetration tests (CPT) were performed using the nees@UCLA CPT rig (for T8.0-1, 8 soundings) in August 2009 and by Gregg Drilling in February 2011 (for T8.0-2, 4 soundings). Locations of CPTs for the two specimens are shown in Figure 4.13. The purpose of the CPTs was to evaluate uniformity in the backfill compaction and to measure penetration resistance that can be correlated to relative density. Each sounding penetrated through the backfill and into the native underlying clay. Of the eight soundings performed for T8.0-1, six were located in the full fill depth area. The remaining two soundings were located far enough from the wall to encounter the rising underlying layer of native soil. For T8.0-2, CPT-1, 2, and 4 were positioned within the full fill

depth area [fill depth of approximately 12 ft (3.7 m), CPT depth exceeds 15 ft (4.6 m)]. CPT-3 of T8.0-2 was performed further from the wall where the depth of fill was smaller.

Figure 4.14 shows normalized tip resistance (q_{cIN}) and soil behavior type index (I_c) for the CPT soundings performed for T8.0-1 and T8.0-2. These quantities are computed using standard procedures as described by Robertson and Wride (1998) and updated by Zhang et al. (2002). Tip resistances from T8.0-1 are notably lower than those for T8.0-2, suggesting lower overall levels of compaction. As expected, I_c values within the backfill are low (approximately 1.2-1.8), indicating sandy soil.

The T8.0-1 data are highly variable both from sounding-to-sounding but also with depth. The depth variations indicate systematic fluctuations over approximately 1.0-1.3 ft (0.3-0.4 m) depth intervals, which we interpret to indicate variable levels of compaction within lift thicknesses. The data do not show systematic changes with depth, which is expected due to the overburden normalization included in the computation of q_{cIN} . The fluctuations between soundings indicate a general level of scatter in the degree of compaction. Tip resistances from T8.0-2 are generally more uniform, both between soundings and with depth, indicating relatively uniform compaction within each lift and at different locations within the backfill.

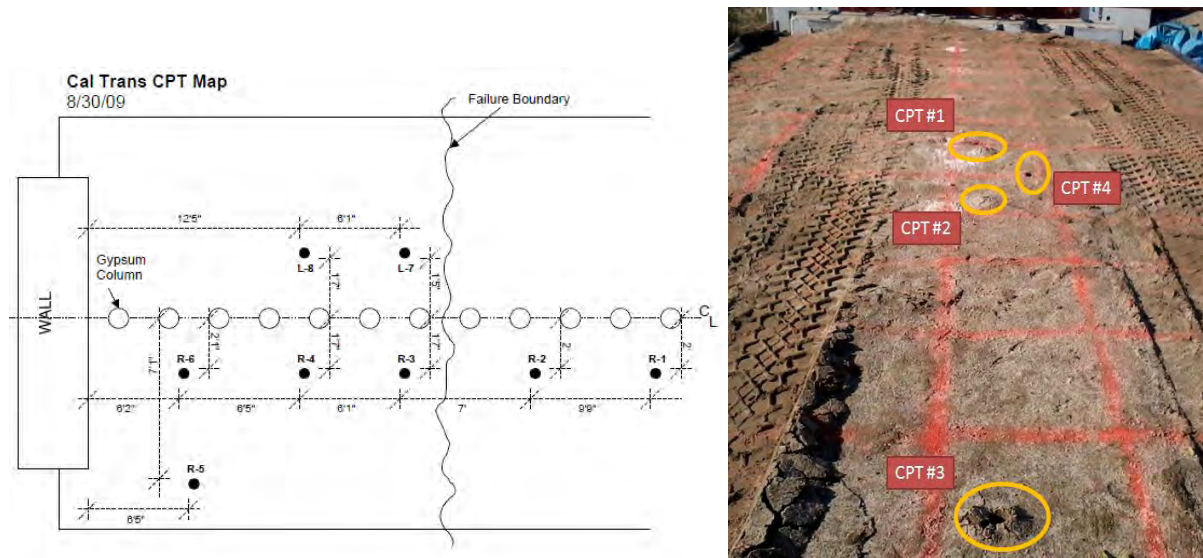


Figure 4.13 CPT Locations In Backfill for T8.0-1 (left) and T8.0-2 (right)

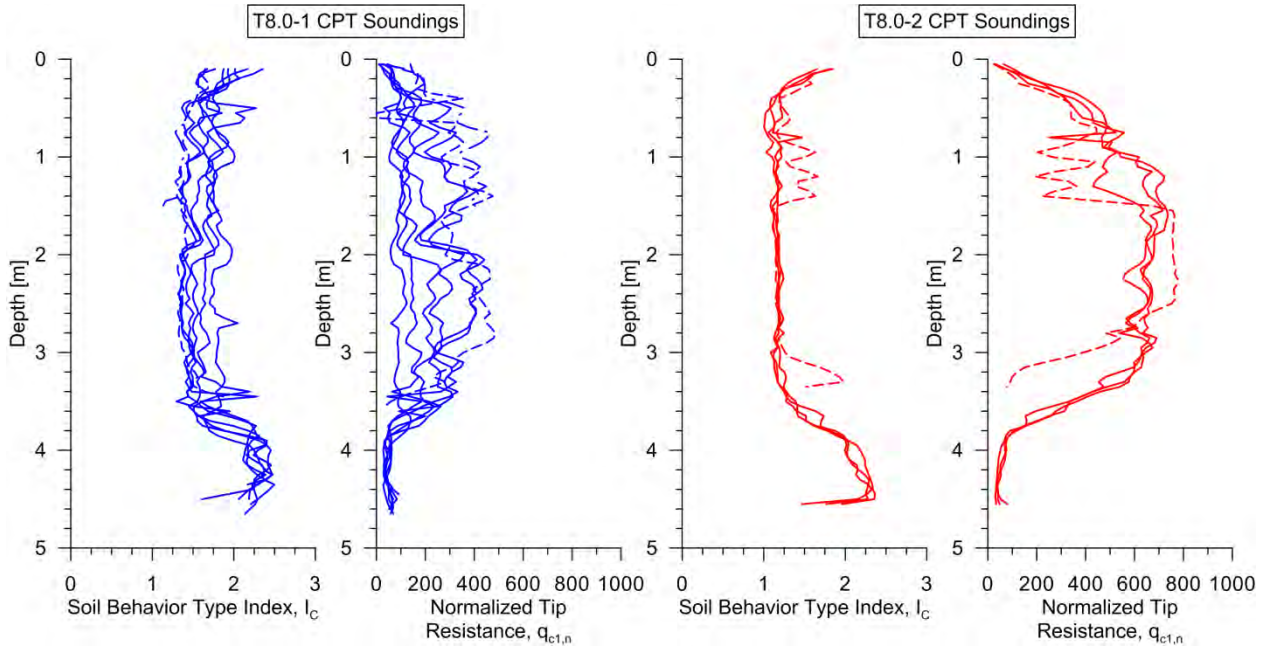


Figure 4.14 CPT data for T8.0-1 and T8.0-2

Over the depth range of 3.3ft – 9.8ft (1.0-3.0 m), average depth-normalized tip resistances for T8.0-1 and T8.0-2 are approximately $q_{c1N} \approx 250$ and 500, respectively. These results can be used to estimate relative density using the following empirical correlation (Idriss and Boulanger, 2008):

$$D_r = 0.465 \left(\frac{q_{c1N}}{C_{dq}} \right)^{0.264} - 1.063 \quad (4.1)$$

where C_{dq} is an empirical parameter reported to take on values ranging from 0.64 to 1.55 for various sands (Salgado et al., 1997; Idriss and Boulanger, 2008). This correlation produces estimates of D_r of about 1.0 for T8.0-2, even for the upper bound value of $C_{dq}=1.55$. Accordingly, these results corroborate the sand cone tests described above, indicating very high average relative densities in the compacted fill materials. For T8.0-1, the reduced $q_{c1N} \approx 250$ causes D_r estimates to be reduced relative to those for $q_{c1N} \approx 500$ by about 0.4 (per Eq 4.1). Good general estimates of D_r for T8.0-1 and T8.0-2 are 0.6 and 1.0, respectively. As noted previously, these D_r values are expected to be highly variable for T8.0-1 and relatively uniform for T8.0-2. Soft zones within the backfill for T8.0-1 have $q_{c1N} \approx 100-200$, with D_r values possibly in the range of 0.4-0.6.

4.2.3 Strength Tests

Triaxial compression tests (ASTM D2850) were performed on unsaturated specimens compacted from the six bulk samples. Each specimen was prepared to achieve a target water content of 9% and a relative compaction level of 96%, which is approximately representative of the compaction condition for T8.0-2. Table 4.3 records the range of water contents and relative compaction levels for the acceptable specimens, in addition to the confining pressures and peak deviator stresses recorded during the triaxial tests. For each specimen, the testing was performed by first placing the specimen under a prescribed cell pressure (σ_{cell} in Table 4.3), then shearing the soil to failure by increasing the vertical (deviator stress). Because the sand specimens are unsaturated, the shearing effectively occurs under drained conditions. The process was repeated for higher cell pressures and the soil tested to failure at each level. These protocols are different from those applied in T5.5 (described in Section 2.1) in which the same specimen is used for each confining pressure, which reduces dilatancy at the higher confinements. Stress-strain curves resulting from the testing of several specimens subjected to the above load sequence are shown in Figure 4.14.

Table 4. 4 Triaxial strength test results for SE30 sand

Sample Bucket #	Test Specimen #	Water Content (%)	Relative Compaction (%)	Confining Stress σ_{cell} (kPa)	Peak Deviator Stress $\Delta\sigma$ (kPa)	Strain (%) at Peak $\Delta\sigma$
1	1.0	8.85	96.2	68.95	282.99	7.32
2	1.1	9.24	96.0	68.95	268.9	1.98
	2.1	9.13	96.2	137.9	503.98	4.05
	3.1	8.96	96.6	275.8	870.27	5.91
3	1.1	9.15	98.6	68.95	315.22	1.93
	3.1	8.56	98.8	275.8	734.85	5.83
4	1.1	8.33	93.5	68.95	280.67	6.12
	2.1	9.12	93.6	137.9	453.81	6.48
	1.2	9.05	94.3	68.95	294.1	2.06
	2.2	9.05	92.1	137.9	427.33	6.04
5	1.0	8.53	95.8	68.95	217.96	6.18
	2.0	8.62	96.7	137.9	454.85	4.09
6	1.0	9.34	94.5	68.95	267.7	2.57
	4.0	8.69	93.5	275.8	815.78	6.77

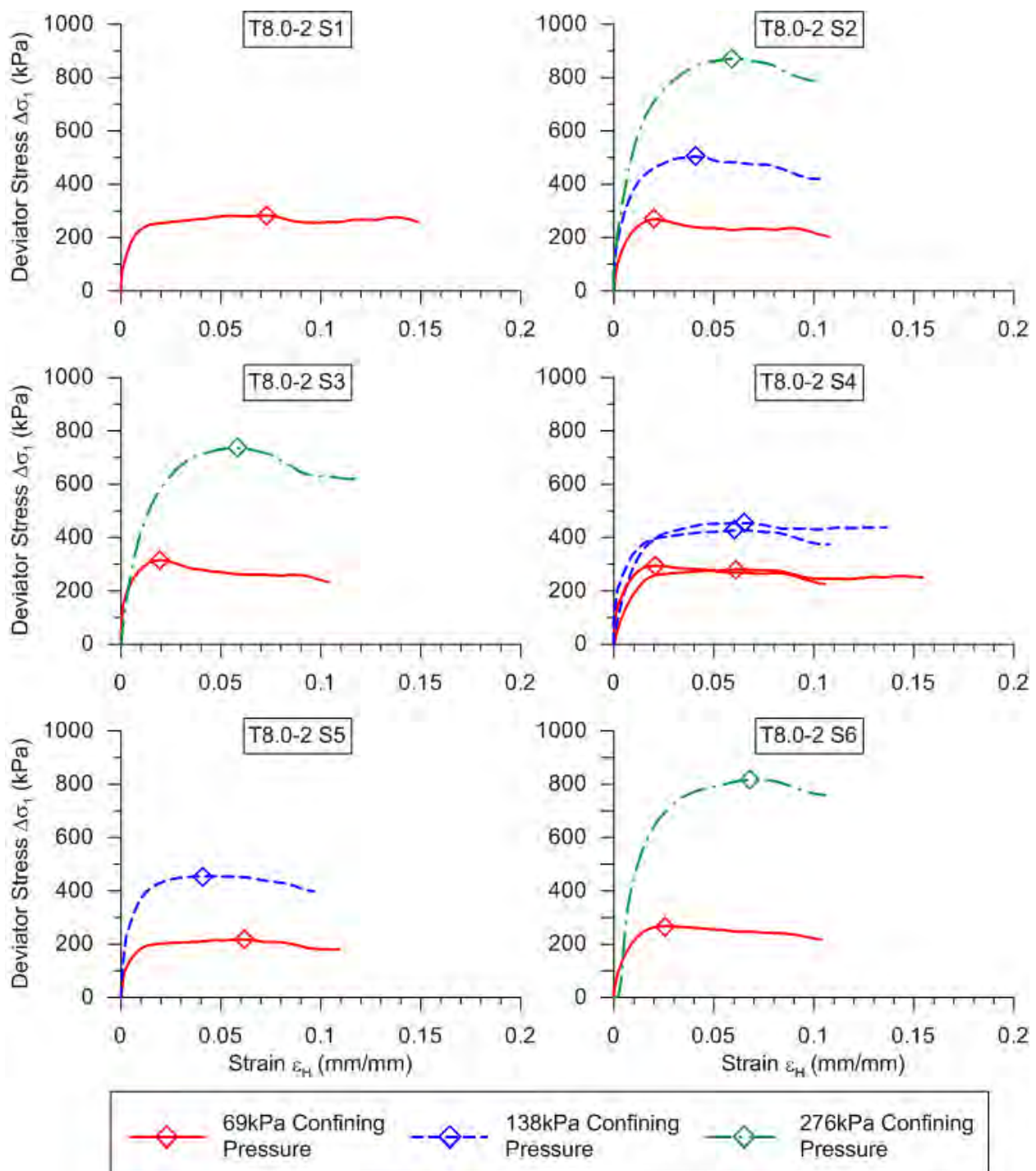


Figure 4.14: Stress-Strain plots for Different Triaxial Tests by Sample (T8.0-2)

Stress points for the peak deviator stresses obtained in the triaxial tests for both T8.0-1 and T8.0-2 were plotted in p - q space as shown in Figure 4.15. These points are used to construct the K_f line, whose equation is expressed as

$$q_f = a + p_f \tan\psi \quad (4.2)$$

A linear regression was performed on the data set to estimate parameters a (from the line intercept) and ψ (from the slope of the line) as 0.43 ksf (20.4 kPa) and 29.5° , respectively. The standard deviation of residuals (in the q direction) is 0.2 ksf (9.7 kPa), which translates to a \pm one standard deviation range for a of 0.22 – 0.63 ksf (10.7 to 30.1 kPa) when holding the slope of the fit line constant. Confidence intervals at the 95% level are also plotted in Figure 4.15. The variability of ψ was evaluated by constructing additional fit lines within the confidence intervals. A lower bound was found by determining the slope of the line that was tangent to the upper interval line at the q -axis and tangent to the lower interval line at the largest p value. Similarly, an upper bound estimate of ψ was calculated from the slope of the line tangent to the lower interval line at the q -axis and the upper interval line at the largest p value. Using this process, angle ψ varies between 28.2° and 30.8° .

Once ψ and a are established for the K_f line, strength parameters ϕ and c for the Mohr-Coulomb failure envelope can be computed as (e.g., Lambe and Whitman, 1969, p 141):

$$\sin\phi = \tan\psi \quad (4.3)$$

$$c = \frac{a}{\cos\phi} \quad (4.4)$$

The resulting envelopes yield a range of friction angle (ϕ) from 32.6° to 36.6° (mean of 34.5° degrees) and range of cohesion (c) from 280 psf and 760 psf (13.0 and 36.5 kPa), with a mean of 520 psf (24.8 kPa). Figure 4.15 illustrates the Mohr circles derived from test results corresponding to peak deviator stress. The Mohr-Coulomb failure envelope shown in Figure 4.16 is fit with the mean values for c and ϕ , and agrees well with the Mohr circles generated from the triaxial test results.

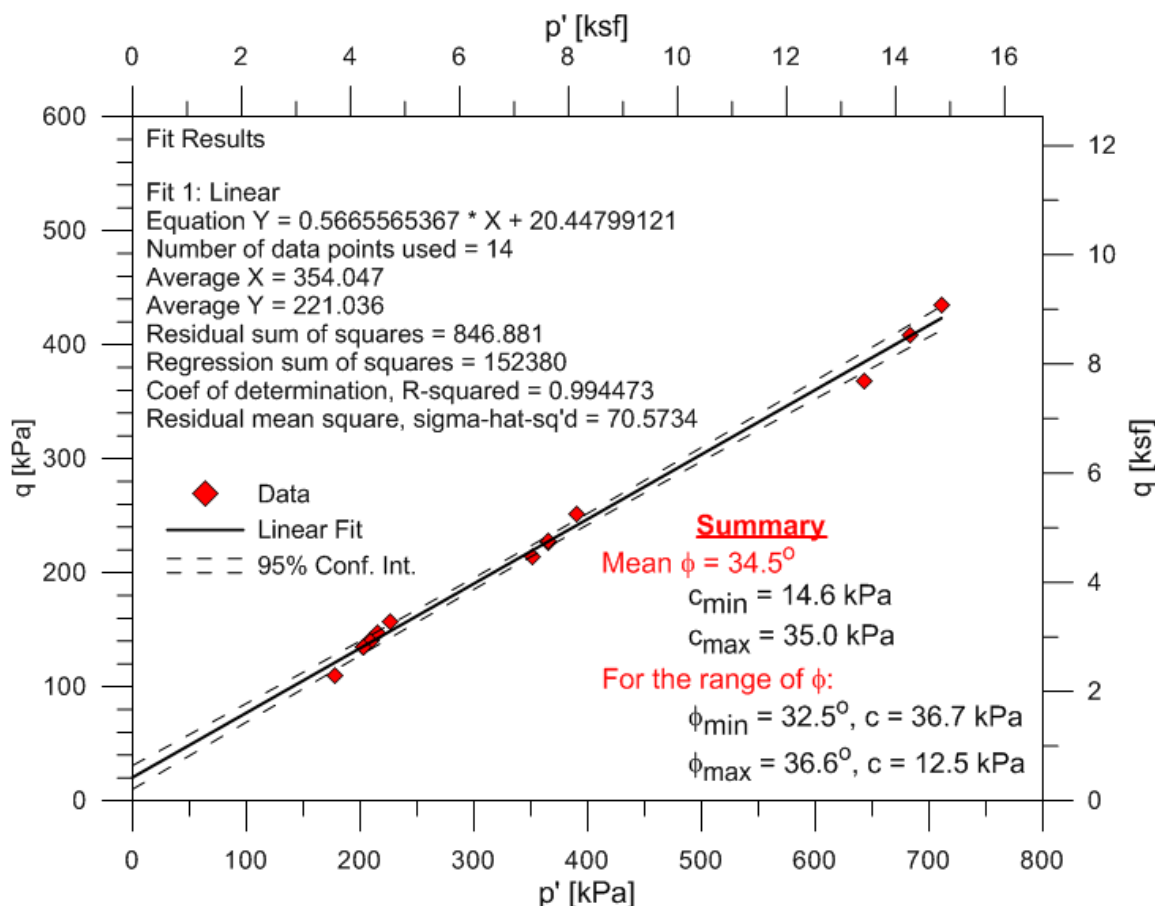


Figure 4.15 Stress points at failure for various triaxial tests with linear fit of the K_f line (T8.0-2). Corresponding parameters for the Mohr-Coulomb failure envelope are reported.

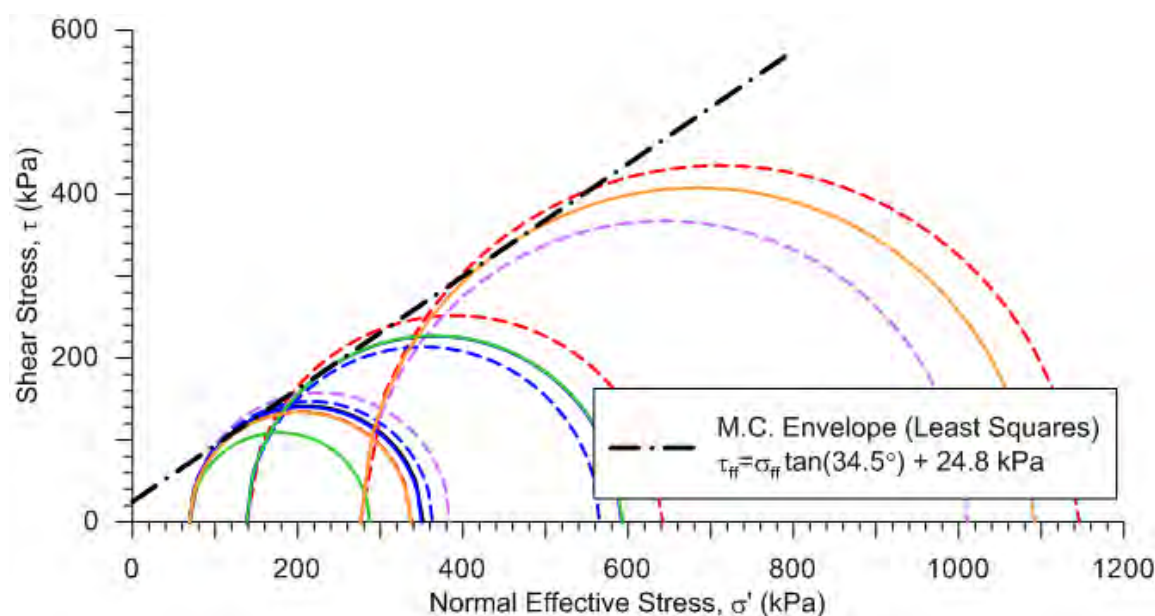


Figure 4.16: Mohr Circles and Mohr-Coulomb Envelope from Triaxial Results (T8.0-2)

5. Test Results

5.1. Load-Displacement Data

Table 1.1 presents the nomenclature used to refer to the various abutment backwall tests performed as part of this research. This section documents the test sequence and the data collected during tests T8.0-1 and T8.0-2 on 8.0ft (2.4 m) high backfills. Both test sequences were preceded by tests that involved displacing the wall, absent backfill, to establish the load-deflection relationship associated with base friction. Test 8.0-1a pushed the backwall until actuator capacity was reached; an additional actuator was installed and test 8.0-1b completed the experiment. Test 8.0-2a caused the concrete abutment wall and reaction block to be structurally compromised. Tests 8.0-2b and 8.0-2c resumed testing on the same backfill specimen once structural repairs were completed.

5.1.1 Baseline Friction Tests

The concrete backwall specimen for test T8.0-1 rested directly on native soil. The same condition was in place for T5.5 in 2006. Base friction tests involved application of several increments of horizontal wall displacement towards the backfill without allowing vertical displacement. Figure 5.1 and 5.2 show the load-deflection data collected for the baseline friction tests for T5.5 and T8.0-1 for the horizontal and vertical force components. The data are cropped at a lateral displacement level of 5 inches (12.7 cm); force measurements were nearly constant at higher displacements. The results for T8.0-1 indicate slightly higher horizontal forces than T5.5 and upward vertical forces that match the wall weight. Hence, it appears that the wall was suspended above the base for this test and that horizontal resistance was applied by a soil wedge below the leading corner.

Those conditions were not present for T5.5. Accordingly, we anticipate that the results for T5.5 more realistically represent the base friction for this boundary condition of the wall resting directly on native soil.

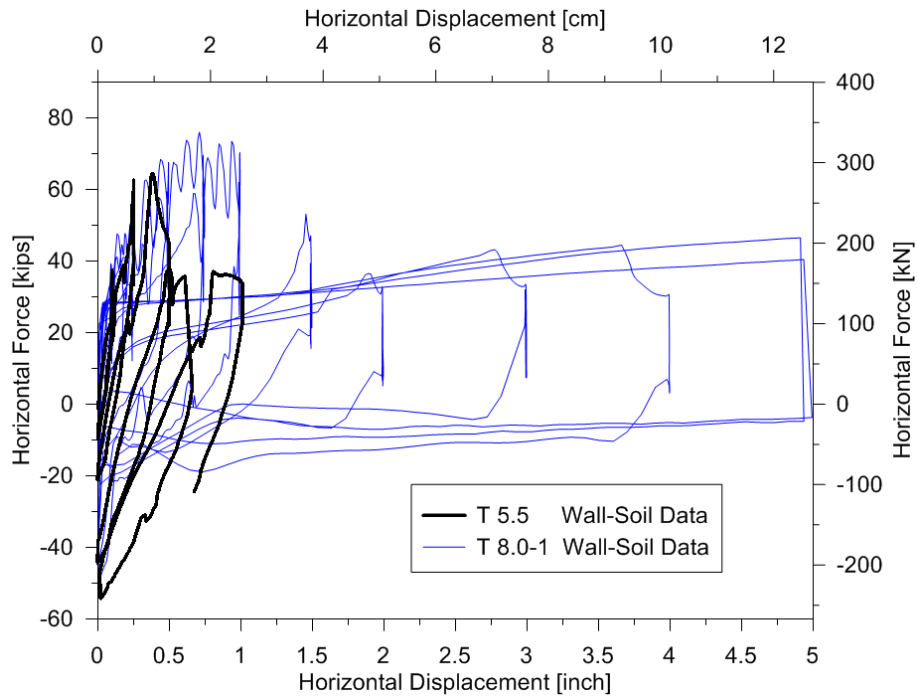


Figure 5. 1 Horizontal load - displacement relationship of baseline friction tests T5.5 & T8.0-1

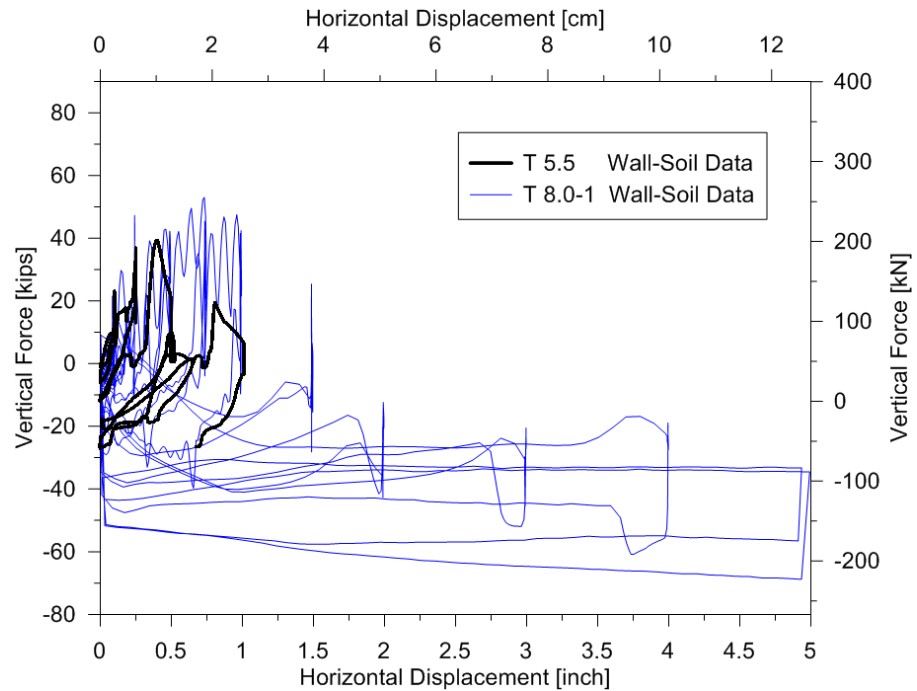


Figure 5. 2 Vertical load-displacement relationship of baseline friction tests T5.5 & T8.0-1

Test sequences T5.5 and T8.0-1 scraped away soil beneath the backwall with each push and pull cycle. In addition, rainy weather conditions during winter and spring of 2010 caused temporary flooding of the site and downward movement of the backwall into the softened soil. The resulting wall settlements presented difficulties with connecting the actuators to the abutment wall. To correct this problem and to minimize additional settlement, a steel baseplate was installed between the native soil and concrete wall prior to T8.0-2. To create a smooth contact surface, cementitious grout was placed prior to setting the wall on the plate.

Figure 5.3 presents the horizontal and vertical load-deflection data collected without backfill for T8.0-2. Several increments of testing were performed in the positive direction (towards the backfill), with the largest amplitude being 1.7 in (44 mm). Displacement limits were set in the control system for safety reasons; the sudden jumps in the graph indicate that those internal displacement limits were reached. The limits were extended and the test resumed after it was assured that the specimen and the surrounding soil were stable.

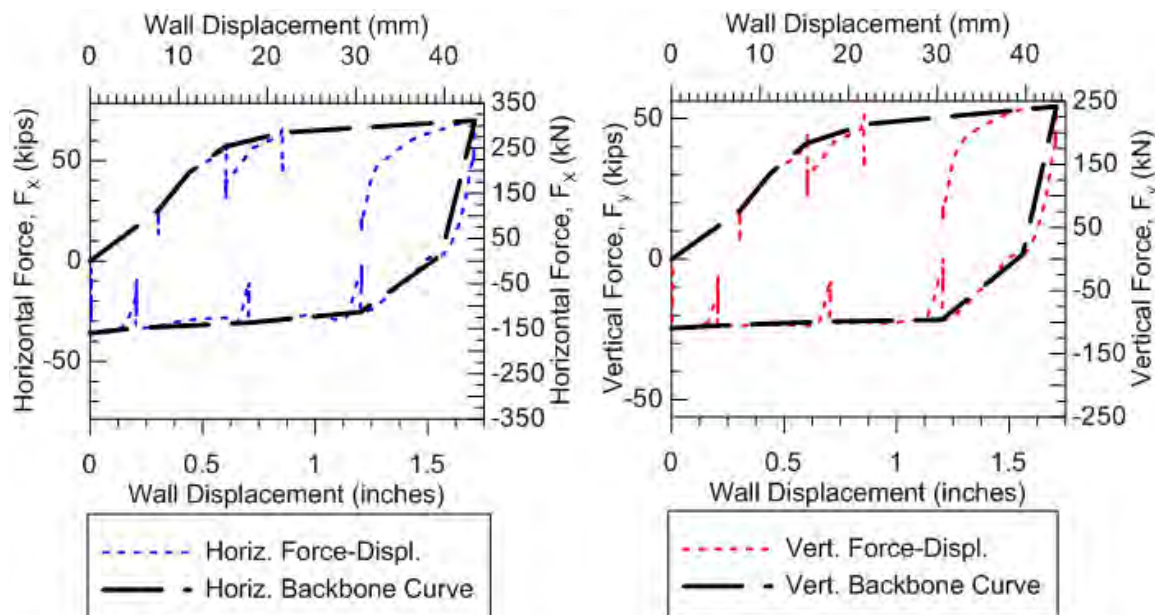


Figure 5.3 Horizontal and vertical load-displacement relationships for baseline friction test T8.0-2

The sliding behavior during both the baseline friction test and T8.0-2a was observed to occur both in the wall-grout-plate interface as well as the plate-soil interface.

As shown in Figure 5.4, a black line drawn onto the steel plate along the perimeter ground indicated limited displacement between the wall and plate; a small groove in the soil adjacent to the plate revealed movement between the plate and soil.

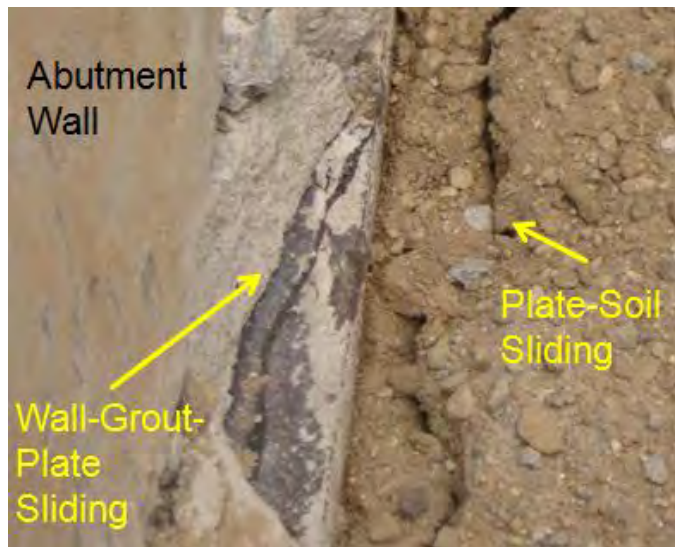


Figure 5.4 Observed sliding during baseline friction test

The maximum horizontal force component during the baseline friction test was approximately 70 kips (310 kN) at the largest displacement. The corresponding vertical force component during the push with no backfill was approximately 56 kips (250 kN). Compared to baseline friction test data from T5.5, these forces are relatively large but are in better agreement with the horizontal friction component of T8.0-1. This is may be due to the fact that the base plate has small rods that “anchor” into the native soil, increasing the expected base resistance. Based on the recommendations of Rabbat and Russel (1985), an average static friction coefficient between cast-in-place grout and rolled steel on a smooth interface is 0.57. By adding together the weight of the concrete block of 65 kips (290 kN) and the maximum vertical force component imparted by the actuators, 56 kips (250 kN), the resulting static frictional force that must be overcome is 69.4 kips (308 kN). This is remarkably close to the observed maximum baseline value for the horizontal force component (70 kips or 310 kN).

5.1.2 Data from T8.0-1

As shown in Table 1.1, test T8.0-1 occurred in two stages. Figure 5.5 shows the load displacement relationships of the measured horizontal and vertical force components for the first stage (T8.0-1a). This stage of testing was paused because the center actuator (Actuator 3) reached its capacity, as indicated in Figure 5.6. The specimen was unloaded, i.e. the wall was pulled back to release the pressure in the hydraulic equipment and left at-rest at a permanent lateral displacement of 1.35 inch (3.4 cm) with respect to the origin of the test. Therefore, starting point for test T8.0-1b in August 2009, with results shown in Figures 5.7 and 5.8, is a lateral offset of 1.35 inches (3.4 cm).

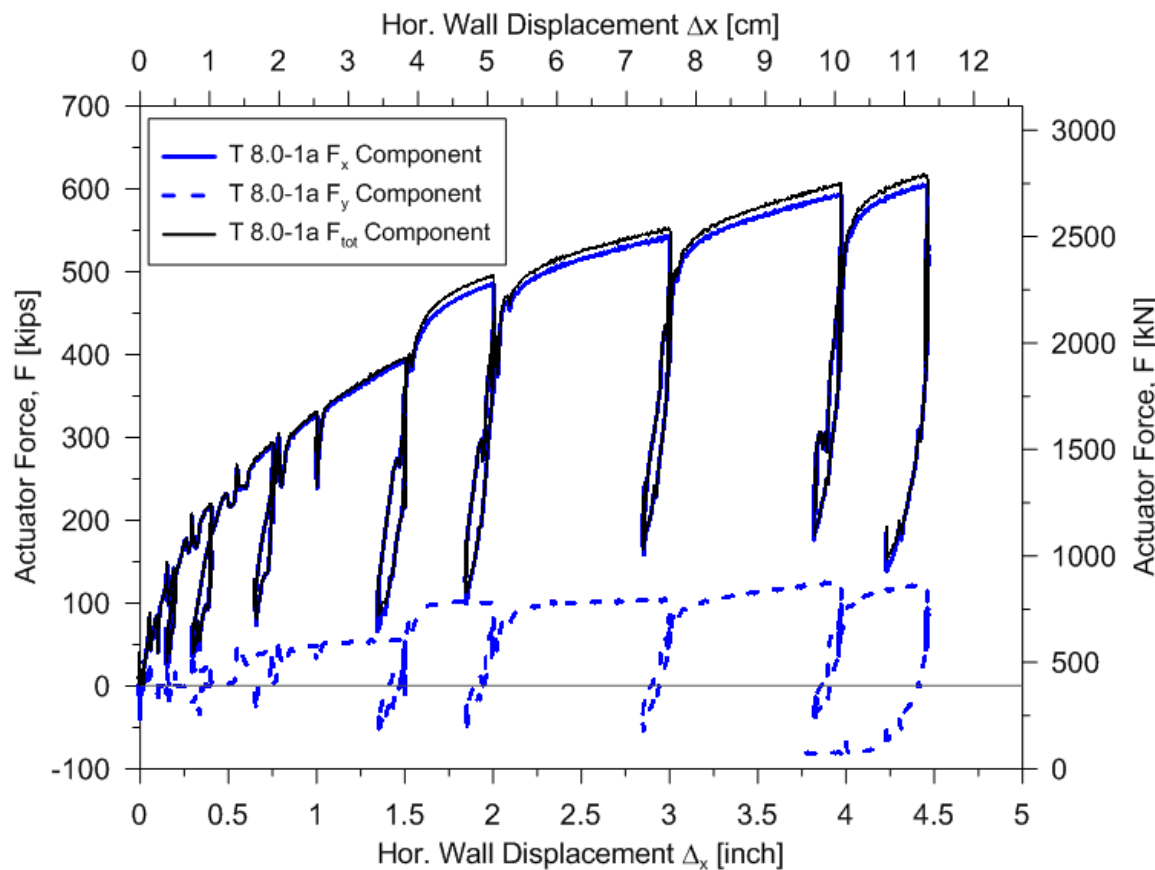


Figure 5.5 Horizontal, vertical and total load displacement relationship of T8.0-1a

Prior to commencing the second stage (T8.0-1b), an additional center actuator (H3R) was installed. As shown in Figure 5.7, testing in this stage reached maximum forces of 705 kips (3140 kN) and 250 kips (1110 kN) in the horizontal and vertical directions, respectively. Actuator forces for this stage are presented in Figure 5.8.

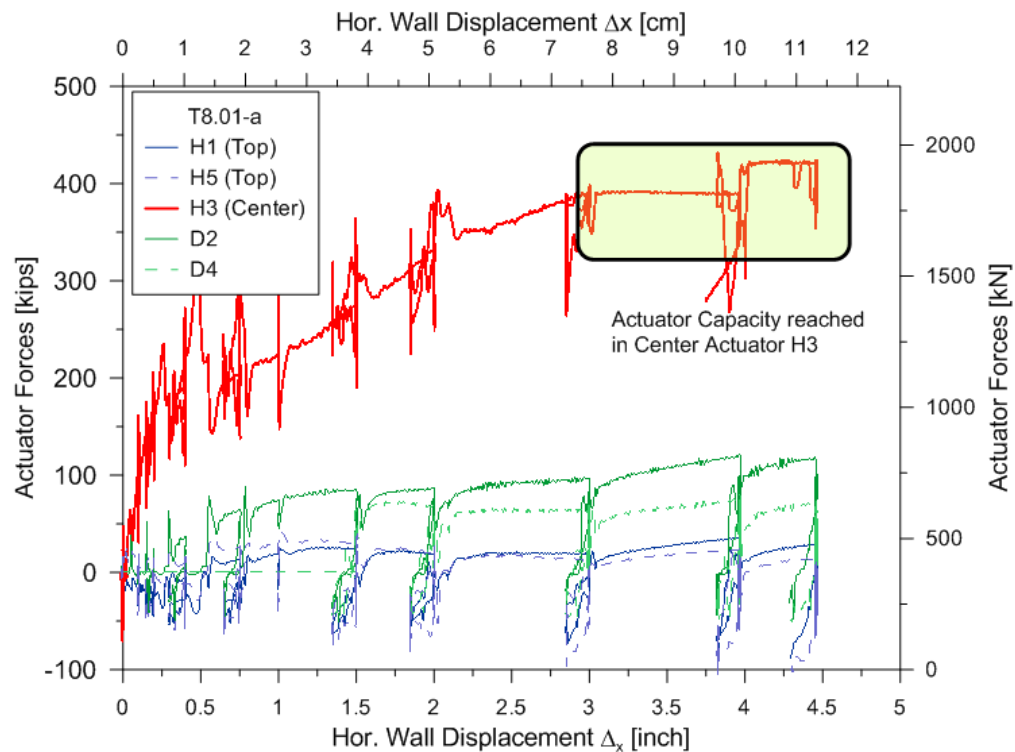


Figure 5.6 Individual, measured actuator forces during test T8.01a

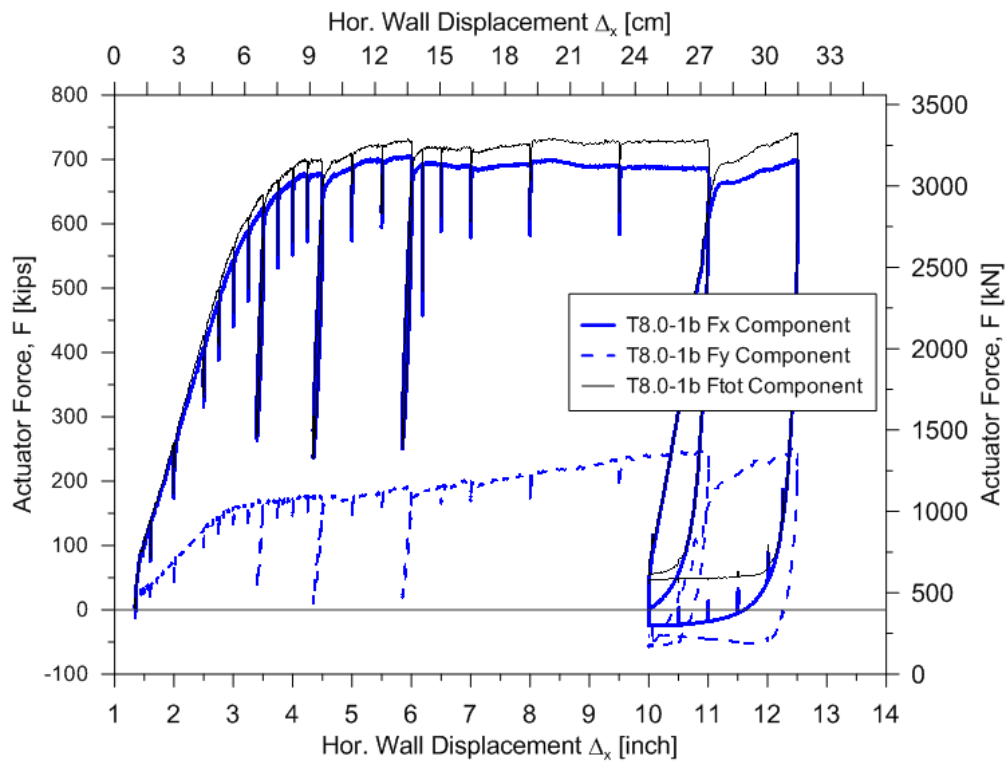


Figure 5.7 Horizontal, vertical and total load displacement relationship T8.0-1b

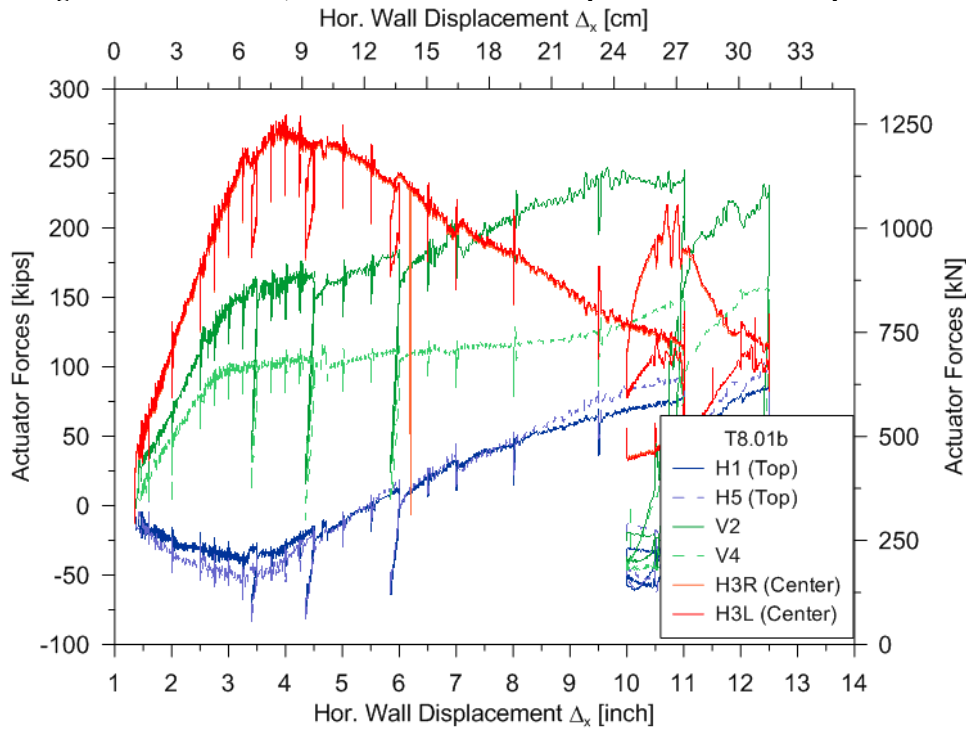


Figure 5.8 Individual actuator forces test T8.01b

5.1.3 Data from T8.0-2a

The force-displacement data for the combined actuator forces during T8.0-2a up to the point of structural damage is shown in Figure 5.9. The total force exerted by the hydraulic system reached approximately 1450 kips (6400 kN) before premature termination of the experiment at 1.6 inch (4 cm) of displacement. Figure 5.10 shows the individual actuators' respective force contributions. Actuators 3L and 3R delayed in contributing to the overall driving force until 0.75 in (1.9 cm) of displacement. Without the expected contributions from these actuators at the center of the wall, the driving force was instead provided by the remaining actuators. In particular, the diagonal actuators were strongly loaded, with the force in diagonal actuator V2 exceeding 400 kips (1780 kN) beyond approximately 1.2 inch (3 cm) of displacement, which is the load cell's upper bound. The lack of center support on the abutment wall produced significant flexural cracking in the abutment wall. The large force demands in the diagonal actuators also led to anchor failures in the reaction block.

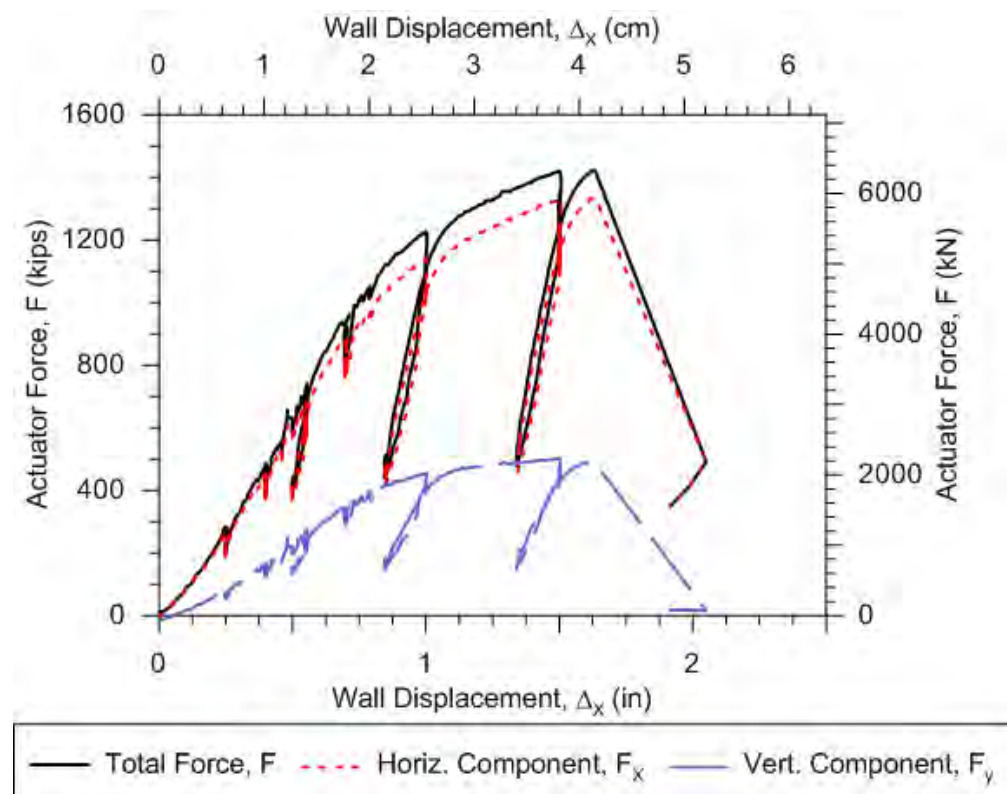


Figure 5.9 Horizontal, vertical and total load displacement relationship T8.0-2a

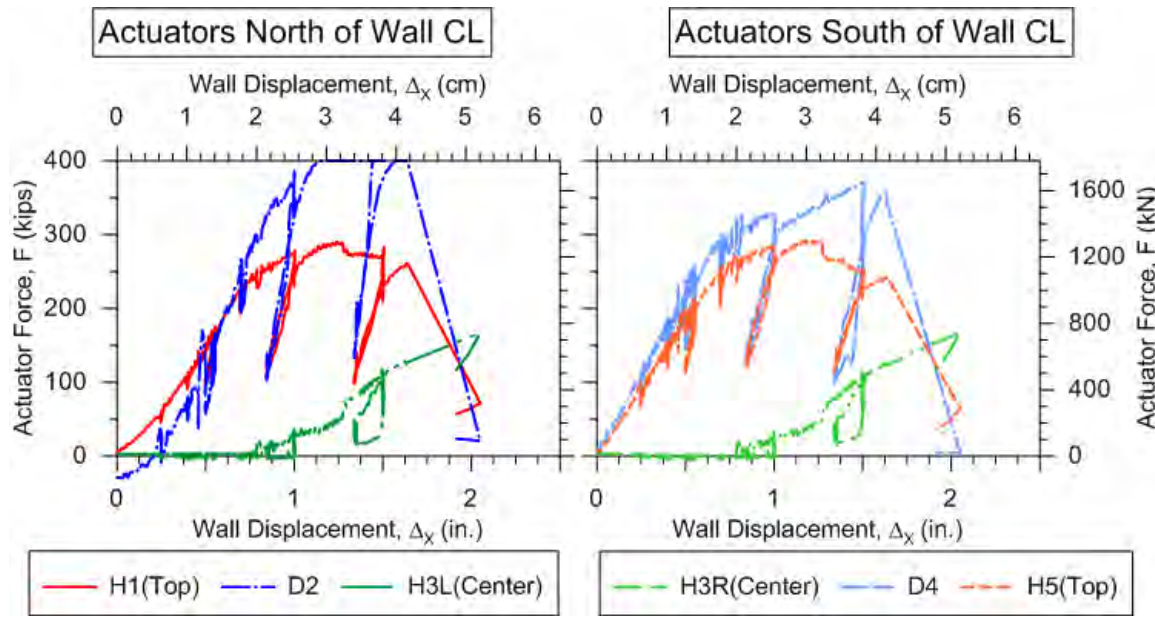


Figure 5.10 Individual actuator forces T8.02a

5.1.4 Data from T8.0-2b & T8.0-2c

Once structural repairs were completed and the control systems were reassembled, testing on the same backfill specimen from T8.0-2a resumed in December 2010. Testing performed on 8 December 2010 is referred to as T8.0-2b and testing on 13 December 2010 is referred to as T8.0-2c. These are not really separate tests but continuations of the same test. Following the sudden structural failures in July 2010, the concrete backwall specimen displaced at the interface with grouted steel base plate. During the December 2010 tests, base sliding occurred between the wall and plate as shown in Figure 5.11 and the steel plate did not appear to displace relative to the underlying soil.



Figure 5. 11 Visible striations on the steel base plate during T8.0-2b and T8.0-2c indicating movement along the wall-grout-plate interface

Figure 5.12 shows the combined actuators' force-displacement data. Total force and horizontal force in T8.0-2b and T8.0-2c exceed the levels of T8.0-2a. The total actuator force applied in T8.0-2b capped at about 1500 kips (6670 kN) at 5.75 in (14.6 cm) of displacement, corresponding to a horizontal load of 1440 kips (6420 kN) and vertical load of 345 kips (1530 kN). Test T8.0-2c produced a maximum total actuator force of 1750 kips (7780 kN) at 8.25 inch (21 cm), with the horizontal component at the total force peak being 1675 kips (7450 kN) and the corresponding vertical component being 525 kips (2330 kN). The initial stiffness for T8.0-2b is much lower than T8.0-2a or T8.0-2c, which we attribute to gap closure. We speculate that the backfill gradually pushed back the abutment wall over the course of the five month pause between T8.0-2a and T8.0-2b, creating gaps between the upper portion of the backfill and the wall. T8.0-2c exhibits a much higher stiffness upon initial loading.

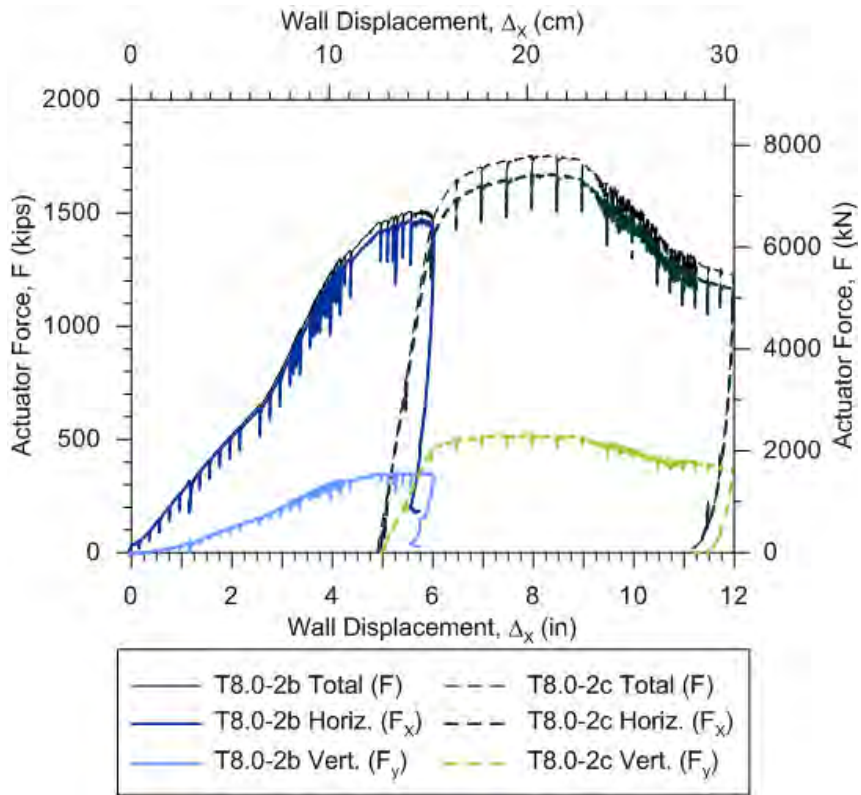


Figure 5.12 Tests T8.02b and T8.0-2c horizontal, vertical and total load displacement relationships

5.2. Metrics of Specimen Performance

We present seven metrics of specimen performance that are relevant to the design of backwalls and retaining structures in general. First, we describe the assembly of the various tests into composite force-displacement plots (T8.0-1a and T8.0-1b into T8.0-1; T8.0-2a, T8.0-2b, and T8.0-2c into T8.0-2). Next, we investigate the ultimate passive capacity of the backfill specimen once corrected for base friction effects. Third, we describe the shape of the load-deflection curves prior to the backfills' passive failures. Fourth, we evaluate the interface friction angle (δ_{iw}) mobilized at the abutment wall-backfill soil interface. Fifth, we review the unload-reload moduli at different displacement levels. Finally, we present the earth pressure distribution behind the backwall for various levels of lateral abutment displacement. We do not interpret the

causes of specimen-to-specimen differences in these performance metrics in this section. That discussion is deferred to Chapter 6.

5.2.1 Assembling Data into One Representative Plot

An assembly of measured data from parts *a* and *b* of T8.0-1 is presented in Figure 5.13. As mentioned previously, Test T8.0-1b had a displacement offset of 1.35 inch (3.4 cm) after unloading and pausing T8.0-1a. Test data for T8.0-1b is plotted with this shift in the horizontal wall displacement in Figure 5.13. The combined forced displacement relationship for this test is taken as the envelope of the responses shown in Figure 5.13.

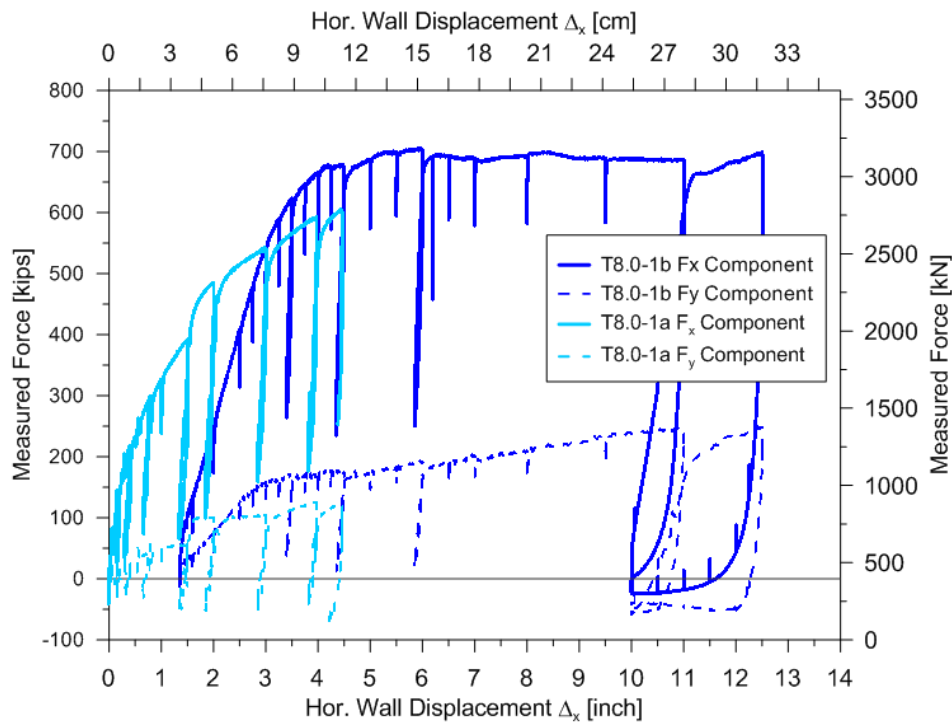


Figure 5.13 Combined horizontal and vertical load displacement relationships of test T8.01a&b

Piecing together the force-displacement curves of the three subtests of T8.0-2 required some engineering discretion. T8.0-2a contains essential initial loading data, and while not reaching maximum capacity, exhibits nonlinear behavior in the backbone curve. During T8.0-2b, the maximum capacity initially appeared to have been reached,

but long test duration compromised actuator efficiency, requiring the test to be temporarily halted. Five days later, T8.0-2c produced higher resistance than the prior tests, not reaching peak resistance until wall displacement was several centimeters beyond those from T8.0-2b. Softening of the backfill response occurred after passing the peak resistance.

Figure 5.14 presents the assembled horizontal force-displacement curve, where Δ_x represents the horizontal wall displacement and F_x represents the horizontal component of the actuator force applied to the abutment wall. Continuity between T8.0-2a and T8.0-2b was achieved by horizontally shifting the force-displacement curve for T8.0-2b to match the force levels and slope of the T8.0-2a curve. The T8.0-2a force level and slope at a wall displacement of 1.5 inch (3.8 cm) match well with the force and slope of T8.0-2b at roughly 4.4 inch (11.2 cm). Therefore, the horizontal shift was applied to the backbone curve for T8.0-2b by 2.9 inch (7.4 cm) to match T8.0-2a, thereby creating an essentially “continuous” curve. T8.0-2b exhibited a softer initial stiffness than T8.0-2a, and as such does not contribute to the assembled curve prior to the point where curves from T8.0-2a and T8.0-2b meet.

Combining the backbone curves from T8.0-2b and T8.0-2c is complicated by the termination of T8.0-2b before force levels were zeroed, so it is unclear how much wall displacement is recovered when the wall is completely unloaded. We estimate this displacement recovery from T8.0-2c, where the recovered displacement from the final (residual) point on the backbone curve to zero is about 0.8 in (2 cm). The unloaded force in T8.0-2b is significantly larger than the residual unloaded force in T8.0-2c. The recovered displacement from T8.0-2b is estimated from a common unload modulus as 1.0 – 1.1 inch (2.6-2.8 cm). We recognize that process by which the three backbone curves were stitched together is somewhat arbitrary and there is uncertainty in actual wall displacement levels for the second and third portions of the backbone curve. We expect that the actual displacement level for peak resistance may vary up to 0.4 inch (1 cm) from the level reported by our composite backbone curve.

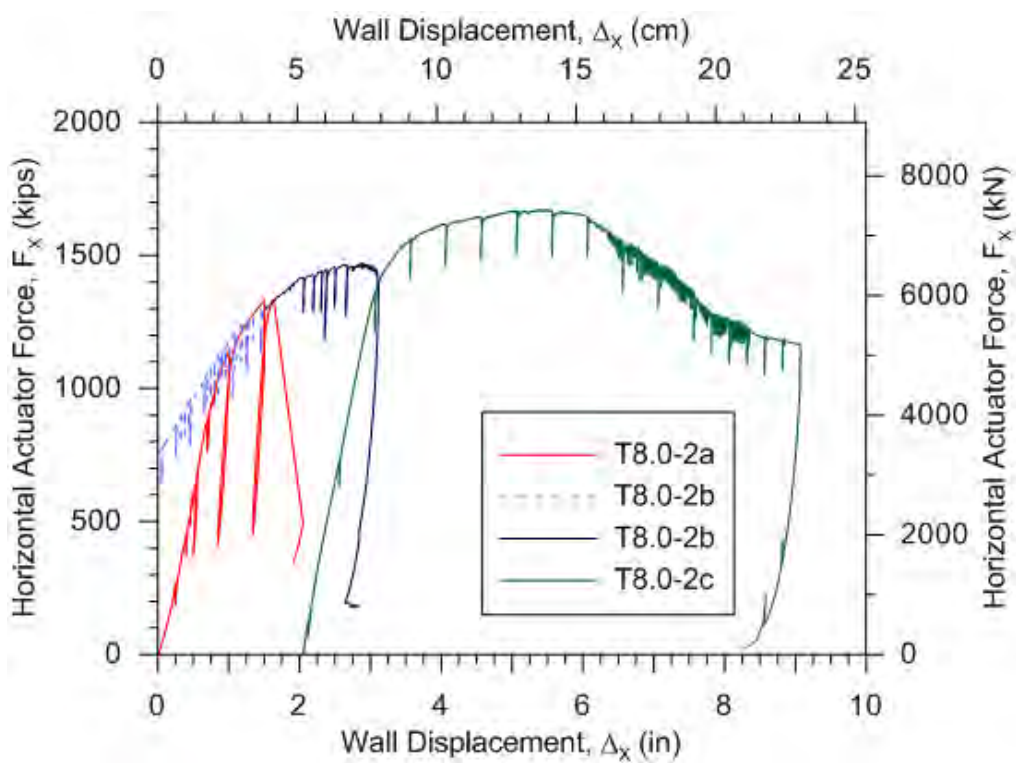


Figure 5. 14 Combined horizontal load displacement relationship for T8.0-1 a,b & c

5.2.2 Passive Capacity of Backfill Specimen and Force-Displacement Shape

The combined backbone curve shown in Figure 5.13 for T8.0-1 must be corrected for base friction to define the passive soil resistance. The base friction results used to make this correction were shown in Figures 5.1 and 5.2 and described in Section 5.1.1; we use a smoothed and extended version of the backbone curve from the base friction data for the purpose of the correction. The base friction correction for $\Delta_x > 1.5$ inch (3.8 cm) is constant at 40 kip (178 kN) and 0 kip in the horizontal and vertical directions, respectively. Those force levels are based on the measured data $\Delta_x = 3.0$ inch (7.5 cm), since data recorded at larger Δ_x may be inaccurate for the reasons given in Section 5.1.1. Figure 5.15a&b show a fitted baseline correction along with the data for horizontal and vertical friction components.

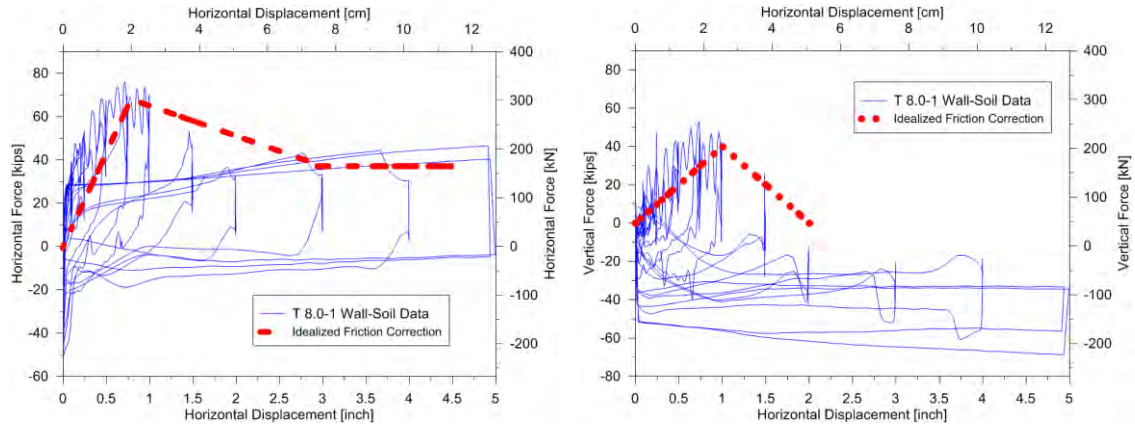


Figure 5.15 a & b: Idealized friction corrections for horizontal and vertical force components

Figure 5.16 shows the passive load displacement relationships for the horizontal, vertical and total force components after the base friction correction. The maximum horizontal and vertical passive components are 668 kips (2970 kN) and 250 kips (1110 kN) in the horizontal and vertical direction respectively. The total passive capacity P_p was calculated from the P_x and P_z components and reached a maximum of 707 kips (3150 kN) at the horizontal displacement level of 6 inch (15 cm). This corresponds to a normalized displacement Δ_{max}/H of 0.06, which is comparable to the range of normalized deflections of 0.03-0.052 measured by Rollins and Cole (2006).

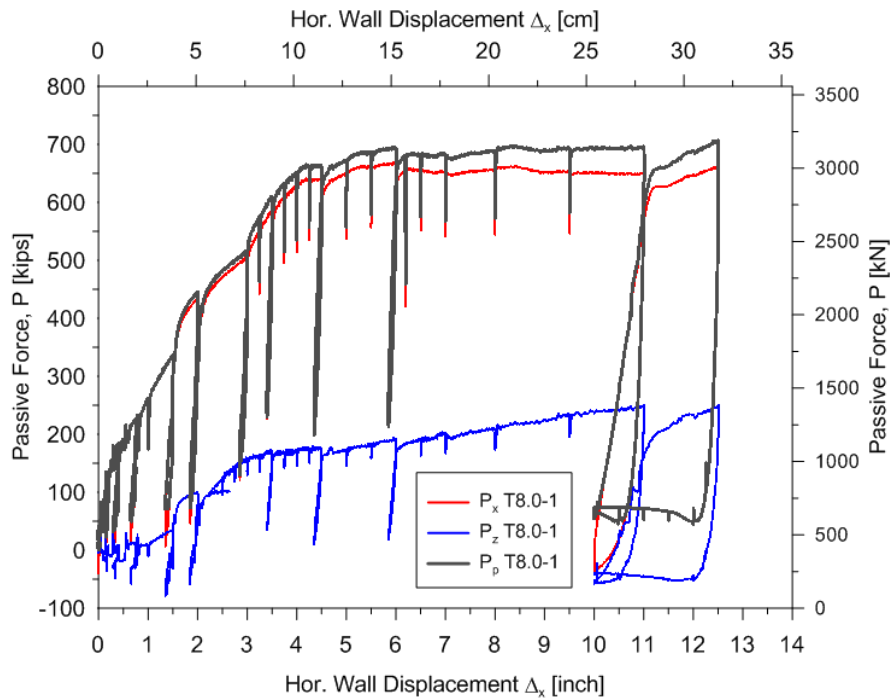


Figure 5.16 Passive load displacement relationships for T8.0-1

If the soil stress distribution against the wall under passive conditions is triangular (confirmed in Section 5.2.5), the passive earth pressure coefficient can be calculated as:

$$K_p = \frac{2P_p}{\gamma H^2 w} \quad (5.1)$$

For specimen T8.0-1, we find $K_p = 10$ using Eq. (5.1) with $P_p = 707$ kips, $\gamma_{tot} = 128.15$ pcf, $H = 8.0$ ft and wall width $w = 17$ ft (5.18m).

For T8.0-2, the combined backbone curve presented in Figure 5.14 must be corrected for base friction as well to define the passive soil resistance. As shown in Figure 5.17, we fit a bilinear relationship to the load-deflection base friction data presented in Figure 5.3, which is elastic to 0.7 inch (19 mm) and plateaus at a horizontal resistance of 70 kips (310 kN). The vertical relationship is also elastic to 0.75 inch (19 mm) and plateaus at 56 kips (250 kN).

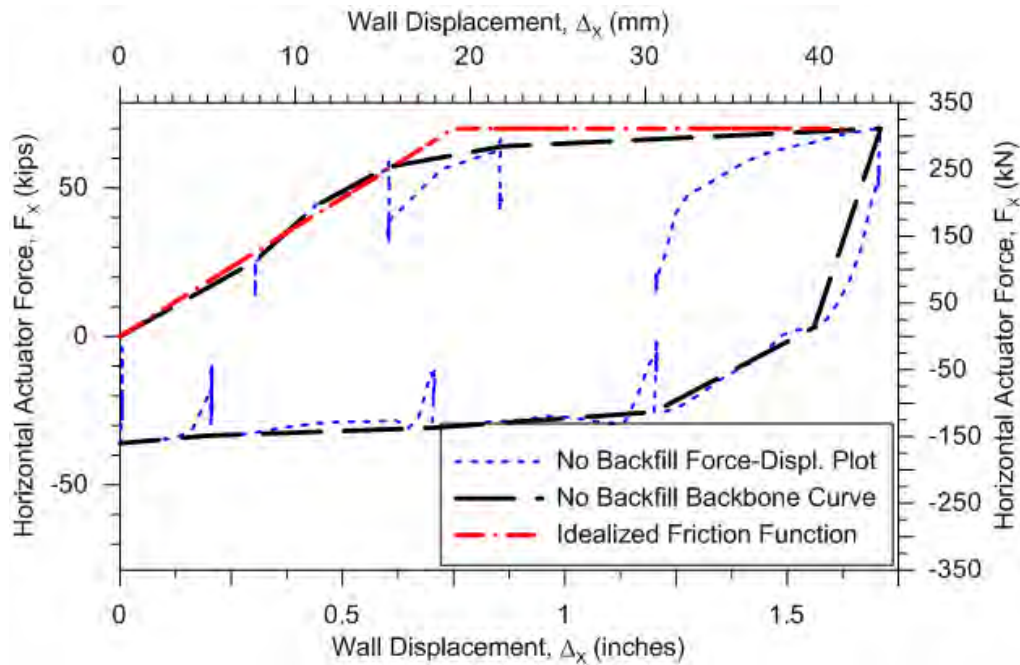


Figure 5.17 Idealized friction correction for the ‘no backfill’ data recorded for test T8.0-2 for the horizontal force component

The combined backbone curve in Figure 5.14 can now be corrected by subtracting the base friction appropriate for a given level of horizontal displacement. Because the testing with backfill extends to much larger displacements than the no-backfill tests, the correction requires extending the plateau of the base friction relationship to larger displacements (i.e. to test segments T8.0-2b & c), which we feel is justified based on observations discussed in Section 5.1.3. Following this correction, the resulting horizontal passive resistance exhibited by the backfill specimen is shown in Figure 5.18. Figure 5.19 shows the combined plots of total passive force along with horizontal and vertical components. Total passive resistance peaks at approximately 1650 kips (7340 kN) at a displacement level of about 5.5 inches (14 cm). The displacement level corresponds to a normalized deflection $\Delta_{\max}/H = 0.057$, which is comparable to the range of normalized deflections of 0.03-0.052 measured by Rollins and Cole (2006). Considering the uncertainty in the displacement level at peak resistance as mentioned in Section 5.2.1, the normalized deflection likely falls within the range of $\Delta_{\max}/H = 0.053$ to 0.061 (5.0 -6.0 inches or 13 to 15 cm).

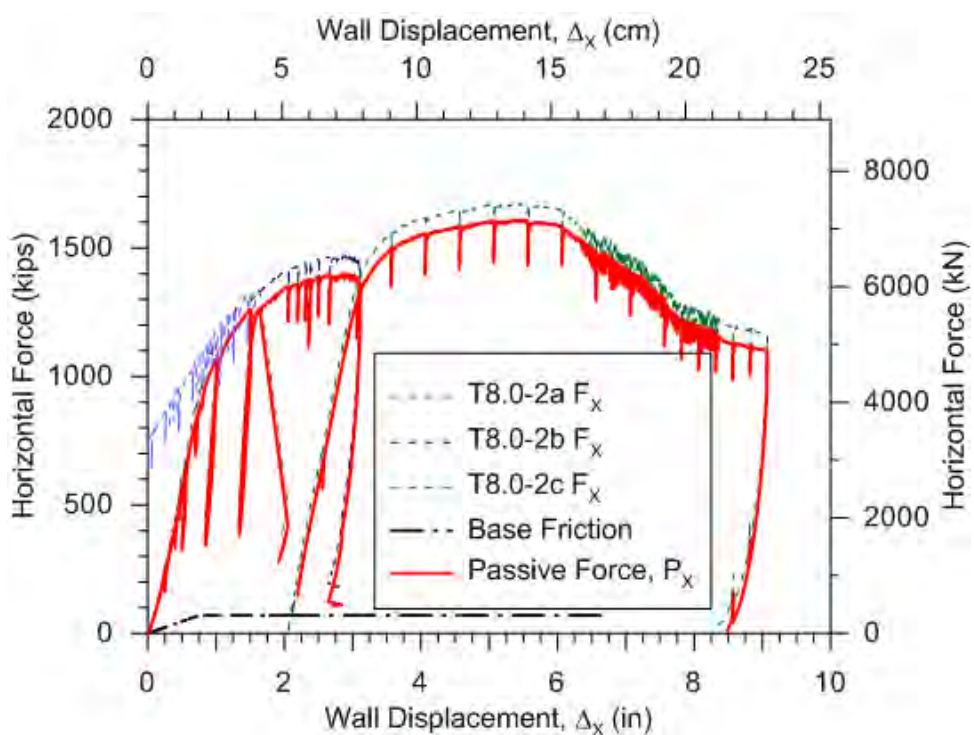


Figure 5.18 Horizontal passive resistance P_x for T8.0-2

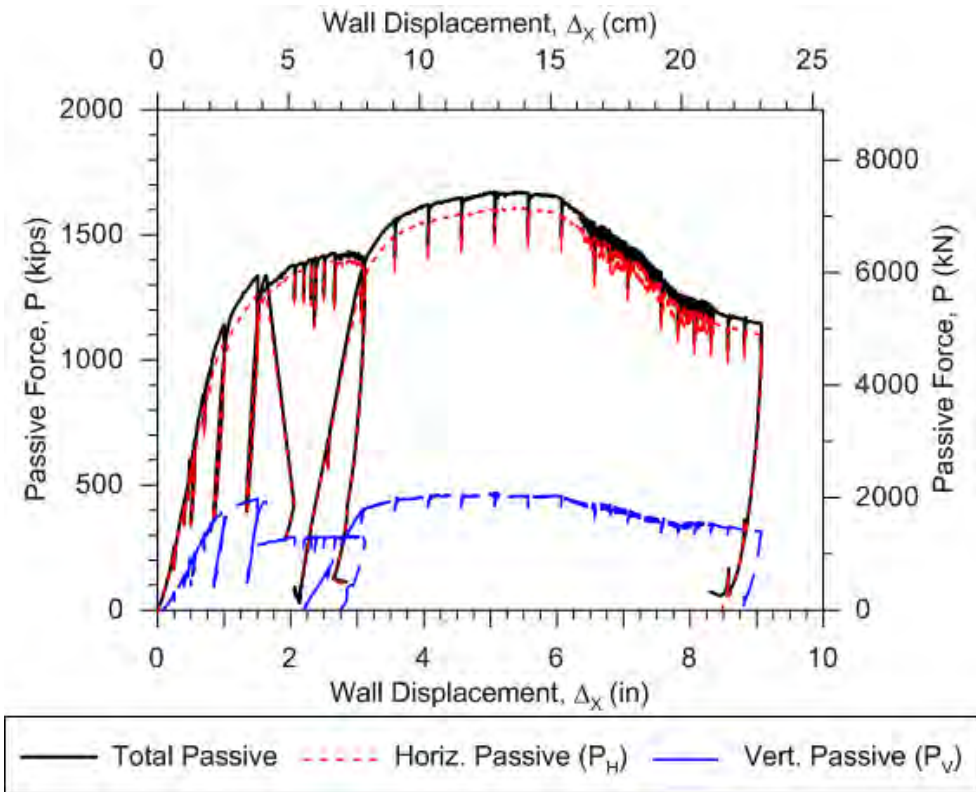


Figure 5.19 Combined passive resistance P_x , P_z and P_p for T8.0-2

The passive earth pressure coefficient can be calculated using Eq. 5.1 as 24 and 17 for the maximum and large-strain (approaching residual) conditions, respectively. For the K_p calculations, the following parameters were used: $P_p = 1650$ kip (7340 kN) and 1124 kip (5000 kN) for maximum and large-strain conditions, respectively; $\gamma=128$ pcf (based on sand cone results), $H=8.0$ ft (2.43 m), and $w=17$ ft (5.18m).

5.2.3 Initial Loading and Unload/Reload Moduli

The initial stiffness was compared with stiffness of the reloading cycles. A linear fit was passed through the loops of the cycles as presented in Figure 5.20. The calculated stiffness values were then plotted versus horizontal displacement as shown in Figure 5.21. It can be seen that the initial stiffness is the smallest measured value and stiffness increases with lateral displacement level. One possible explanation for this increasing behavior is the development of full contact pressure between the abutment wall and the

backfill material, since small lateral displacements of the wall away from the backfill were observed during compaction with the heavy vibratory roller equipment. The initial stiffness was measured to be 43.3 kip/in ft (239.4 kN/cm/m) using a wall width w of 17 ft (5.18 m). T8.01-b started out at a very high stiffness of 202 kip/in ft (1117 kN/cm/m), which is associated with the stiffness once full contact was established during test continuation of stage T8.0-1b. Subsequent cycles indicate a stiffness reduction to 124 kip/in ft (685 kN/cm/m) at the displacement levels [i.e. $\Delta \sim 5.0 - 6.0$ inches (12-15 cm)] where maximum passive capacities were obtained. Results at this displacement level also match the final values of stage T8.01a.

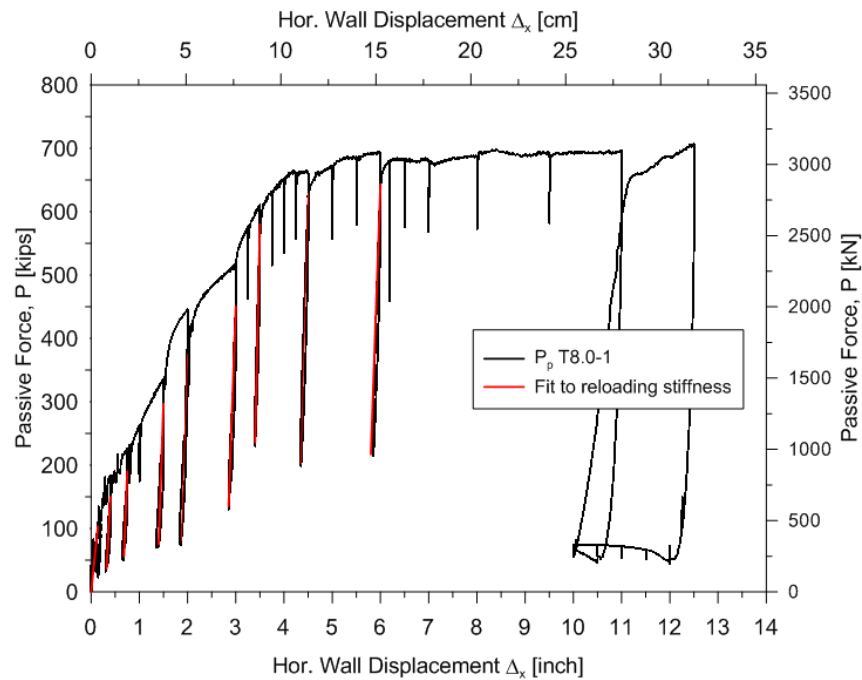


Figure 5.20 Linear fit to initial and reloading stiffness using the passive force –displacement relationship

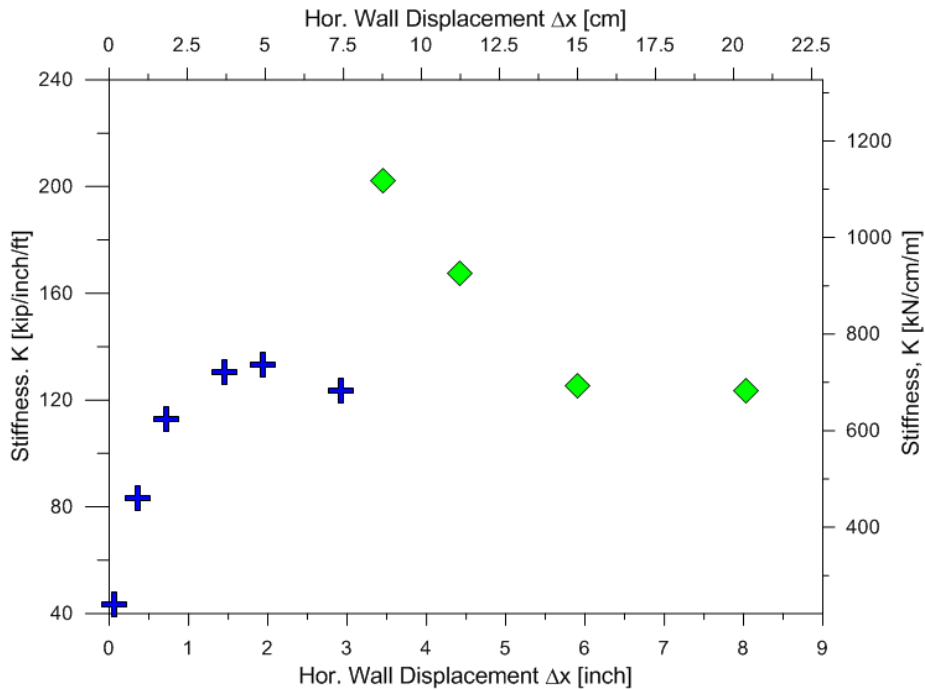


Figure 5.21 Initial and reloading stiffness versus horizontal displacement

Figure 5.22, shows the backbone curve for T8.0-2a and the fitted linear stiffness functions. The fits exhibit a slight ramp-up in stiffness over the first 0.4 inch (1.0 cm) of displacement (possibly from closure of minor gapping caused by wall displacement during compaction). “Initial” stiffness from T8.0-2a is therefore calculated after this initial hardening, which provides a modulus of 86 kip/in/ft (496 kN/cm/m). This initial modulus can be compared to that from test T8.0-2c, which was performed shortly after T8.0-2b and had no gap closure. The initial modulus from T8.0-2c was 85 kip/in/ft of wall (490 kN/cm/m of wall), which nearly matches the post-hardening modulus from T8.0-2a.

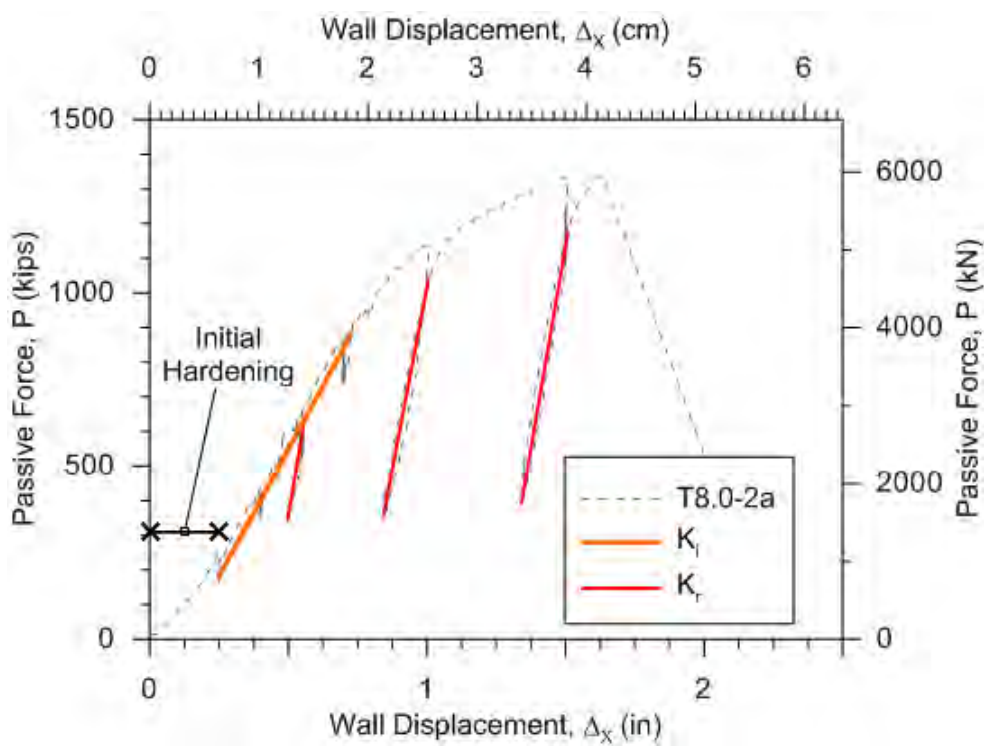


Figure 5.22 Force-deflection relationship for T8.0-2a showing initial hardening behavior and evaluation of initial and unload/reload moduli

Numerous unload-reload cycles were performed during all three testing phases from which unload-reload moduli (K_r) can be evaluated. As shown in Figure 5.22, the reloading stiffness K_r was evaluated by taking a secant modulus between the transition point from unloading to reloading, and the cross-over point where reloading displacement surpasses the unloading phase. Figures 5.23-5.24 illustrate the relationship between unload-reload moduli and horizontal displacement.

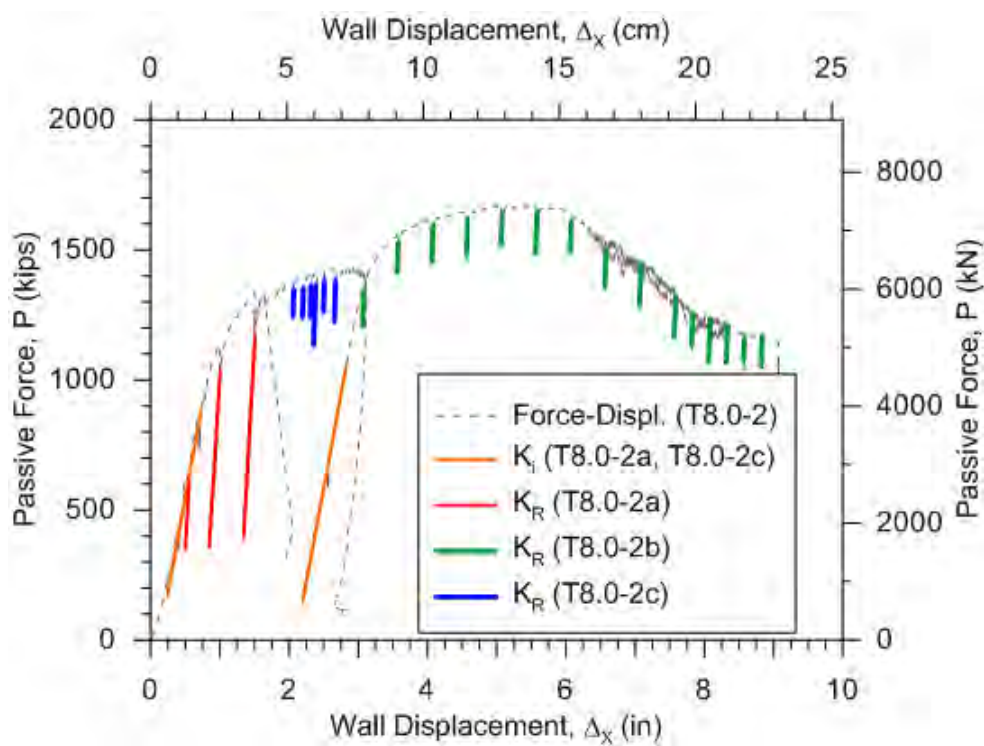


Figure 5.23 Composite load-deflection relationship for T8.0-2 showing initial and unload-reload stiffness

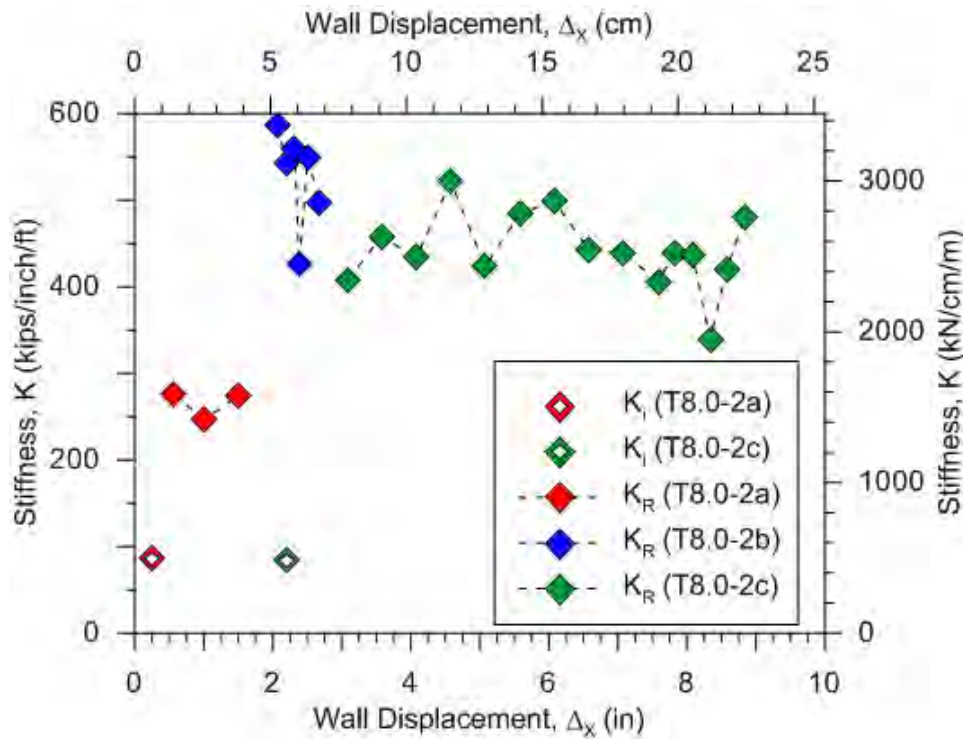


Figure 5.24 Initial and unload-reload stiffness vs. wall displacement. Note that the “initial” stiffness

5.2.4 Mobilized Interface Friction Angle

The passive soil resistance at the wall-soil interface has horizontal and vertical components and is often described in terms of a mobilized interface friction angle,

$$\delta_{iw}(\Delta_x) = \tan^{-1}\left(\frac{P_z(\Delta_x)}{P_x(\Delta_x)}\right) \quad (5.2)$$

where $P_z(\Delta_x)$ and $P_x(\Delta_x)$ are the vertical and horizontal forces applied to the wall at displacement level Δ_x , respectively. The term “mobilized” is used because the interface friction at a given level of horizontal displacement (Δ_x) is generally less than the maximum possible value at the point of shear failure at the interface.

The passive load-deflection relationships corrected for base friction, shown in Figure 5.16 and Figure 5.19 , are used with Eq. 5.1 to calculate the mobilized friction angle (δ_{iw}). A source of uncertainty in this calculation is whether the wall self-weight should be added to the measured value of $P_z(\Delta_x)$. If the diagonal actuators act to remove any vertical displacement such that the vertical reaction force on the wall from the underlying soil does not change during testing, then the self-weight should not be included. On the other hand, if there is enough wall displacement for vertical lift off (which would be a very small amount, likely below our measurement tolerance), then the wall self-weight should be added to the vertical component of the actuator forces for the $P_z(\Delta_x)$ term in Eq. 5.1. Inclusion of the wall weight affects the internal friction angle by approximately 4-5 degrees in both tests. Figures 5.25 and 5.26 plots δ_{iw} for the backfill tests T8.0-1 and T8.0-2 respectively, considering both cases – with and without wall self-weight.

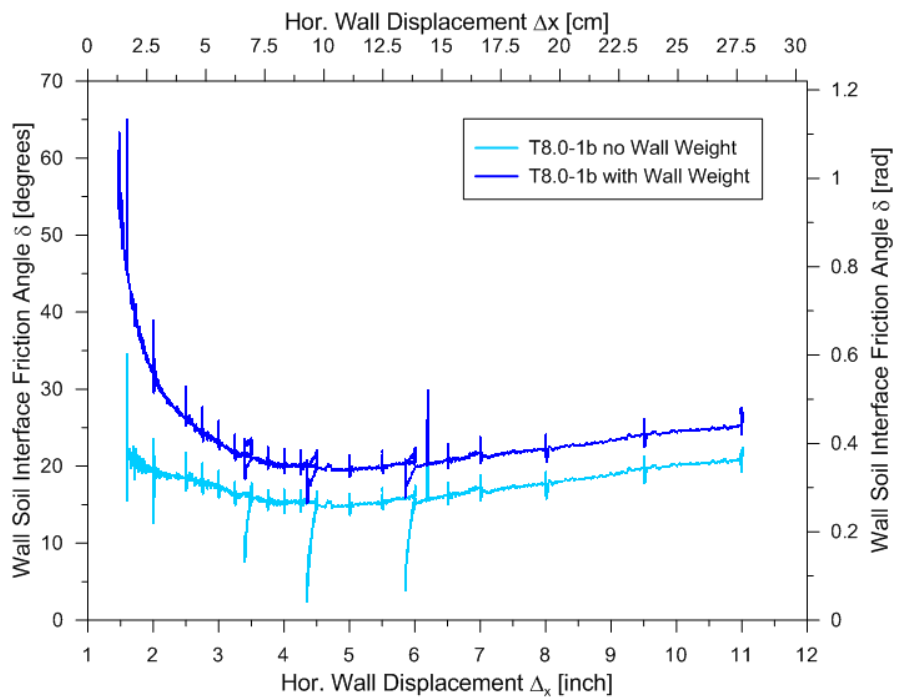


Figure 5.25 Wall soil interface friction angle for T8.0-1

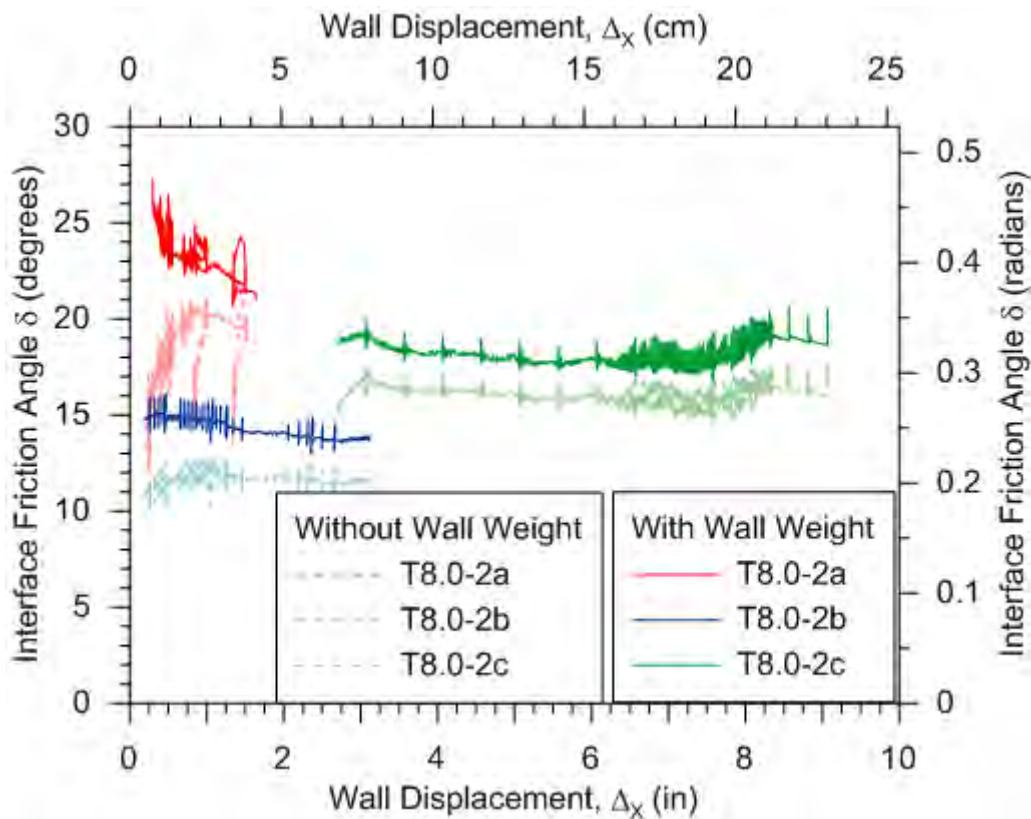


Figure 5.26 Wall soil interface friction angle for T8.02

Mobilized friction angle varies with Δ_x and test interval. Calculations neglecting the self-weight of the abutment wall yielded values between 11-15 degrees (T8.0-1a; T8.0-2b) and 23-25 degrees (T8.0-1b; T8.0-2a); accounting for the self-weight reduced the range to between approximately 8 to 20 degrees. At the displacement level corresponding to the peak passive force (5.5-6.0 inch or 14-15 cm), the mobilized friction angle ranged between 15 and 20 degrees and was fairly consistent for T8.0-1 and T8.0-2. These results can be compared to the interface friction angle range for T5.5 test of 13 to 20 degrees, with the peak resistance occurring at δ_{lw} equal to 13.6 degrees; those values are similar to what we find in the present set of tests.

As discussed in Chapter 4, the average peak friction angle obtained from triaxial tests was 34.5 degrees. The range of interface friction angles corresponding to the peak passive resistance of the backfill specimen translates to $0.43\phi'$ to $0.58\phi'$. The smoothness associated with formed reinforced concrete may account for the relatively low mobilized friction angles.

5.2.5. Earth Pressure Distribution

The backwall specimens used in T8.0-1 and T8.0-2 were furnished with a grid of soil pressure sensors as depicted in Figure 3.5. For T8.0-1 only the vertically aligned pressure sensors 1-8 were present. A grid of horizontal pressure cells (9-16) was added for T8.0-2. Not all sensors functioned throughout the entire test period; sensor functionality was previously summarized in Table 3.1. As shown in Figure 5.27, all sensors appear to have provided reliable data for T8.0-1 (data in figure are from T8.0-1a). The data reflect the pushing and holding cycles during the application of lateral wall displacements. Figure 5.28 shows the pressure distribution vs. the lateral displacement of the wall into the backfill material. The pressure-displacement results indicate a low modulus and large failure strains (i.e., strain at peak lateral earth pressure) for the pressure sensors located near the surface of the backfill material (e.g., PS8), due to the relatively low confining pressures in this region. On the other hand, deeper sensors recorded stiff moduli and relatively small failure strains (e.g., PS1 and PS2). Strain softening behavior associated with dilatancy would be expected at all depths throughout the backfill material, but only

manifests at larger depths because the strains are not large enough to mobilize this behavior near the surface.

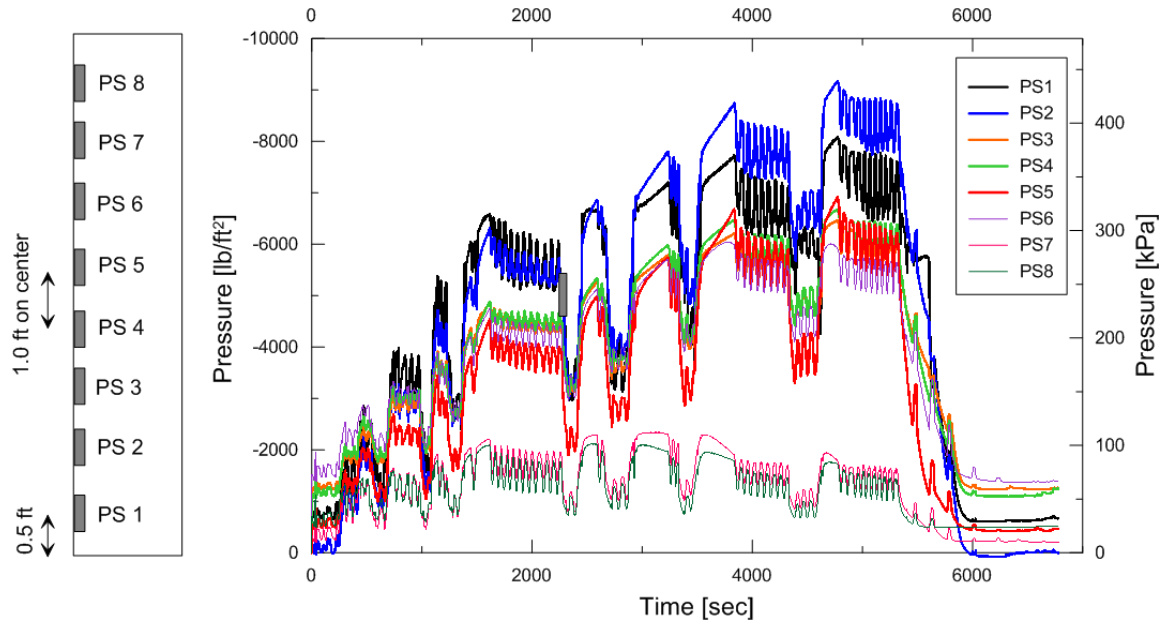


Figure 5. 27 Pressure sensor recordings vs. time for T8.0-1a

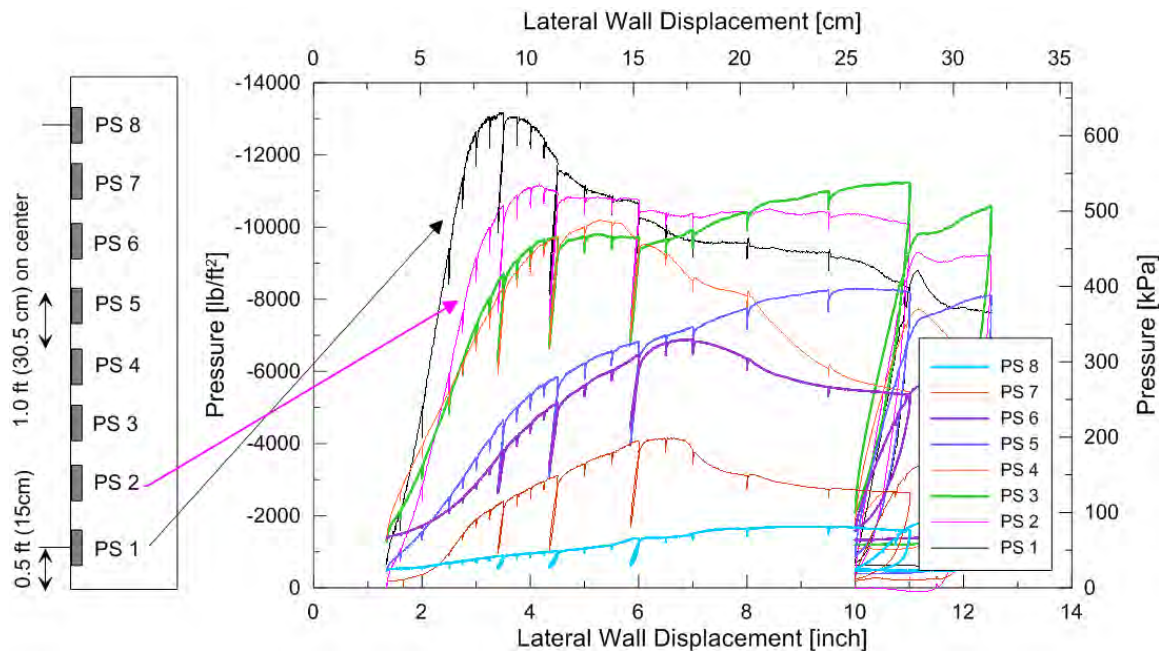


Figure 5. 28 Pressure versus lateral wall displacement for T8.0-1b

Figure 5.29 shows the vertical earth pressure distribution for three representative lateral displacement levels (at small, intermediate, and near capacity) of 1.0 inch (2.5cm),

3.5 inch (8.9 cm) and 5.0 inch (12.7 cm) along with a linear fit to the data. The pressure sensors indicate a nearly linear increase of passive earth pressure with depth, which is compatible with a low cohesion shear strength and the use of Eq. (5.1). Table 5.1 compares resultant passive forces computed from the earth pressure distributions (using the area underneath the linear fit in Figure 5.29) to the measured resultant actuator forces. Back-calculated passive capacities are reasonably consistent with the actuator data, indicating that the soil pressures, as expected, are providing essentially the full resistance to wall movement. The wall width taken for this calculation was $w = 15\text{ft}$ (4.6 m)

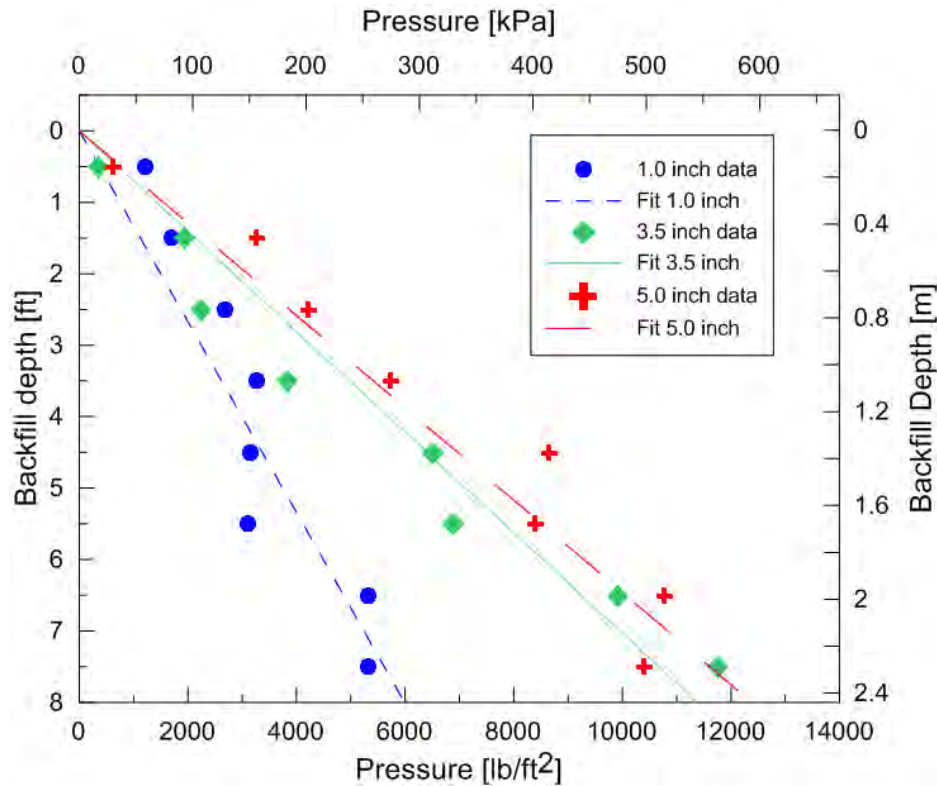


Figure 5. 29 Earth pressure distribution for lateral displacement levels of 1.0, 3.5 and 5.0 inch

Table 5.1 Comparison between measured capacities from hydraulic equipment and earth pressure sensors.

Displacement Level [inch (cm)]	P _p measured using hydraulic system [kip (kN)]	P _p back-calculated from earth pressure distribution [kip (kN)]	% Difference [Error]
1.0 (2.5)	260 (1157)	360 (1601)	28 %
3.5 (8.9)	590 (2624)	683 (3038)	14 %
5.0 (12.7)	675 (3003)	743 (3305)	9 %

5.3. Mapped Crack Patterns

5.3.1 Surface of Backfill

Photographs showing the surface crack layout observed after completing T8.0-1 are shown in Figure 5.27 and 5.28. Large horizontal cracks were observed throughout the entire failure surface up to the point of the surface intersection of the major failure plane. Backfill heave was observed between 0.6 m (2ft) and 4.3 m (18ft) behind the abutment wall and is shown in Figure 5.28 and 5.29. Wingwall bulging of up to 5-8 cm (2-3 inch) was recorded on both sides of the test specimen.



Figure 5. 30 Surface cracks on the backfill of T8.0-1 marked in green color



Figure 5. 31 Backfill upheave and major cracking at the location where the principal failure plane intersects with the surface



Figure 5. 32 Photograph of backfill upheave along the wingwalls of the specimen

For T.8.0-2, backfill surface cracking was monitored and mapped throughout each day of testing. Figures 5.16-5.19 show the intermediate and final surface cracks as the backfill deformed for test T8.0-2. The first observable main failure crack opened at a displacement level of approximately 12.7 cm (5.0 inches). This network of cracks formed between 7.9 and 8.5 m ($3.25H$ to $3.5H$, where H = backwall height) behind the face of the wall across the full width of the backfill. These cracks were later shown to be the intersection of the principal failure plane with the ground surface. Numerous smaller cracks also appeared approximately 1.5 m (5 ft) behind the wall face. Long, isolated cracking was also observed both perpendicular and parallel to the direction of wall movement; these are most likely manifestations of the top of fill expanding as the wedge of soil displaced upwards above the main failure surface.

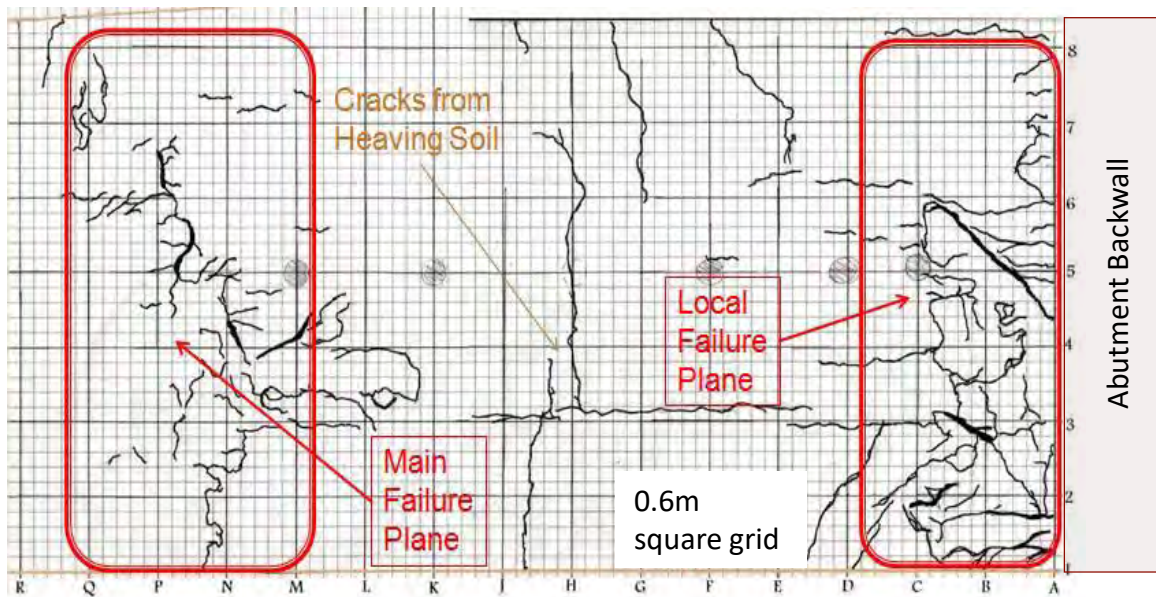


Figure 5.33 Plan view of surface cracks with highlighted regions for test T8.0-2



Figure 5. 34 Surface Cracks after test T8.0-2a. Left: Cracking near Grid A-1, Right: Cracking near Grid B-3

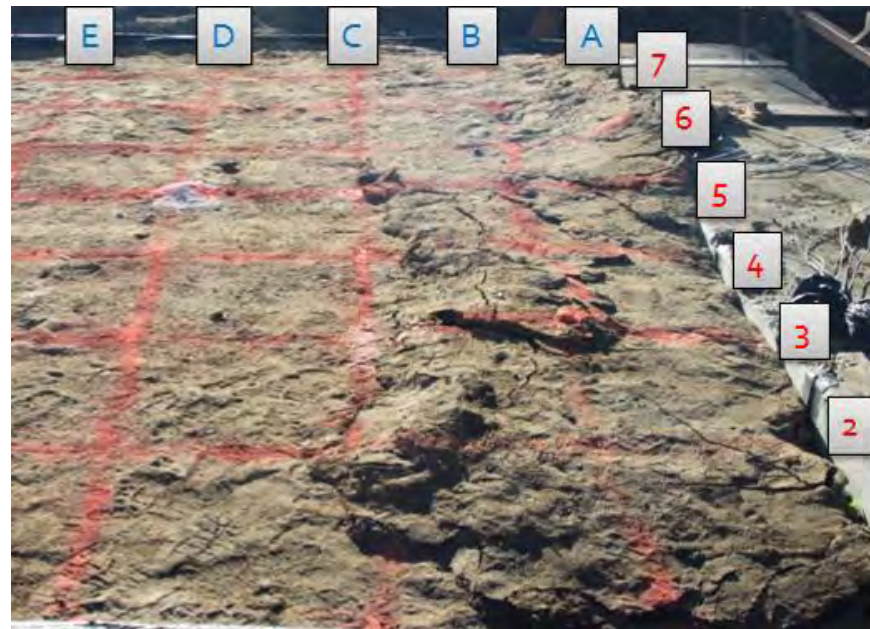


Figure 5. 35 Local Cracking after T8.0-2c

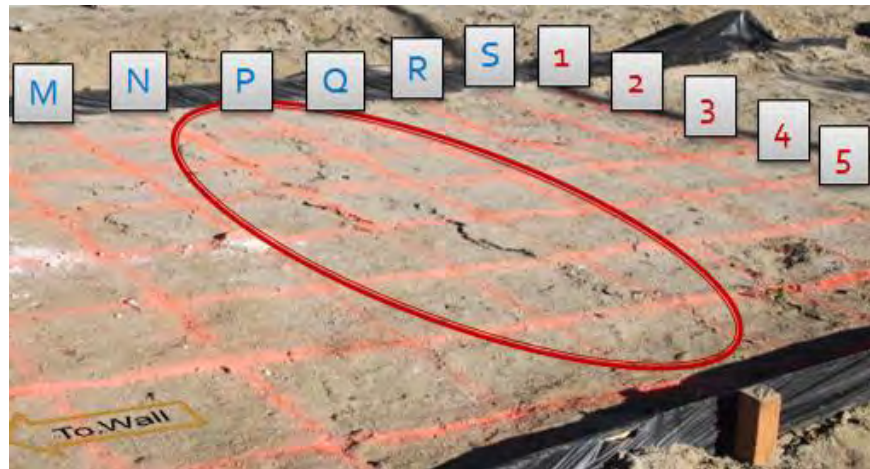


Figure 5. 36 Main Failure Surface Crack after T8.02c

5.3.2 Post-Test Trenching of Slip Surfaces

Following backfill placement but prior to testing, low strength gypsum columns were cast into hand-augured 10 cm diameter boreholes for T8.0-1 and T8.0-2. By trenching along these gypsum columns following testing, we investigated the locations of subsurface shear surfaces. As shown in Figure 5.34, seven columns were installed at distances of 61.0, 122, 183, 305, 427, 549, and 671 cm (24, 48, 72, 120, 168, 216, and 264 inches) from the soil-backwall interface. Each column extended through the full depth of fill and into the underlying natural clay.

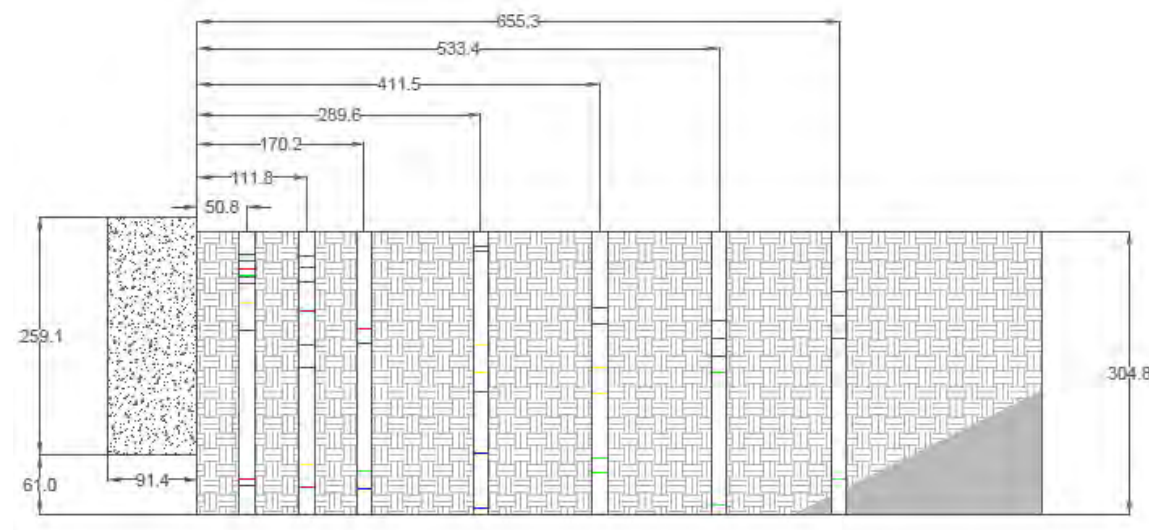


Figure 5. 37 Elevation View of Backfill with Gypsum Column Locations for T8.0-2

Post-test trenching was performed in stages due to safety limits on the height of vertical cut that can be made above an area to be person occupied (maximum height of 1.5 m). We excavated in 1.5 m intervals, mapped the exposed face of the backfill and gypsum columns, removed the remaining portion of the backfill, and then excavated the next 1.5 m interval. This process was continued until the full depth of backfill and a portion of the underlying natural soil had been exposed and mapped.

Figure 5.35 – 5.37 are images of the excavated face for T8.0-2 and T8.0-1 marked with depths where the columns were sheared. As illustrated in Figures 5.34, the failure surface initiated near the base of the wall, extended downward about 2- 4 inches (5-10 cm), and then extended upwards through the backfill reaching the surface approximately 26 ft (8 m) from the wall. The shape of the failure plane was approximately log-spiral. As shown in Figure 5.34, additional shear surfaces were mapped in the columns above the principal failure surface. No shearing was observed in the natural soils underlying the backfill. Figure 5.36 and 5.37 show more photographs during the excavation of T8.0-1.



Figure 5.38 Combined images of backfill excavation and gypsum column ruptures for T8.0-2



Figure 5. 39 Trace off failure surface observed for T8.0-1



Figure 5. 40 Photograph showing the initiation of the major failure surface at the bottom of the wall for T8.0-1

6. Analytical and Numerical Modeling

Section 2.3 provided an overview of simulation models that can be used to analyze the lateral response of bridge abutments. In this chapter we describe two bodies of work: (1) extension of the hyperbolic force-displacement (HFD) method to account for backwalls of varying height and (2) presentation of HFD and log-spiral hyperbolic (LSH) model predictions for the tests described in Chapter 5.

6.1. Development of a HFD Model Incorporating Abutment Height Effects

As described in Section 2.3.2, the hyperbolic force-displacement (HFD) model is a two-parameter hyperbolic equation that can be fit to test data or the results of more advanced analyses. Section 2.1 described the results of two field-scale tests of seat-type abutment wall systems that form the basis for current Caltrans Seismic Design Criteria (SDC) for backwalls (Caltrans, 2010). The tests were reviewed in Section 2.1, the SDC criteria derived from the tests are summarized in Section 2.2, and curve-fitting of the HFD model to the results of the two tests was briefly described in Section 2.3.2. Both tests and the corresponding HFD curve-fits apply for abutment backwall heights of 5.5 ft (1.68 m). In this work we extend the HFD models for varying backwall heights. This work has been published previously by Shamsabadi et al. (2010).

6.1.1 HFD Representation of Test Results for 1.68 m (5.5 ft) Tests

The expression for the HFD model, originally given in Eq. 2.3, is re-written temporarily as:

$$\frac{P(y)}{w} = \frac{Cy}{1 + Dy} \quad (6.1)$$

where $P(y)$ is the lateral force on the retaining wall corresponding to lateral deflection y , w is wall width, and constants C and D can be related to the parameters shown in Figure 2.4 that describe the curve shape

$$C = \left(2K_{50} - \frac{P_{ult}/w}{y_{max}} \right) \quad D = 2 \left(\frac{K_{50}}{P_{ult}/w} - \frac{1}{y_{max}} \right) \quad (6.2)$$

Recall that P_{ult} is the maximum abutment wall force developed at displacement y_{max} , $K_{50} = P_{ult} / (2wy_{50})$ is the average abutment stiffness per unit width of wall, and y_{50} is the displacement at half of the maximum abutment force. Values of the parameters controlling the shape of the HFD curve (i.e., P_{ult} and y_{max}) can be obtained from more advanced analyses (such as LSH simulations) or from tests conducted on scaled or full-size models.

The residual resistance of the backfill, the displacement at which this residual is reached, and the average stiffness values obtained from the UCLA and UCD abutment tests are listed in Table 6.1. Using these data, constants C and D can be readily calculated using Eq. (6.2). The use of these values in Eq. (6.2) will yield lateral resistance per unit width (meter or ft) of the abutment backwall. The maximum value of the lateral displacement (y_{max}) is 5% and 10% of the abutment height for T5.5 and the UCD test, respectively. In both tests, the abutment heights were $H = 1.68\text{m}$.

Table 6. 1: Abutment Backfills Parameters for UCLA and UCD Abutment Tests.

Site/Backfill Type	P_{ult}/w (kN/m, kips/ft)	K_{50} (kN/cm/m, kips/in/ft)	y_{max} / H
T5.5 (SE30)	450, 30	290, 50	0.05
UCD (cohesive)	450, 30	145, 25	0.10

6.1.2 HFD Model Extension for Backwall Height Effects

The HFD constants listed in Table 6.1 are applicable for bridge abutments with a backwall height $H = 1.68\text{ m}$, as was used in the UCLA and the UCD tests. To develop backbone curves for other wall heights, the term C can be modified by a height-adjustment factor as follows

$$\frac{P(y)}{w} = \frac{ay}{1+by} \left(\frac{H}{H_r} \right)^n \quad (6.3)$$

where, as before, $P(y)/w$ is the lateral force per unit width of the backwall at lateral displacement y ; a and b are two *new* parameters for representing the HFD curves; $(H/H_r)^n$ is a backwall *height adjustment factor* in which H is the backwall height, H_r is the reference backwall height (henceforth chosen to be $H_r = 1$ m) and n is a dimensionless exponent. This expression may be termed as the *Extended HFD* equation (EHFD), and a comparison with Eq. (6.1) establishes that $C = a (H / H_r)^n$ and $D = b$.

The parameterization in Eq. (6.3) can be visualized with the assistance of classical Rankine-Bell passive earth pressure theory (see, for example, Bowles, 1996), which states that

$$\frac{P_p}{w} = \frac{1}{2} \gamma K_p H^2 + 2c \sqrt{K_p} H \quad (6.4)$$

where P_p/w is the passive capacity of a retaining wall per unit width; γ is the unit weight of the backfill soil; K_p is the coefficient of maximum passive earth pressure; c is the backfill soil cohesion; and H is the wall height. Thus, per the Rankine-Bell equation, the capacity-height relationship is a polynomial function of H . For clean sands (i.e., for $c=0$) the relationship is quadratic ($n=2$), whereas for increasingly cohesive backfills with high cohesive shear strength, the second term will dominate the right-hand side of Eq. (6.4) ($n \rightarrow 1$). For backfills with both cohesion and friction, the exponent in Eq. (6.3) should range within $1 < n \leq 2$.

The parameterization in Eq. (6.3) is not meant to imply that a and b are independent of backwall height. However, we do assume that the asymptote of ratio $ay/(1+by)$ —which is equal to a/b —remains nearly constant with respect to height. The results that follow will demonstrate the accuracy of this assumption. For lack of any other physically justifiable (or a more apparent) choice, we proceed with this assumption and seek to calibrate the values of a , b , and n using numerical LSH simulations.

6.1.3 Evaluation of Height Exponential Factor n

To quantify the effect of abutment wall height, we first compute the ultimate capacities of abutment walls per unit wall-width (P_{ult}/w) with different heights for typical granular and cohesive backfills using the LSH model. After evaluating Eq. (6.3) at $y=y_{max}$, and taking the logarithm, we find

$$\log(P_{ult}/w) = n \log\left(\frac{H}{H_r}\right)^n \quad (6.5)$$

where $d = \log\left(ay_{max}/(1+by_{max})\right)$. Figure 6.1 displays the LSH results obtained for UCLA (granular) and UCD (cohesive) backfill soils for various heights along with linear least squares approximations per Eq. (6.5) to those data. The power-law postulated in Eq. (6.3) captures the height-dependence of the ultimate wall resistance. The magnitudes of the exponent are $n = 1.56$ and $n = 1.05$ for UCLA's granular (silty sand), and UCD's cohesive (clayey silty) backfill soils, respectively. Note that these values of n are only calibrated with respect to ultimate resistance; their applicability for lower displacement levels is investigated in the next section.

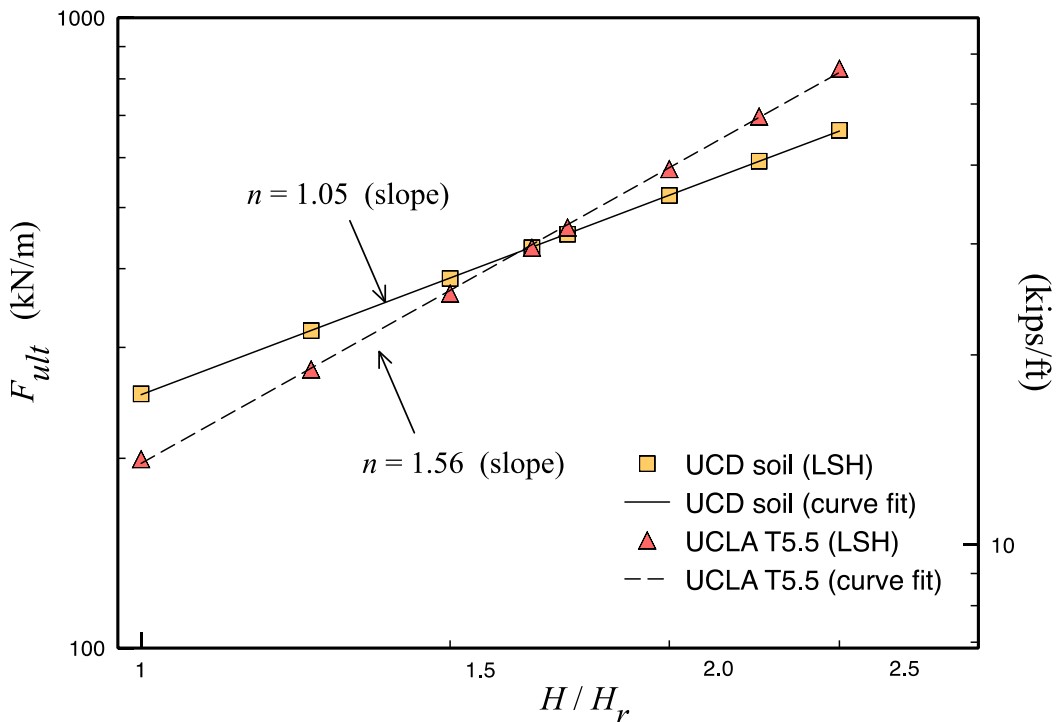


Figure 6.1 Variation of the backwall capacity per unit width versus normalized backwall height (reproduced from Shamsabadi *et al.* 2010).

6.1.4 Re-Calibration of EHFD Coefficients

Utilizing the above value of exponent n , we perform a secondary minimization problem to estimate a and b . For a given value of n and backwall height H , we compute the complete lateral response backbone curve of an abutment—with either UCLA or UCD backfill—up to y_{max} using the LSH model. The difference between this backbone curve, and that predicted by the EHFD curve described in Eq. (6.3) defines an error (objective) function. We minimize this objective function in a least-squares sense with respect to the coefficients a and b . This nonlinear minimization problem is solved using a *Trust Region* algorithm (Matlab, 1997), and we omit the details here for brevity.

Table 6. 2: EHFD coefficients back-calculated using LSH simulation data

Site / Backfill Type	UCLA / granular			UCD / cohesive		
	H (m)	a (kN/cm/m)	b (1/cm)	n	a (kN/cm/m)	b (1/cm)
1.00	410.6	1.867	1.56	249.1	0.8405	1.05
1.25	316.6	1.468	1.56	199.4	0.6755	1.05
1.50	258.4	1.206	1.56	166.1	0.5637	1.05
1.67	230.8	1.073	1.56	149.6	0.5084	1.05
1.75	218.5	1.020	1.56	142.9	0.4856	1.05
2.00	190.2	0.8836	1.56	125.6	0.4270	1.05
2.25	168.7	0.7784	1.56	112.2	0.3811	1.05
2.50	152.8	0.6954	1.56	101.6	0.3446	1.05

Results of this procedure are displayed Table 6.2, from which a and b are found to depend on backwall height. This indicates that the values of n developed in the previous section do not uniquely represent the height effect on abutment performance (i.e., the coefficients do not apply at less than peak resistance). However, it is possible to develop a simpler model—i.e., one for which all dependencies of the right-hand side of Eq. (6.3) on backwall height (H) are described explicitly. For that we first define the following normalized coefficients,

$$\hat{a} = a / a_r, \quad \hat{b} = b / b_r, \quad \hat{H} = H / H_r \quad (6.6)$$

where a_r and b_r are the back-calculated EHFD coefficients for the reference height, $H_r = 1\text{m}$. As shown in Figure 6.2, we then observe that both these coefficients have a simple (and nearly identical) variation with respect to the normalized height parameter H / H_r .

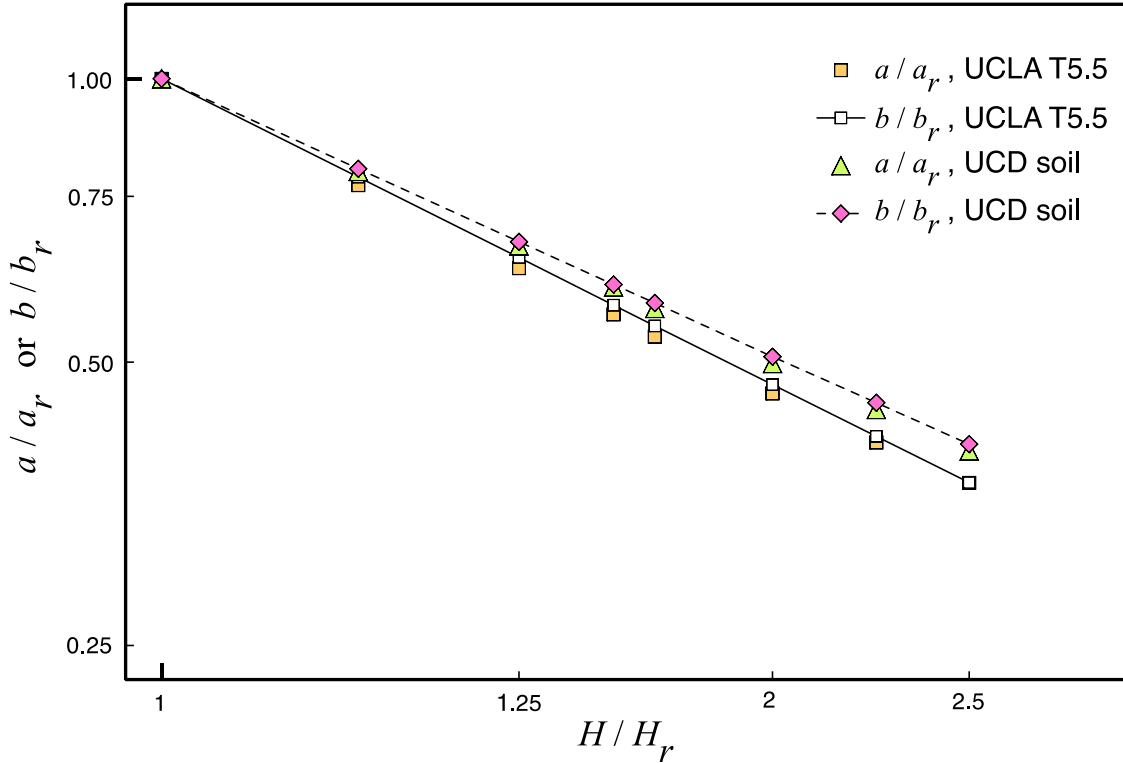


Figure 6.2 Variation of the normalized HFD coefficients versus normalized backwall height (reproduced from Shamsabadi *et al.* 2010).

The four sets of results shown in Figure 6.2 reveal that for both soil types, a simple power-law describes the height-dependence of the EHFD coefficients. This power-law is

$$\hat{a} \approx \hat{b} \approx \hat{H}^{-1} \quad \hat{a} = a / a_r, \quad \hat{b} = b / b_r, \quad \hat{H} = H / H_r \quad (6.7)$$

The actual value of the exponents obtained from linear regression vary between -0.98 and -1.08. We subsequently demonstrate that the selected value of -1.0 provides EHFD curves that approximate LSH curves well for a range of backwall heights. As such, the final form of the EHFD curve is

$$\frac{P(y)}{w} = \frac{a_r y}{\hat{H} + b_r y} \hat{H}^n \quad (6.8)$$

These Extended HFD equations can be used to represent the backbone curve for an abutment backwall having compacted backfill soils matching those in T5.5 or the UCD test. Eq. (6.8) provides an abutment longitudinal displacement at residual capacity (y_{max}) of 0.05H for the granular backfill and 0.1H for the cohesive backfill. The values of the reference coefficients are given in Table 6.2 in *italicized* numerals (these are the values of a and b for $H = H_r = 1$ m). Entering these coefficients into Eq. (6.8) provides expressions for the two backfill types:

$$\frac{P(y)}{w} = \begin{cases} \frac{410.6y}{\hat{H} + 1.867y} \hat{H}^{1.56}, & y < 0.05H \quad (\text{T5.5, SE30}) \\ \frac{249.1y}{\hat{H} + 0.8405y} \hat{H}^{1.05}, & y < 0.1H \quad (\text{clayey-silt}) \end{cases} \quad (6.9)$$

where y is in cm, $P(y)/w$ is in kN/m, and H is in m. Here we note that a unit conversion yields $a_r = 71.5$ Kips/in/ft and $b_r = 4.75/\text{in}$ for the SE30 granular backfill, and $a_r = 41.6$ kips/in/ft and $b_r = 2.16/\text{inch}$ for the clayey silt backfill. For this case $H_r = 3.28\text{ft}$ must be used in Eq. (6.9). The backbone curves in Eq. (6.9) should not be used for backfill materials that are significantly different from those in the tests by Lemnitzer et al. (2009) or Romstadt et al. (1995) tests in terms of strength, cohesion, or compaction condition. Hence, these relations should be considered to be material-specific and should not be generalized to other conditions in the absence of further research.

Figure 6.3 compares backbone curves computed from Eq. (6.9) with the T5.5 (SE30) and UCD experimental results (for $H=1.68$ m) and LSH simulations for $H=1.0-2.5$ m. The agreement between the EHFD and LSH results is good across the range of considered wall-heights and lateral displacements. The comparison with experimental data is also favorable.

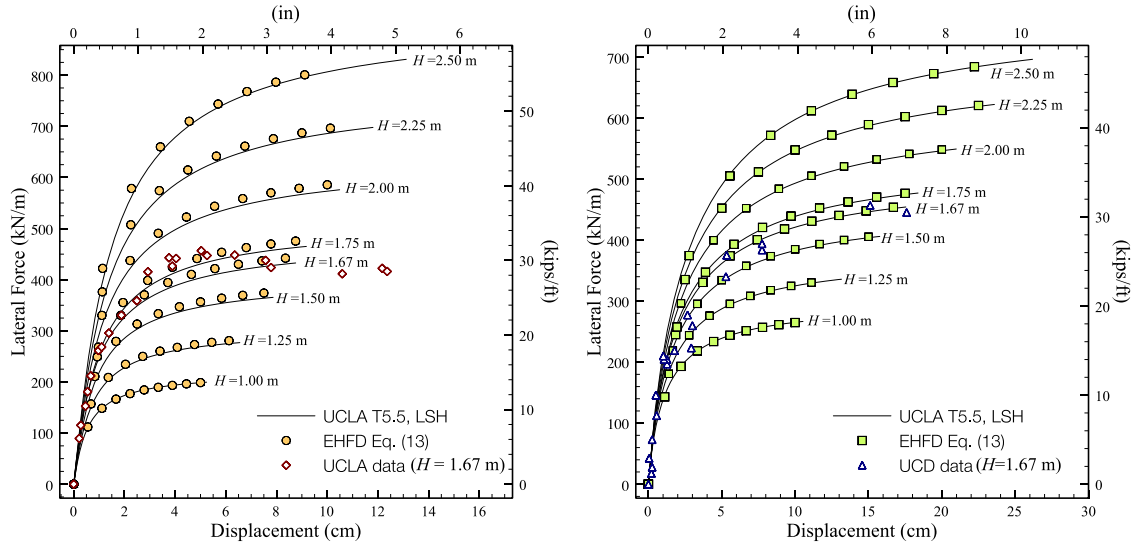


Figure 6.3 Comparison of backbone curves computed using the proposed EHFD equations along with LSH curves and data from the T5.5 and UCD tests (reproduced from Shamsabadi *et al.* 2010).

6.2. Model Predictions Versus Observed Response

6.2.1 Selection of Strength Parameters for Use in Analysis

Section 4.2.2 and 4.2.3 describes the in situ densities and shear strength testing performed on the backfill materials, which appear to be practically identical for tests T5.5, T8.0-1 and T8.0-2. As described in Section 4.2.2, there appears to have been a lower level of compaction for T8.0-1 as compared to T5.5 and T8.0-2, as summarized below:

T5.5: $D_r = 0.92$ (Lemnitzer *et al.*, 2009, p 508). Likely range $D_r = 0.85$ to 1.0.

T8.0-1: $D_r = 0.4$ -0.6. Section 4.2.2 of this report.

T8.0-2: $D_r = 0.9$ -1.0. Section 4.2.2 of this report.

The available shear strength test data, as described in Section 4.2.3, applies for drained shear conditions, a triaxial stress path, and relatively high relative densities (comparable to T5.5 and T8.0-2). Figure 4.14 synthesizes the data for peak strengths from these experiments, and indicates the following results:

Mean $c=25$ kPa, Mean $\phi=34.5$ deg

Range of c (+/- one standard deviation) for the given $\phi=13$ -37 kPa

Range of ϕ (from 95% confidence intervals on fit): 32.6-36.6 deg

The above Mohr-Coulomb parameters represent peak strength conditions. For our calculations, three additional factors need to be considered: (1) how do the parameters change for plane strain conditions?; (2) how do the parameters change for critical state (i.e., residual) conditions?; (3) how do the parameters change for the lower compaction condition in T8.0-1? The manner by which these issues were considered is summarized below.

Plane Strain Shear: Lee (1970) describes the higher drained shear strength obtained in plane strain tests as compared to triaxial tests. Friction angles for plane strain conditions are higher than those for triaxial by amounts ranging from 0-8 deg, with the largest differences associated with dense sands and at low confining pressures (i.e., the most dilatent materials). For the conditions present in the SE 30 material used in field testing, a 5 deg offset in ϕ appears reasonable. This changes our mean peak strength parameters to:

$$\text{Mean } c= 25 \text{ kPa, Mean } \phi=39.5 \text{ deg}$$

Critical State Conditions: There are two approaches to this problem. One is to look at our test data, which is not optimal because the tests do not extend to large strain levels typically associated with critical state conditions. Nonetheless, the results from Figure 4.13 suggest an approximate sensitivity (peak/residual strengths) of about 1.2. The reduced friction angle from this approach is $\phi_{cs}=30$ deg. Sand materials at critical state would not be expected to have significant curvature in the failure envelopes, so a cohesion of $c_{cs}=0$ is selected.

This result can be checked against critical state (or residual) friction angles in the literature, which range from 30-35 deg (Negussey et al., 1988). The value identified from the estimate of sensitivity is within this range. In summary, for residual we use the following parameters:

$$c_{cs}=0, \phi_{cs}=30 \text{ deg}$$

Lower Compaction Levels: Laboratory testing has not been performed for the lower relative density (D_r) conditions that appear to have been present in T8.0-1. Residual

strengths will not change for the lower compaction levels, but peak strengths will decrease. Bolton (1986) found a relationship between relative state parameter index (I_{RD}) and difference between peak and critical state friction angles as:

$$\phi - \phi_{cs} = xI_{RD} \quad (6.10)$$

where x is approximately 3 for triaxial and 5 for plane strain. For the present set of test data, we have $\phi - \phi_{cs} = 9.5$ deg. Parameter I_{RD} is computed as (Bolton, 1986):

$$I_{RD} = D_r \left(Q - \ln \frac{100 p'}{p_a} \right) - R \quad (6.11)$$

where $Q \approx 10$ (Quartz and feldspar), $R \approx 1.0$, p' = mean stress at failure, p_a = reference stress of 100 kPa. Using stresses for a representative depth of 2.5 m in Eq. (6.11) with a D_r range of 0.85 – 1.0 gives $I_{RD} = 4$ to 5. Using this value of I_{RD} in Eq. (6.10) indicates that $x = 2$ – 2.5.

The reduced D_r of 0.4 – 0.6 for T8.0-1 can be entered into Eq. (6.11) to $I_{RD} = 1.4$ – 2.7, which translates to $\phi - \phi_{cs} = 3$ – 6 deg per Eq. (6.10) with the range of x identified above. Hence, for the looser specimen, peak friction angles are estimated to be in the range of 33 to 36 deg (for plane strain). The cohesion associated with this friction angle is unknown, but a lower value than was used for the high D_r backfill is considered appropriate due to reduced dilatancy (less curvature of failure surface). We estimate the cohesion as being in the range of 10 – 15 kPa.

Summary: LSH simulations are performed for the following strength parameters:

T5.5 and T8.0-2 (peak): $\phi = 39.5$ deg and $c=13$ – 37 kPa (best estimate of 24 kPa)

T5.5 and T8.0-2 (critical state): $\phi = 30$ deg and $c=0$

T8.0-1 (peak): $\phi = 33$ -36 deg and $c=10$ – 15 kPa

T8.0-1 (critical state): $\phi = 30$ deg and $c=0$

6.2.2 LSH Model Comparisons

The log spiral hyperbolic (LSH) simulation procedure and its input parameters are described in Section 2.3.1. Using the wall dimensions given in Chapter 3, a soil unit

weight of 20.1 kN/m^3 , $\varepsilon_{50}=0.35\%$, failure ratio $R_f=0.97$, the strength parameters given in the prior section, and a wall-soil interface friction angle of $\delta=0.5\phi$ (using peak strengths for ϕ), LSH simulations were performed for specimens T8.0-1 and T8.0-2. Results of these simulations are given in Figures 6.4-6.5. The simulations are able to capture the large differences between peak strengths in the two tests, suggesting that the different compaction levels are responsible for the different levels of measured passive capacity.

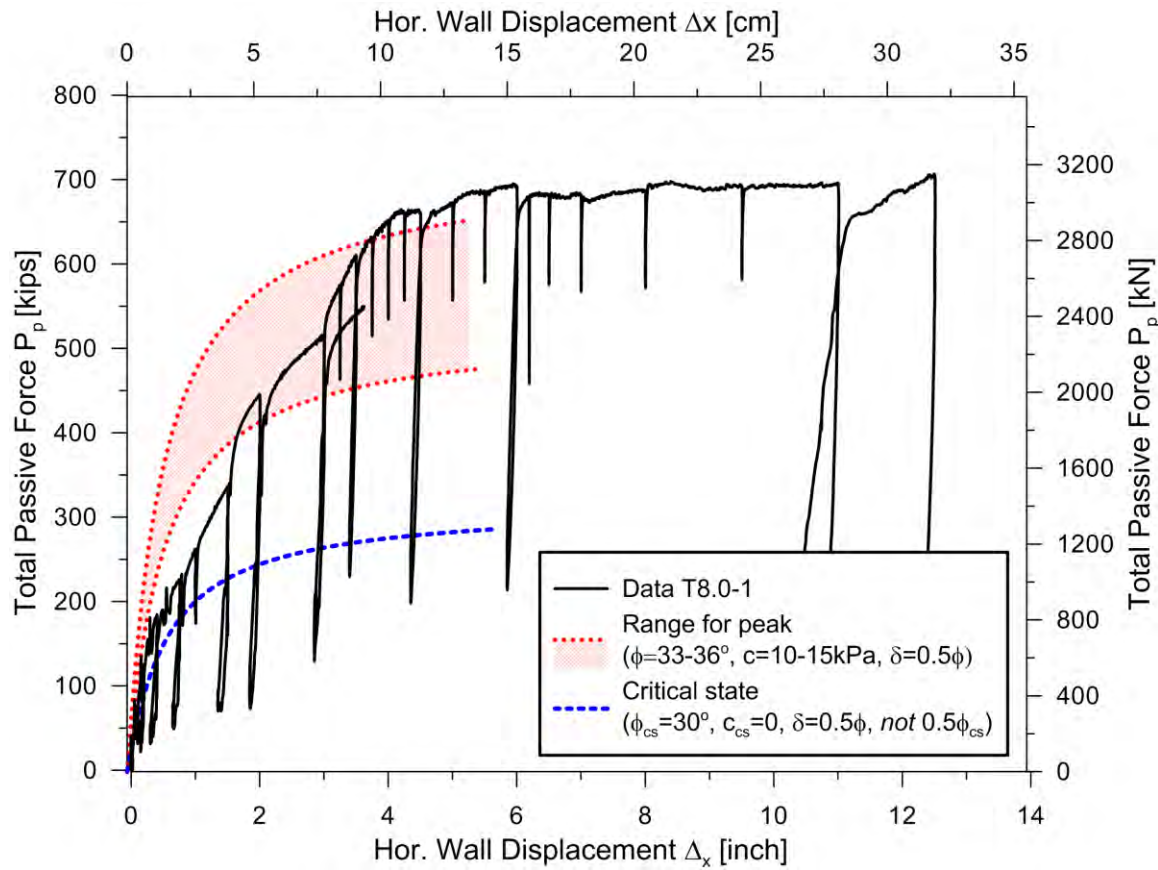


Figure 6.4. Test results for T8.0-1 and LSH predictions of capacity using strength parameters from Section 6.2.1.

For test T8.0-1, the LSH simulation using peak strength parameter overestimate initial stiffness and underestimate peak strength, although the upper bound of considered range is close to the peak strength. The simulations using critical state strengths underpredict stiffness and significantly underestimate capacity. It appears that the assumption of zero cohesion for the critical state condition may be too conservative.

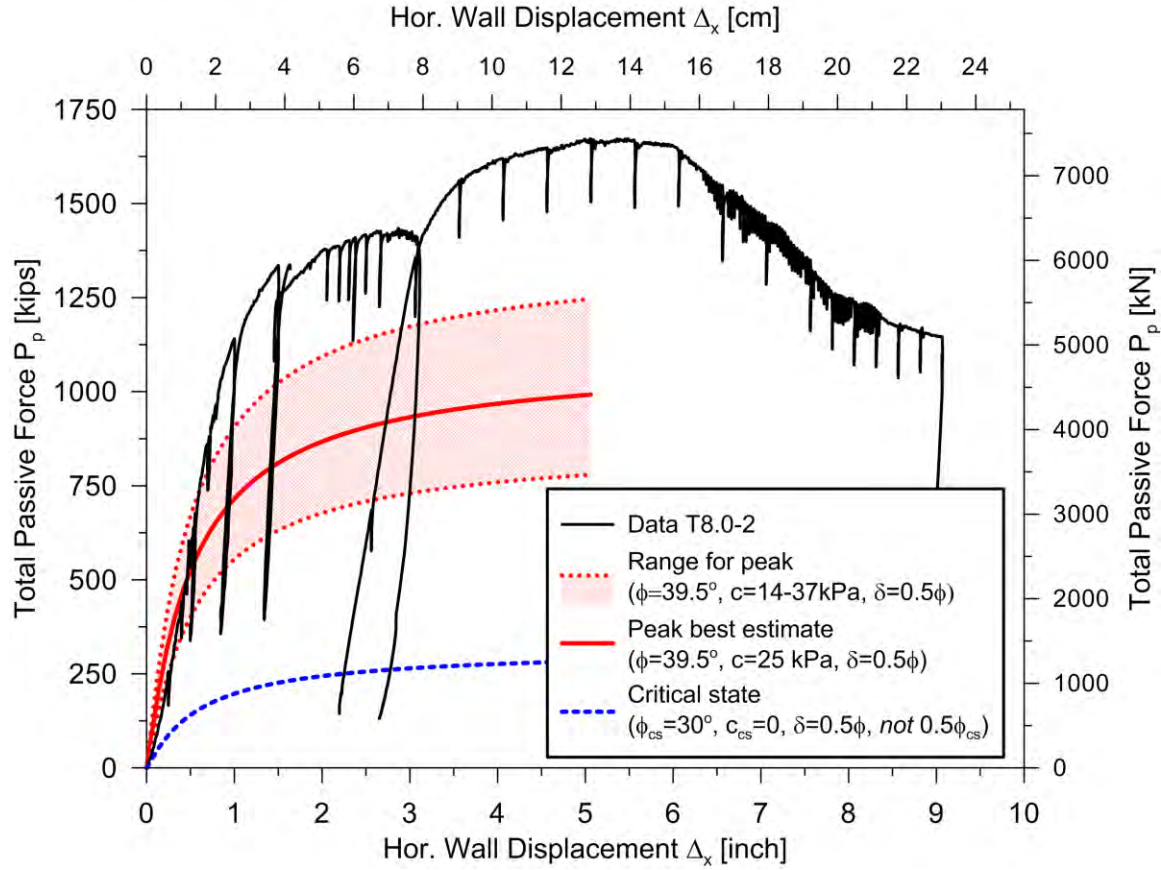


Figure 6.5. Test results for T8.0-2 and LSH predictions of capacity using strength parameters from Section 6.2.1.

For test T8.0-2, the LSH simulation using peak strength parameter capture well the initial stiffness and underestimate peak strength, although the upper bound of considered range is close to the peak strength. The ‘best estimate’ parameters for the peak strength come close to predicting the resistance at the largest deformation levels (approaching residual). As before, the simulations using critical state strengths underpredict stiffness and significantly underestimate capacity. It appears that the assumption of zero cohesion for the critical state condition may be too conservative.

Because the backfill materials and level of compaction for T8.0-2 is comparable to that in T5.5, we also compare LSH predictions to the T5.5 data using the same strength parameters given in Section 6.2.1. As shown in Figure 6.6, the range of predictions using peak strength parameters encompasses the measured peak strength. We consider this model-data comparison to be more useful than that presented in previous publications (*e.g.*, Lemnitzer et al., 2009; Shamsabadi et al., 2010), because those prior simulations

are based on strength parameters developed using non-standard techniques (details in Section 2.1). As in the T8.0-1 and T8.0-2 simulations, the capacity based on critical state strength is much lower than the measured passive resistance at large displacement.

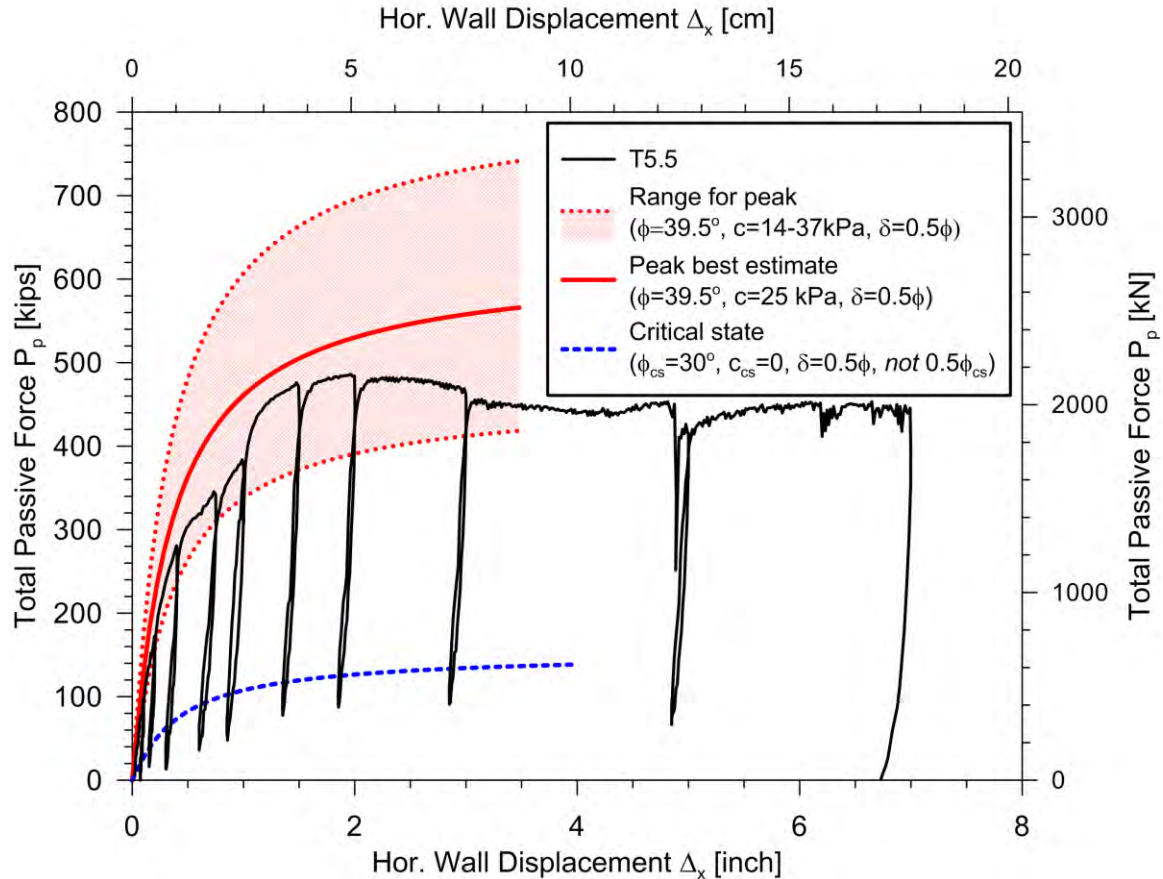


Figure 6.6. Test results for T5.5 and LSH predictions of capacity using strength parameters from Section 6.2.1.

In summary, the laboratory-based peak strength parameters implemented in LSH underpredict the peak resistance observed in the T8.0 tests and slightly underpredict the resistance from prior test T5.5. For the T8.0 tests, the upper bound of the considered range in strength parameters provides wall resistances that are low by amounts ranging from about 15-25%. The center of the range is low by amounts ranging from 30-70%. However, while the predictions are somewhat low, they do capture the large change in resistance between T8.0-1 and T8.0-2 resulting from the different compaction conditions. Several factors may contribute to the LSH under-predictions of peak resistance for the T8.0 tests. The offset between triaxial and plane strain shear strengths may be higher than

anticipated and may also affect cohesion (we only adjusted friction angle). Moreover, the laboratory test specimens may not exactly match field conditions due to subtle differences in compaction methods (less grain breakage in lab) and due to ageing effects that are present in the field but not in the lab tests (e.g., Mitchell and Soga, 2005, p513). The different trend for T5.5 (modest over-prediction with the central value shear strength) likely results from slightly lower compaction levels than were present in T8.0-2, although we do not have CPT data that can be used to verify this hypothesis. Finally, we also see that use of critical state strength parameters in LSH simulations consistently and substantially underestimates large-deformation (approaching residual) passive resistance.

6.2.3 Attempted Inference of Height Effect

Because specimens T5.5 and T8.0-2 have similar compaction conditions, the responses obtained from those tests can in principal be compared to empirically evaluate the height effect. Figure 6.7 plots the two backbone curves with the horizontal axis normalized by wall height. The ratio of the peak capacities from the two tests is approximately 3.4, whereas the ratio of the large deformation (approaching residual) capacities is approximately 2.6. Using an average capacity ratio of about three, the approximate height scaling factor can be solved for using the framework presented in Section 6.1:

$$3.0 = \left(\frac{H_{T8.0-2}}{H_{T5.5}} \right)^n \quad (6.12)$$

This process leads to an exponent of approximately 2.9, which we judge to be unrealistically high. We speculate that the large ratio of capacities results from a higher degree of compaction in T8.0-2 relative to T5.5, although the available information is not sufficient to confirm this hypothesis. For practical application, we recommend use of the height correction factors provided in Section 6.1.

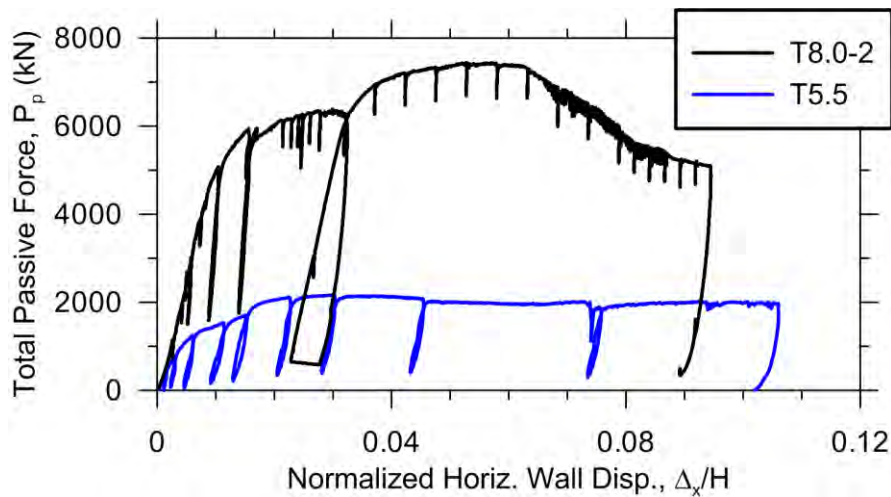


Figure 6.7. Test results for T5.5 and T8.0-2 to show apparent height effect

6.2.4. Comparison of experimental data with analytical and classical solutions

The experimental results from T5.5, T8.0-1 and T8.0-2 were compared with the classical earth pressure theories of Rankine, Coulomb, Log-Spiral (Terzaghi (1943, 1996)) and a Method of Slices (Logarithmic Spiral Hyperbolic, LSH) develop by Shamsabadi et al. (2007, 2010). The input parameters for the analyses are summarized in Table 6.3. Table 6.4 presents results of the calculations along with the test results.

Table 6. 3: Input Parameters for Comparison Study

Test	T5.5	T8.0-1	T8.0-2
ϕ [°]	39.5	34.5	39.5
c [psf (kPa)]	500 (24)	261 (12.5)	500 (24)
δ [°]	13.6	17	18.1
γ [pcf (kN/m ³)]	126 (19.8)	128 (20.1)	128 (20.1)
w [ft (m)]	16 (4.8)	17 (5.18)	17 (5.18)
H [ft (m)]	5.5 (1.68)	8.0 (2.4)	8.0 (2.4)

For both experiments and analysis predictions, capacities are shown in force units and in dimensionless form using the K_p parameter. As described in Chapter 5, the use of K_p , calculated from capacity using Eq. (5.1), is justified from the test results given the triangular pressure distributions revealed by pressure cell data. The backfill cohesion in Table 6.3 was considered in the calculations for P_p using Eq. (6.4). The K_p values used in Eq. (6.4) and listed in Table 6.4 reflect the effects of friction only.

Table 6. 4: Comparison of K_p and P_p from experiment and analyses

Test	Backfill Height [ft (m)]	Rankine		Coulomb		Log-Spiral		LSH		Measured @ Max	
		K_p	P_p [kip (kN)]	K_p	P_p [kip (kN)]	K_p	P_p [kip (kN)]	K_p	P_p [kips (kN)]	K_p	P_p [kip (kN)]
T5.5	5.5 (1.68 m)	4.5	324 (1441)	8.1	497 (2210)	8.55	518 (2304)	15.7	480 (2130)	16.3	497 (2210)
T8.0-1	8.0 ft (2.4m)	3.6	385 (1713)	7.24	695 (3092)	6.8	660 (2936)	8.0	560 (2490)	10.0	707 (3145)
T8.0-2	8.0 ft (2.4 m)	4.5	602 (2678)	10.53	1175 (5227)	9.92	1119 (4977)	12.4	1043 (4600)	24.0	1650 (7340)

The trends described previously in Section 6.2.2 hold for the results in Table 6.4 as well regarding the comparison of predicted LSH capacities using peak strength parameters to the peak resistance. In each test, LSH results are low, with the misfit being greatest for T8.0-2. Capacity predictions using the Terzaghi Log Spiral method are similar to those from LSH. Rankine estimates are systematically quite low, as expected, due to the zero interface friction inherent to this method. Coulomb estimates are fairly similar to those from the Terzaghi Log Spiral method for these specific cases, but this would not generally be expected to hold for other backfill materials. The consistency of these analytical predictions results from compensating factors. Coulomb K_p values are slightly high relative to log-spiral, increasing capacities. On the other hand, Coulomb

failures surfaces are relatively short due to their planar geometry relative to log-spiral, which decreases contributions to capacity from cohesion.

7. Preliminary Analytical Studies on Skew Abutments

In this section, we summarize the preliminary numerical and analytical studies that we have performed for potential future skew wall tests. The particular configuration that is considered here is that of a skew abutment (various angles) that does not experience any rotation from its initial direction of push. This configuration is appropriate for bridges that have substation torsional resistance provided by multiple column bents with adequate stiffness and strength. The more general case of a rotating skew abutment is deferred to a future study.

The aforementioned problem is a three-dimensional one, and at the present time, the only tool to probe this behavior is the finite element method. As such, we have used PLAXIS3D (“Foundation v2.1”) with its *Hardening Soil Model*, which was also used in prior three-dimensional finite element simulations described in Shamsabadi et al. (2010). There are two main objectives of this study:

- (1) How is the backbone curve affected by the degree of skew?
- (2) What side-boundary conditions are needed in a field test, in which it is not technically feasible to have a specimen that bears the full-width (e.g., 75ft or 23m) of an actual bridge deck?

Answers to these two questions are sought in the following sections.

7.1. Three-dimensional Finite Element Simulations of Non-Rotating Skew Walls

The abutment configuration used in the parametric studies is shown in Figure 7.1. The backwall height was 5.5 ft (1.68 m); and the depth of the finite element mesh was 11 ft (3.33 m; i.e., twice the wall height). Meshes for abutments with different skew angles (α) were generated by rotating the wall counter-clockwise in plan view around point A. In some of the simulations, the bridge deck width (L_d)—and by the same token, the backwall width ($L_b = L_d/\cos \alpha$)—were also varied. In such cases, the breadth of the finite element mesh (denoted as “variable” in Figure 7.1) was also varied in order to make sure that the remote boundary was adequately distant from the backwall so that it did not influence the inelastically deforming volume of the soil. The finite element types and other model attributes used in these simulations match those for straight abutment simulations as described by Shamsabadi et al. (2010). The material properties are identical those used in the “lower-bound” simulations of the same (cf., row 2 of Table 2 in Shamsabadi et al., 2010).

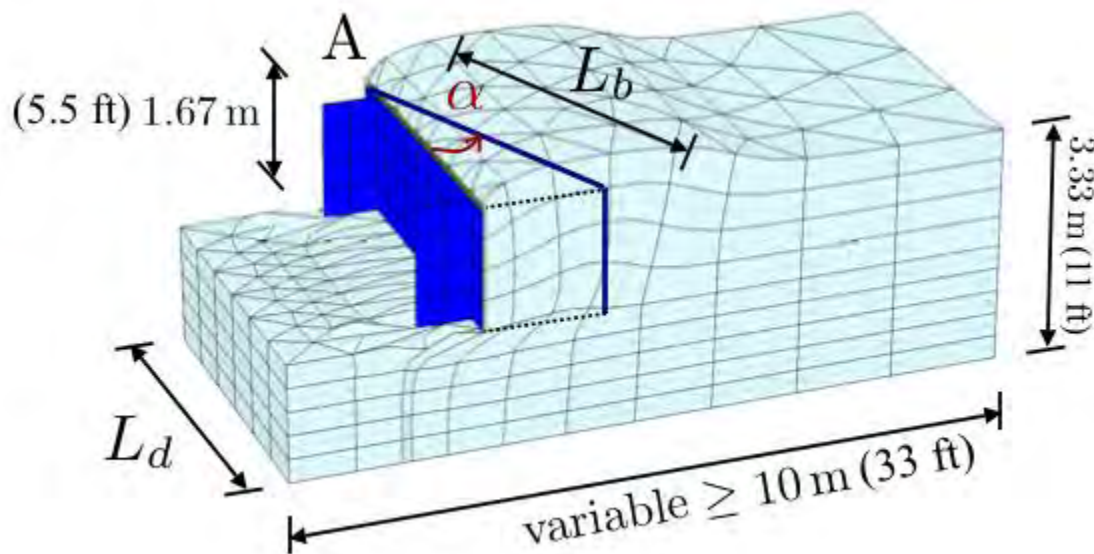


Figure 7.1: Schematic for the generic configuration of straight/skew abutment finite element meshes.

Results of the said numerical simulations are shown in Figure 7.2, wherein the variations of the backfill capacity with respect to the angle of skew and backwall width are presented. As one’s intuition might also suggest, the backfill capacity scales up

linearly with the backwall width, for any skew angle. However, the rate of increase is different for different skew angles. In particular, this rate of increase appears to be inversely proportional with the angle of skew, as indicated by the slope of the regression lines included on this figure.

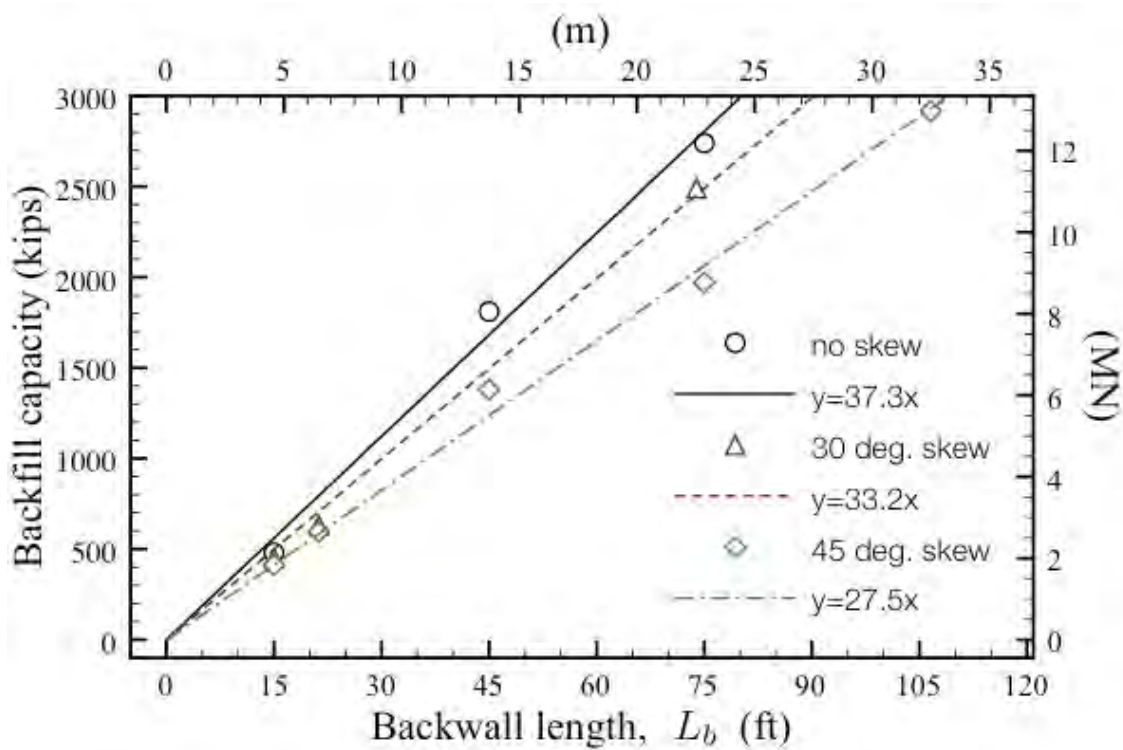


Figure 7.2: Abutment backfill capacity versus backwall length.

A more insightful interpretation of data is offered in Figure 7.3, where the backfill capacity is plotted versus the bridge deck width. Here, we see that *the capacity of the passive backfill increases by approximately 40 kips for every foot of increase in the bridge deck width, and that this increase is identical for any skew angle (of up to, at least, 45°)*. These relationships can be used in combination with those obtained for straight abutment backbone curves (Shamsabadi et al., 2010), to predict the capacity of any skew abutment (up to 45°).

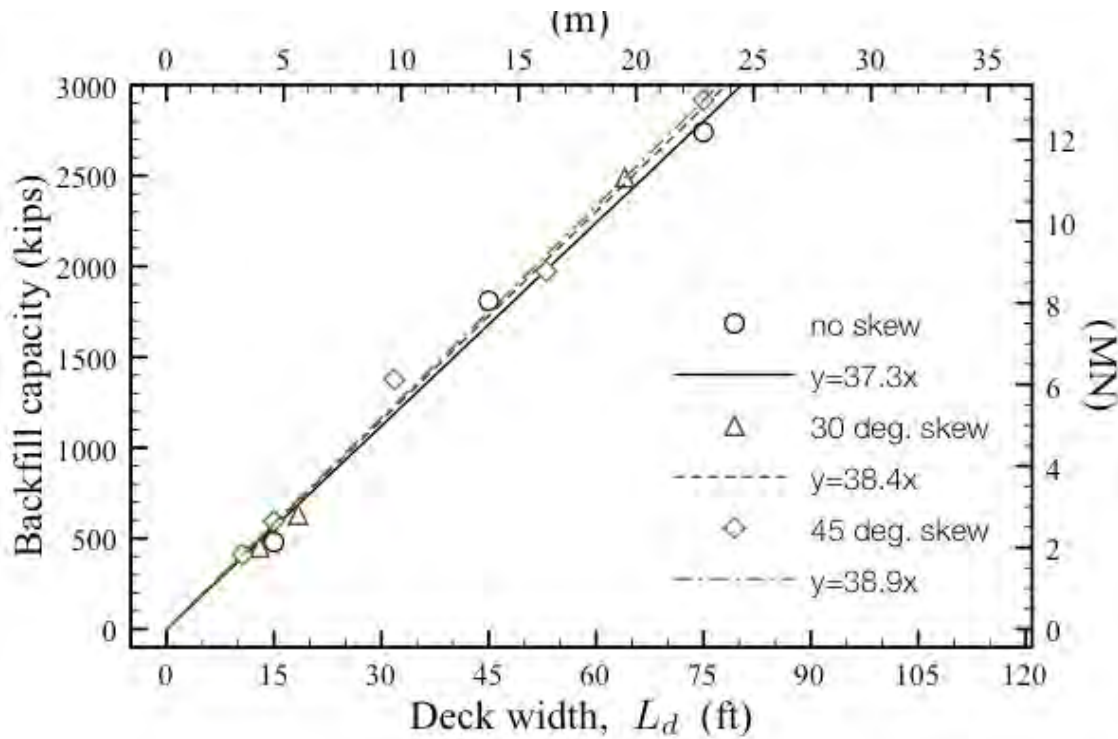


Figure 7.3: Normalized abutment backfill capacity versus deck width.

As it turns out, the aforementioned simple rule breaks down rapidly, for skew angles that are greater than 60° . In simulations of such severely skewed abutments, the backfill behavior was observed to be more complicated, as exemplified by the results shown in Figure 7.4. Here, the pattern of backfill failure surface is different than those of abutments with skew less than 60° , and as a consequence the capacity scaling relationship derived above does not hold. To wit, the capacity of this 15ft (4.6m)-wide deck is ~ 900 kips (4000 kN) which is significantly lower than those computed for smaller angles of skew (i.e., ~ 600 kips (2670) in Figure 7.3). The difference may be attributed to some apparent factors as the participation of cohesive forces on the wall, the aspect ratio (depth versus width) of the backwall, etc.

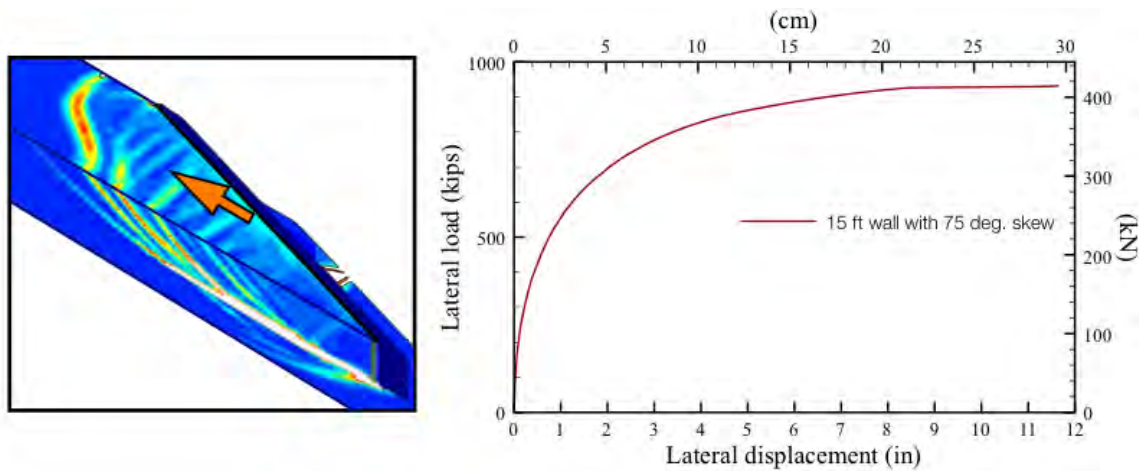


Figure 7.4: Deformed finite element mesh at capacity for a backwall with skew angle 75° and the computed backbone curve.

The influences of the skew angle and backwall length (or deck width) on the stiffness of the passive resistance backbone curve were also studied. Two backbone curves from the simulations are shown in Figure 7.5. These curves belong to a 75ft-wide (23 m) backwall with either 0 or 45 degrees of skew. Here, we see that the initial stiffnesses and the capacity values of these backbone curves are nearly identical. The only discernable difference is the lateral displacement value at which that capacity is reached, which, at any rate, is a sensitive parameter due to the asymptotic/limit nature of the backfill behavior in question.

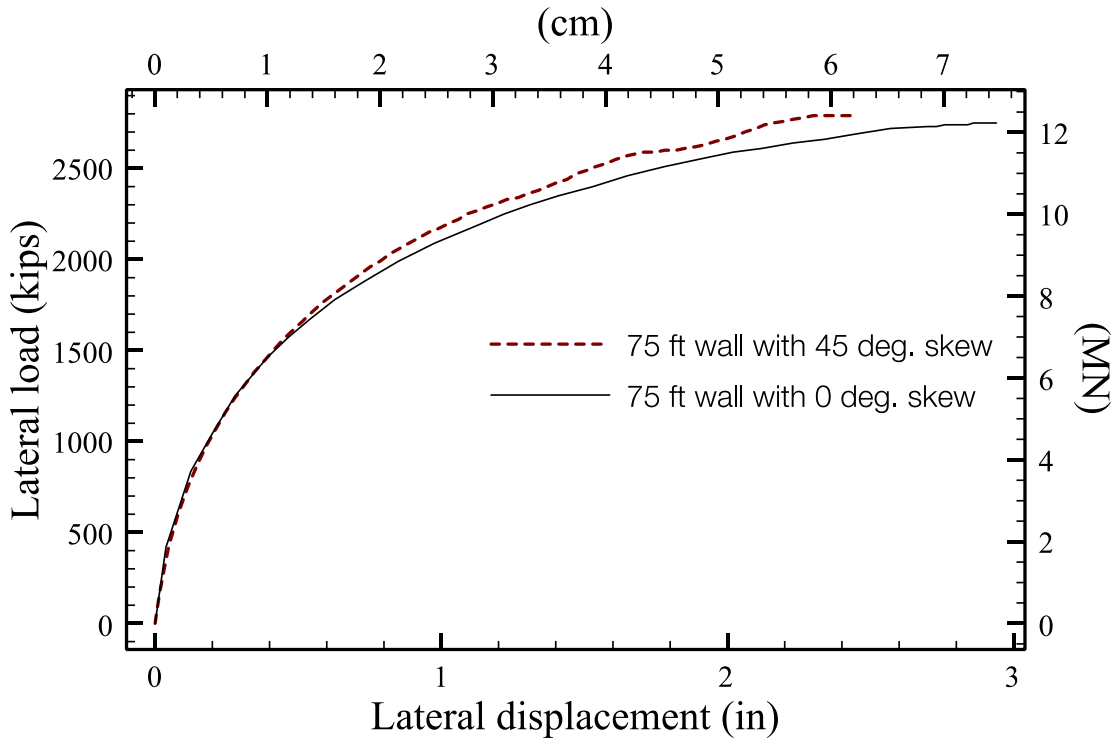


Figure 7.5: Backbone curves for different backwalls lengths and skew angles.

7.2 Influence of Boundary Conditions & Possible Inclination of Wingwalls

It is feasible to construct and test a full-scale backwall specimen (e.g., that for a 75 ft or 23 m wide bridge deck) replete with wingwalls. The feasible maximum specimen width at the UCLA/Caltrans field test site is approximately 15ft (4.5 m). The side-boundary conditions for such a truncated test on a skew angled backwall are not obvious.

For the straight abutment tests, the specimens' backfill had to possess plane-strain conditions throughout the tests, and this was assured by bracketing the two sides of the backfill with plywood sheets that were lined with plastic to minimize friction. The soil particle motions were parallel to the direction of the push; and that this motion was not disturbed at the side boundaries was assured by the plywood-plastic system.

For a skew angled abutment, the collective/average direction of the soil particle motions is not intuitively obvious; and the side-boundaries may have to be inclined relative to the direction of the push. We conducted a set of numerical simulations on skew angled abutment, carried out with PLAXIS3D, to determine the influence of the side boundaries. We obtained a reference/basis solution by simulating a full-size

specimen with a 75 ft (23 m) backwall, and 30° skew. We then observed the particle motions within the central 15 ft (4.5 m) wide portion of this model, and also scaled down the obtained backbone curve by a factor of 4.5/23 (15/75). We then conducted a set of simulations on a skew abutment with a 15 ft (4.5 m) backwall. In each simulation, various aspects of the side boundaries were altered. Figure 7.6 displays the generic configuration of these simulation models; and the altered parameters varied were the side-boundary inclination, the size of a would-be gap between the edge of the backwall and the side boundary. We also added additional layers of soil on the side-boundary dubbed “earrings,” which served to reduce the lateral confinement that was provided by the frictionless, rigid side boundaries.

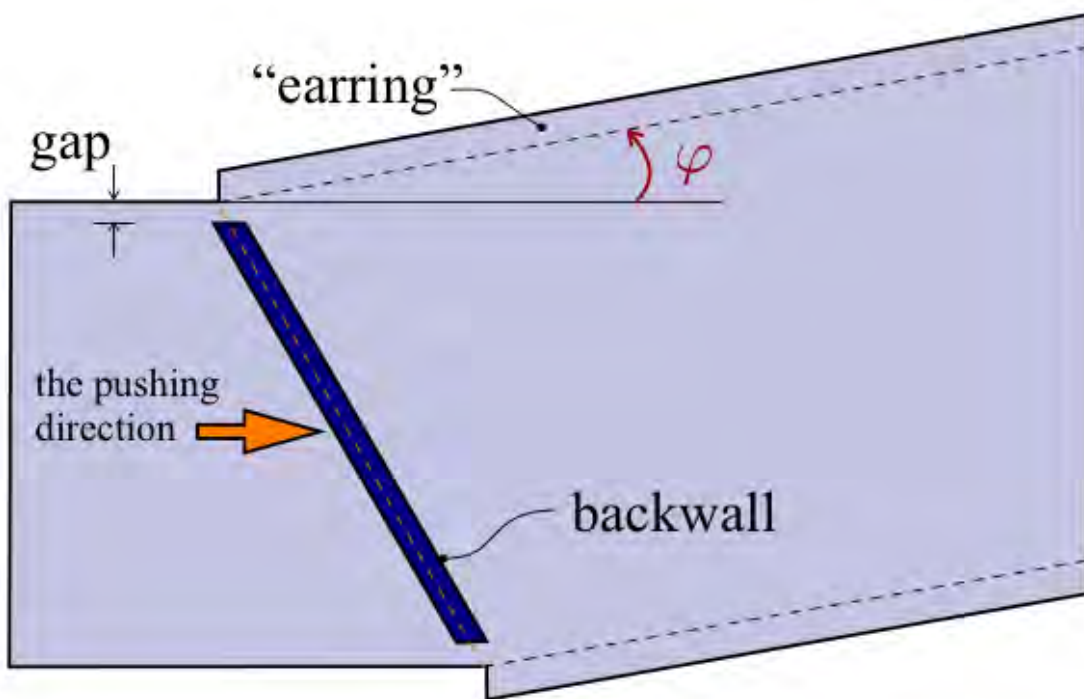


Figure 7.6: Sketch of the model configuration used in side-boundary influence studies.

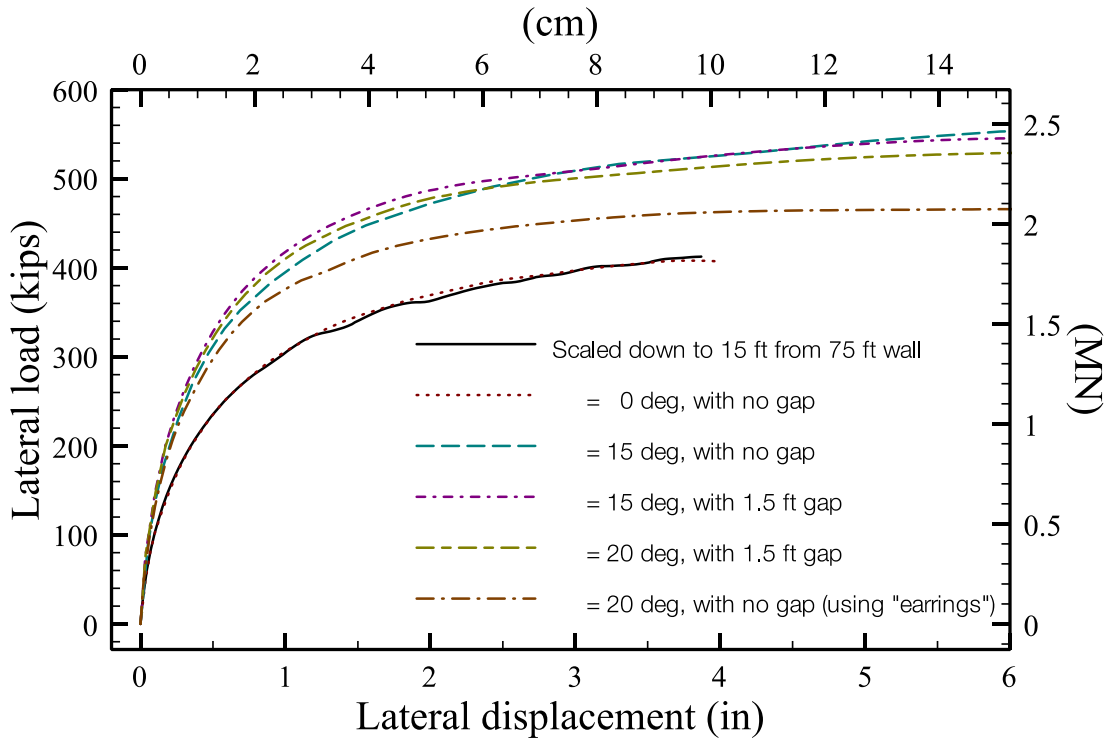


Figure 7.7: Backbone curves a 4.5 m wall with 45° skew for various side-boundary inclination angles.

The backbone curves obtained from the aforementioned simulations along with the reference curve (i.e., the scaled-down from the 75ft (23m)-wide abutment) are displayed in Figure 7.7. Results indicate that, while the particle motions are not parallel to the direction of the push, the best approximation to the reference curve is obtained by the configuration that has side boundaries with a zero inclination angle, which incidentally, requires no gap to accommodate the motion of the rigid (back-) wall. In general, the gap size does not appear to have a significant effect on the backbone curve (at least, for a 0.5m gap). On the other hand, there appears to be a pattern (albeit complex) in the variation of the backbone capacity with the side inclination angle. This pattern is displayed more clearly in Figure 7.8. Here, we see that the capacity increases in general with the side inclination angle (except for a peculiar¹ local minimum at 10 degrees).

¹ These fluctuations, at least in part, could be attributed to differences of mesh sizes in difference simulations.

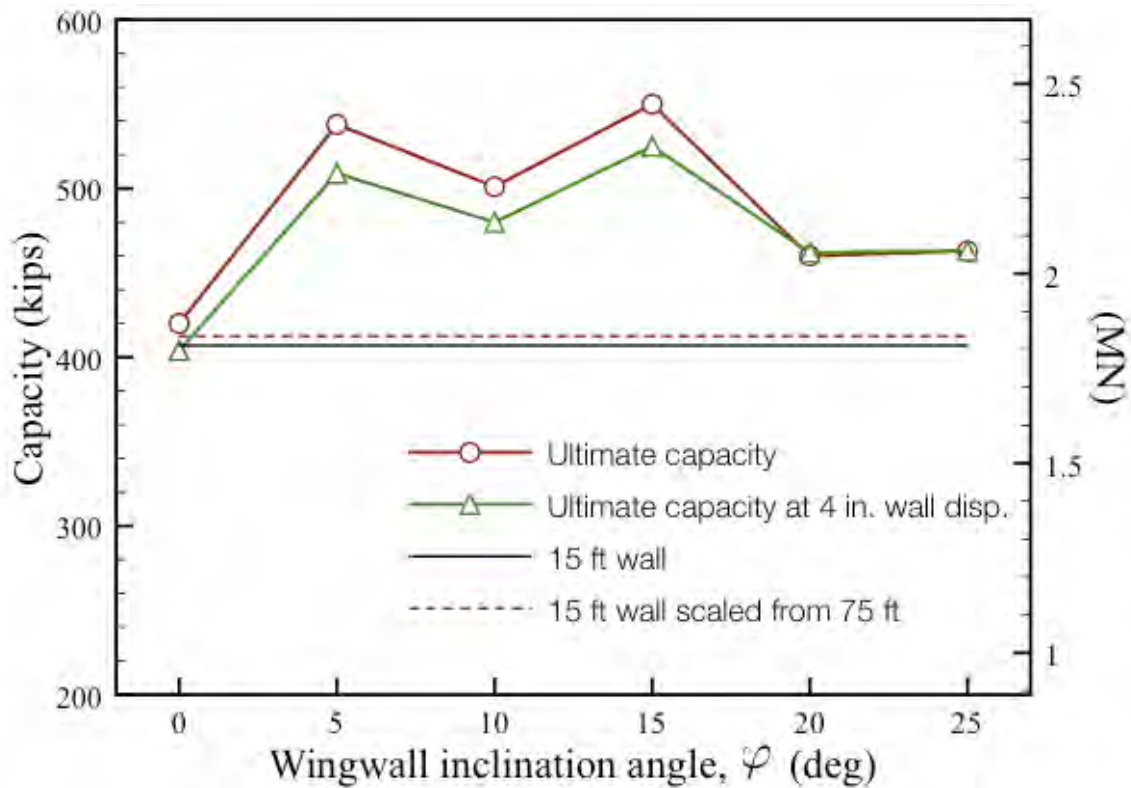


Figure 7.8: Backfill capacity versus the wingwall inclination angle.

In summary, direct push testing of a skew abutment wall should be undertaken with frictionless side-boundaries that are parallel to the direction of the push. This is recommended for consideration in future experimental programs.

Table of Contents

6. Analytical and Numerical Modeling	75
6.1. Development of a HFD Model Incorporating Abutment Height Effects	75
6.1.1 HFD Representation of Test Results for 1.68 m (5.5 ft) Tests	75
6.1.2 HFD Model Extension for Backwall Height Effects	76
6.1.3 Evaluation of Height Exponential Factor n	78
6.1.4 Re-Calibration of EHFD Coefficients	79
6.2. Model Predictions Versus Observed Response.....	82
6.2.1 Selection of Strength Parameters for Use in Analysis.....	82
6.2.2 LSH Model Comparisons	84
6.2.3 Attempted Inference of Height Effect	88
6.2.4. Comparison of Experimental data with analytical and classical solutions	89
7. Preliminary Analytical Studies on Skew Abutments	93
7.1. Three-dimensional Finite Element Simulations of Non-Rotating Skew Walls	94
Table 6. 1: Abutment Backfills Parameters for UCLA and UCD Abutment Tests.	76
Table 6. 2: EHFD coefficients back-calculated using LSH simulation data	79
Table 6. 3: Input Parameters for Comparison Study	Error! Bookmark not defined.
Table 6. 4: Comparison of K_p and P_p from experiment and analyses	Error! Bookmark not defined.

8 SUMMARY AND RECOMMENDATIONS

8.1 Scope of Research

Caltrans Seismic Design Criteria (SDC, 2011) describe the load-deflection relationship for abutment wall-backfill interaction with a bilinear relationship defined by a modulus and capacity. Moduli are specified separately for clay and sand backfills as 20 and 50 kips/in per foot of wall width (145 and 290 kN/cm/m), respectively, for walls 5.5 ft (1.67 m) in height. For this same wall height, capacity is defined from a uniform pressure of 5.0 ksf (240 kPa) acting normal to the wall. Both stiffness and capacity are assumed to scale linearly with wall height. Compaction conditions of the backfill materials are not directly considered in assigning stiffness or strength parameters.

This research addresses the scaling of abutment wall lateral response with wall height and compaction condition. The scaling with wall height was investigated through testing and analytical work. The analytical work explored the manner by which hyperbolic curves representing the load-deflection response of backfills scale with wall height using calibrated log-spiral hyperbolic (LSH) models for backfill response. The results apply to the same clay and sand backfill materials considered in SDC (2011) and are expressed as relatively simple closed-form expressions. The height scaling effect was also investigated experimentally. However, because wall-soil resistance scales strongly with compaction condition and identical compaction conditions in two separate specimens are nearly impossible to achieve, we identified a height effect that we consider unrealistic. Therefore, we recommend the use of the analytical solutions for analysis of height effects.

The properties of compacted soils are known to be strongly dependent on compaction condition. We tested two wall-soil specimens with identical characteristics except for the level of compaction of the sandy backfill. One specimen has as-compacted relative densities ranging from approximately $D_r = 0.4\text{--}0.6$ and the other had an unusually high level of compaction of D_r

= 0.9-1.0. These results are compared to evaluate the effects of compaction condition and the ability of analytical models to capture the variation of wall resistance with compaction condition.

8.2 Principal Findings and Recommendations

The scaling of backwall resistance with height can be expressed by an exponent n applied to a normalized wall height (e.g., Eq. 6.8). Classical Rankine-Bell earth pressure theory suggests limiting values of n approaching 1.0 for cohesive soil and 2.0 for cohesionless granular soil. Using the strength parameters for the cohesive and granular materials considered in SDC (2011), we find that the height scaling exponent can be taken as 1.05 and 1.56, respectively. Closed form hyperbolic equations that include this height scaling are provided in Eq. 6.9.

Two test sequences were completed. The first is denoted T8.0-1 and involved the modestly compacted granular backfill. The second is denoted T8.0-2 and involved the unusually dense backfill material. Other than the degree of compaction, the two specimens are essentially identical in terms of dimensions, material gradation, and boundary conditions imposed during testing. Specimen T8.0-1 exhibits nearly elastic-plastic response with negligible strain softening. The peak resistance was approximately 700 kips (3145 kN) and occurred with a wall-soil interface friction that is approximately half of the soil friction angle. Specimen T8.0-2 exhibits a strongly strain softening response with a peak resistance of approximately 1650 kips (7340 kN) and large-strain (approaching residual) capacity of approximately 1100 kips (5000 kN). As before, the wall-soil interface friction angle was approximately half of the soil friction angle. Because the earth pressure distribution behind the backwall was measured to be of triangular shape, these capacities can be equivalently expressed as passive earth pressure coefficients (K_p). Values of K_p were found to be 10.0 for T8.0-1 at the point of ultimate capacity and 24.0 and 17.0 for T8.0-2 at ultimate and residual capacities, respectively.

Following conventional geotechnical practice, we characterize the soil strength parameters using drained triaxial testing over a range of normal stresses that represent in situ conditions. We evaluate peak strength parameters for the dense backfill configuration and apply corrections for plane strain effects and for the looser backfill configuration. We also estimate critical state parameters using the test results and literature. Due to scatter in the test data, there is some uncertainty in the strength parameters which we quantify and consider in the analysis. When these strength parameters are used in LSH simulations of the backfill response, we find

modest under prediction of the peak response for the upper bound of the considered range of strengths; central values of strength parameters produce more substantial under prediction. Nonetheless, the degree of underprediction is modest relative to the substantial differences in capacity between specimens T8.0-1 and T8.0-2. Those large variations in capacity between specimens are well captured by the analysis, suggesting that the LSH method can account for the effects of compaction condition on the wall capacity. The LSH simulations are also able to capture variations in specimen response for different wall height.

We recommend that the height scaling effects in future versions of the SDC be modified to more realistically capture the different trends for cohesive and granular backfills. For granular backfill, capacity should scale by an exponent $n = 1.5\text{--}2$. We also recommend that compaction condition be considered in the specification of stiffness and capacity. This research has demonstrated the substantial, first-order impact of this important parameter which can vary substantially in the field from site-to-site due to variations in construction quality.

8.3 Recommendations for Future Research

We recommend that future research consider skew abutments both for the cases when the skewed wall is pushed into the backfill without twisting and for cases where the push is accompanied by torsional rotation. Additionally, future testing should consider energy dissipation associated with wall-backfill interaction and its effects on bridge response. Finally, the test inventory should be extended beyond the SE30 materials considered in the present work to include silty and clayey soils with varying levels of compaction. It is too simplistic to classify soils as simply cohesive or cohesionless for the purposes of establishing passive force-deflection relationships.

REFERENCES

- ASTM. (2009). "Standard Test Methods for Laboratory Compaction Characteristics of Soil Using Modified Effort (56,000 ft-lbf/ft³ (2,700 kN-m/m³))." *D1557*, West Conshohoken, Pa.
- ASTM. (2006). "Standard Test Methods for Maximum Index Density and Unit Weight of Soils Using a Vibratory Table." *D4253*, West Conshohoken, Pa.
- ASTM. (2006). "Standard Test Methods for Minimum Index Density and Unit Weight of Soils and Calculation of Relative Density" *D4254*, West Conshohoken, Pa.
- ASTM. (2007). "Standard Test Method for Unconsolidated-Undrained Triaxial Compression Test on Cohesive Soils." *D2850*, West Conshohoken, Pa.
- Bolton, M.D. (1986). "The strength and dilatancy of sands." *Geotechnique*, 36 (1), 65-78.
- Bowles, J.E. (1996). *Foundation analysis and design*, 5th edition, McGraw-Hill, New York, NY.
- California Dept. of Transportation (CALTRANS). (2010). "Seismic Design Criteria, ver.1.6, Nov 2010." CALTRANS, Division of Engineering Services, Office of Structure Design, Sacramento, Calif.
- Carder, D.R., Pocock, R.G., and Murray, R.T. (1977). "Experimental retaining wall facility lateral stress measurements with sand backfill," *Rep. 766, Transport and Road Research Laboratory*, Crowthorne, Berkshire, England.
- Dubrova, G.A. (1963). *Interaction of Soil and Structures*. Rehnay Transport Publishing, Moscow, USSR.
- Duncan, J.M., and Chang, C.-Y. (1970). "Nonlinear analysis of stress and strain in soils." *J.Soil Mech. & Foundations Div.*, ASCE, 96(5), 1629-1653.
- Earth Mechanics, (2005). "Field Investigations Report for Abutment Backfill Characterization, Response Assessment of Bridge Systems - Seismic, Live, and Long Term Loads." *Report to Dept. of Structural Engineering, University of San Diego, La Jolla*
- Fang, Y.-S., Chen, T.-J., Wu, B.-F. (1994). "Passive earth pressure with various wall movements," *J. Geotech. Engrg. ASCE*, 120(8), 1307-1323.

- Gadre, A. and Dobry, R. (1998). "Lateral cyclic loading centrifuge tests on square embedded footing," *J. Geotech. & Geoenv. ASCE*, 124(11), 1128-1138.
- Idriss, I.M., and Boulanger, R.W. (2008). *Soil Liquefaction During Earthquakes*, Monograph series, No. MNO-12, Earthquake Engineering Research Institute.
- James, R.G. and Bransby, P.L. (1970). "Experimental and theoretical investigations of a passive earth pressure problem," *Geotechnique*, 20(1), 17–36.
- Lam, I.P. and Martin, G.R. (1986). "Seismic Design of Highway Bridge Foundations," Reports FMWA/RD-86/101,102, and 103, Federal Highway Administration, Washington, D.C.
- Lambe, T. W., and Whitman, R. V. (1969). *Soil Mechanics*, Wiley and Sons, NY.
- Lee, K.L (1970). "Comparison of plane strain and triaxial tests on sand," *J. Soil Mechanics & Foundations Div.*, ASCE, 96 (3), 901-923.
- Lemnitzer, A., Ahlberg, E.R., Nigbor, R.L., Shamsabadi, A., Wallace, J.W., Stewart, J.P. (2009). "Lateral performance of full-scale bridge abutment wall with granular backfill" *J. Geotech. & Geoenv. Eng.*, ASCE, 135 (4), 506-514.
- Mackey, R.D. and Kirk, D.P. (1968). "At rest, active and passive earth pressures," *Proc. Southeast Asian Conf. on Soil Mech. and Found. Engrg.*, Asian Institute of Technology, Bangkok, Thailand, 187–199.
- Mitchell, J.K., and Soga, K., (2005). *Fundamentals of Soil Behavior*, 3rd Edition. John Wiley & Sons, Hoboken.
- Narain, R.J., Saran, S., and Nandakumaran, P. (1969). "Model study of passive pressure in sand," *J. Soil Mech. Found. Div.*, ASCE, 95(SM4), 969–983.
- Negussey, D., Wijewickreme, W.K.D., and Vaid, Y .P. (1988). Constant volume friction angle of granular materials. Canadian Geotechnical Journal, 25: 50-55.
- Rabbat, B.G. and Russel, H.G. (1985). "Friction coefficient of steel on concrete or grout." *J. Struct. Eng.*, ASCE, 111 (3), 505-515.
- Robertson, P.K., and Wride, C.E. (1998). "Evaluating cyclic liquefaction potential using the cone penetration test." *Can. Geotech. J.* 35: 442–459.
- Rollins, K. M., and Cole, R. T. (2006). "Cyclic lateral load behavior of a pile cap and backfill." *J. Geotech. Geoenvir. Eng.*, ASCE 132 (9), 1143–1153.
- Rollins, K.M. and Sparks, A. (2002). "Lateral resistance of full-scale pilecap with gravel backfill," *J. Geotech. & Geoenv. Engrg. ASCE*, 128(9), 711-723.

- Romstadt, K., Kutter, B.L., Maroney, B., Vanderbilt, E., Griggs, M., and Chai, Y.H. (1995). "Experimental measurements of bridge abutment behavior." *Rep. No UCD-STR-95-1*, Structural Engineering Group, Univ. of California, Davis, CA.
- Roscoe, K.H. (1970). "The influence of strains in soil mechanics," *Geotechnique*, 20 (2), 129–170.
- Rowe, P.W. and Peaker, K. (1965). "Passive earth pressure measurements," *Geotechnique*, 15 (1), 57–78.
- Salgado, R., Mitchell, J. K., and Jamiolkowski, M. (1997). "Cavity Expansion and Penetration Resistance in Sand." *J. Geotech. & Geoenv. Eng.*, ASCE, 123 (4), 344-354.
- Schofield, A. N. (1961). "The development of lateral force of sand against the vertical face of a rotating model foundation," *Proc. 5th International Conf. Soil Mech. and Found. Engrg.*, Paris, 479–484.
- Shamsabadi, A., Rollins, K.M., and Kapuskar, M. (2007). "Nonlinear soil-abutment-bridge structure interaction for seismic performance based design." *J. Geotech. Geoenviron. Eng.*, ASCE, 133 (6), 707–720.
- Shamsabadi, A., Khalili-Tehrani, P. Stewart, J.P., Taciroglu, E. (2010). "Validated simulation models for lateral response of bridge abutments with typical backfills." *J. Bridge Eng.*, ASCE, 15 (3), 302-312.
- Terzaghi, K. (1943). *Theoretical soil mechanics*, Wiley, New York.
- Stewart, J.P., E. Taciroglu, J.W. Wallace, E.R. Ahlberg, A. Lemnitzer, C. Rha, P.K. Tehrani, S. Keowen, R.L. Nigbor, and A. Salamanca (2007). "Full scale cyclic testing of foundation support systems for highway bridges. Part II: Abutment Backwalls," *Report No. UCLA-SGEL 2007/02*, Structural and Geotechnical Engineering Laboratory, University of California, Los Angeles.
- Terzaghi, K., Peck, R.B., and Mesri, G. (1996). *Soil Mechanics in Engineering Practice*, 3rd Ed., Wiley, New York, NY.
- Tschebotarioff, G.P., and Johnson, E.G. (1953). "The effects of restraining boundaries on the passive resistance of sand," *Rep. to the Office of Naval Research*, Princeton Univ., Princeton, N.J.
- Zhang, G., Robertson, P. K., and Brachman, R. W. I. (2002). "Estimating liquefaction induced ground settlements from CPT for level ground." *Can. Geotech. J.*, 39 (5), 1168–1180.